The Pennsylvania State University

The Graduate School

Department or Materials Science and Engineering

PROBING ANODE DEGRADATION IN AUTOMOTIVE LI-ION BATTERIES

A Dissertation in

Materials Science and Engineering

by

Ou Jung Kwon

Submitted in Partial Fulfillment
of the Requirements
for the Degree of

Doctor of Philosophy

December 2010

The thesis of Ou Jung Kwon was reviewed and approved* by the following:

Chao-Yang Wang
Distinguished Professor of Mechanical Engineering and
Professor of Materials Science and Engineering
Dissertation Advisor
Chair of Committee

Michael A. Hickner
Assistant Professor of Materials Science and Engineering

Christopher D. Rahn
Professor of Mechanical Engineering

Donghai Wang
Assistant Professor of Mechanical Engineering

Joan M. Redwing
Professor of Materials Science and Engineering
Chair of Intercollege Graduate Degree Program in Materials Science and Engineering

*Signatures are on file in the Graduate School

ABSTRACT

The lithium-ion battery is drawing attention as a power source for future clean and fuel-efficient vehicles. Although the Li-ion battery presently shows best performance for energy density and power density compared to other rechargeable batteries, some degradation problems still remain as key challenges for long-term durability in automotive applications. Among those problems, Li deposition is well known for causing permanent capacity loss. Fundamental mechanisms of Li deposition in the carbon anode are, however, not fully understood, especially at subzero temperature and/or under high rate charge. This dissertation introduces comprehensive study of Li deposition using automotive 18650 Li-ion cells. The mechanism and relevant diagnostic methods as well as preventive charging protocol are discussed.

In part one, a new diagnostic tool is introduced utilizing 3-electrode cell system, which measures thermodynamic and kinetic parameters of cathode and anode, respectively, as a function of temperature and SOC (state of charge): open circuit potential (OCP); Li diffusion coefficient in active particles; and internal resistance. These data are employed to understand electrochemical reaction and its thermal interaction under charging conditions that result in Li deposition.

Part two provides a threshold parameter for the onset of Li deposition, which is not commonly used anode potential but charge capacity, or more specifically the amount of Li^+ ions participating in intercalation reaction without Li deposition at given charging circumstances. This is called the critical charge capacity in this thesis, beyond which

capacity loss at normal operating condition is observed, which becomes more serious as temperature is lowered and/or charge C-rate increases.

Based on these experimental results, the mechanism of Li deposition is proposed as the concept of anode particle surface saturation, meaning that once the anode particle surface is saturated with Li in any charging circumstances, no more Li^+ ions can be intercalated but should be reduced to metallic form on the anode particle surface. This is validated by calculating the distribution of Li concentration inside the anode particle with electrochemical modeling.

In part three, a novel pulse charge protocol is developed, which consists of two steps. First high current charge/discharge pulses increase the cell temperature from a subzero temperature up to above room temperature in a short time, and next, high current charge provides the net charge capacity. Sluggish Li diffusion at low temperature becomes fast thanks to cell temperature elevation by high current pulses (1^{st} step), which plays a role of preventing surface saturation during high current charge (2^{nd} step). Thus, this charge protocol is not only Li deposition-free but also leads to rapid charge at subzero temperatures.

TABLE OF CONTENTS

LIST OF FIGURES

LIST OF TABLES

NOMENCLATURE

Symbols

D	Li diffusion coefficient
E	Cell potential
η	Overpotential
I	Current
R	Internal resistance
$\dot{Q}_{\mathrm{P}}$	Rate of irreversible heat (polarization heat)
$\dot{Q}_{\mathrm{S}}$	Rate of reversible heat (entropy heat)
T_{cell}	Internal temperature of 18650 Li-ion cell
T_{can}	Surface temperature of 18650 Li-ion cell
T_{amb}	Ambient temperature

Acronyms

AC	Alternating current
BMS	Battery management system
CC	Constant current
CCCV	Constant current and constant voltage
DC	Direct current
EIS	Electrochemical impedance spectroscopy
EV	Electric vehicle
GITT	Galvanostatic intermittent titration technique
HEV	Hybrid electric vehicle
NiMH	Nickel metal hydride
OCP	Open circuit potential
PHEV	Plug-in hybrid electric vehicle
SOC	State of Charge

ACKNOWLEDGEMENTS

First and foremost, I am sincerely thankful to my advisor, Dr. Chao-Yang Wang, whose guidance, encouragement and support enabled me to complete this Ph.D. research in the last 3 years. I wish to thank Dr. Richard Steinberger for his kind help and idea to install experimental devices. I would like to thank Dr. Weifeng Fang for his computer simulation data with many discussions. My thanks also go to all other members of Electrochemical Engine Center.

I would like to show my appreciation to Mr. Yosuke Ishikawa, Honda Motor Company, for the financial support and insightful discussions during the project. I also express my gratitude to the rest of my thesis committee: Dr. Michael Hickner, Dr. Christopher Rahn and Dr. Donghai Wang, for their time and invaluable comments.

Specially, my great thanks heartily go to my wife, Seung Hee Jang, for all her love and encouragement. I could not have imagined finishing this study without her. I am grateful to my son, Hyukjae Jason Kwon, for bring happiness and joy into my life. I finally appreciate my parents who always pray for me in Korea. To all of them I dedicate this dissertation.

Chapter 1

Introduction

Li-ion batteries are one of the critical enabling technologies for future clean and fuel-efficient automobiles [1]. Many research institutions funded by government as well as automotive industry are struggling to develop durable, safe and affordable batteries from active materials to management systems. Since Sony first released Li-ion batteries in 1991, Li-ion batteries have been so outstandingly developed that they show the highest power and energy density in the rechargeable battery market.

Although Li-ion batteries have no competitors in portable electronic devices such as laptops and cell phones, they are still in the infancy stage for automotive application. Only a few expensive vehicle models are powered by Li-ion batteries, such as the Tesla Roadster. Most major auto companies are only now competitively announcing such new cars, to be released within the next couple of years. The main reason is that for the past a decade the research and development stream has focused on the hybrid electric vehicle (HEV), such as the Toyota Prius, where battery assists only a small portion of propulsion power. Nickel metal hydride (NiMH) batteries were adoptable and affordable for HEV, but the economic and strategic needs (importing oil and environment issue) for plug-in hybrid vehicles (PHEV), such as GM Chevy Volt, or pure electric vehicles (EV), such as Ford Focus and Nissan Leaf, are continuously growing. PHEV and EV prefer Li-ion batteries over NiMH batteries because they need higher energy density to extend

electrical driving range: Li-ion batteries can offer weight reduction of 40~50% and volume reduction of 20~30% as well as a margin of efficiency improvement [2].

1.1. Literature review

For the past two decades, most research topics in Li-ion batteries can be categorized into two areas: (1) study of new materials to improve performance (capacity, energy density, power density) and to satisfy safety requirement; (2) degradation study for life-extension. Both have been mainly focused on portable electronics because Li-ion batteries are now generally used in laptops and cell phones. Recently, research has been extended to large-sized and high power applications. In this chapter, we review relevant literature in the areas of automotive Li-ion batteries.

1.1.1. Li-ion battery

Lithium metal is the most attractive material in rechargeable batteries because of its lightest atomic weight and lowest redox potential (-3.045V vs. standard hydrogen electrode) among all metals, and offers highest energy (3,863mAh/g) and power density, theoretically. However, prolonged deposition/dissolution cycling causes dendrite formation in Li metal, which brings about serious problems in safety and cycleability for rechargeable batteries [3]. In order to overcome the problem of Li dendrite formation and provide improvement in safety and cycleability, carbon anodes have been selected because lithiated carbon (LiC_6) shows negative electrochemical potential close to that of

the metallic lithium electrode and reversible intercalation/deintercalation reaction [3]. The carbon anodes combined with lithium transition metal oxides of layered structure such as $LiCoO_2$ can provide 4V-class Li-ion cells. Armand [4] proposed this working principle as the concept of "Rocking Chair Battery". When Sony began to produce commercial batteries using this concept, they first named this battery the "Li-ion battery" in order to emphasize that there is no lithium metal inside the cell. This term now is accepted by the battery market worldwide [5].

These electrode reactions are depicted in Fig. 1-1 and expressed as follows:

Anode: $\mathrm{Li_xC_6} \xrightarrow{\text{discharge}} \mathrm{C_6} + \mathrm{xLi^+} + \mathrm{xe^-}$

$E^0_{anode} \approx 0 \sim 0.5\mathrm{V}$

Cathode: $\mathrm{Li_{(1-x)}M_yO_z} + \mathrm{xLi^+} + \mathrm{xe^-} \xrightarrow{\text{discharge}} \mathrm{LiM_yO_z}$

$E^0_{cathode} \approx 4.5 \sim 3.5\mathrm{V}$

Overall: $\mathrm{Li_{(1-x)}M_yO_z} + \mathrm{Li_xC_6} \xrightarrow{\text{discharge}} \mathrm{LiM_yO_z} + \mathrm{C_6}$

$\Delta E = E^0_{cathode} - E^0_{anode} \approx 4\mathrm{V}$

where M is transition metal like Co, Ni and Mn etc. Both lithium transition metal oxide and carbons play a role of host materials. On discharge, the anode supplies Li^+ ions through electrolyte and equivalent electrons through external circuit to the cathode. Li^+ ions are inserted into the cathode as guest species. On charge, the opposite reaction occurs. Li conducting organic electrolyte consists of a solution of a lithium salt ($LiPF_6$) in a mixture of high dielectric solvent and low viscosity solvent (ethylene carbonate /dimethyl carbonate, EC/DMC) soaked in a separator. The separator is a porous

membrane placed between electrodes, which allows ionic conduction path of lithium but blocks electrical connection [5].

This working principle can be implemented not only in portable electronic applications but also in automotive applications. Numerous research and development efforts have been conducted to improve performance of the Li-ion battery for the past two decades. For example, when 18650 cylindrical cells, such as the most common sized Li-ion cell with 18mm diameter and 65mm length in Fig. 1-2, were introduced in 1991, these cells had about 1.2Ah, but these have now been increased up to about 2.9Ah [6]. In automotive application, four key challenges still remain to be addressed by the US Department of Energy (DOE) Applied Battery Research, denoted the Advanced Technology Development (ATD) program [1]:

- Calendar life of 15 years.
- Cost of $20/kW
- Ability to operate between -30 and 52^{o}C
- Sufficient abuse tolerance for use in on-road light-duty vehicle applications

For instance, most portable electronic devices are quickly replaced with newly released models within 2~3 years; but the power source of the electric car should guarantee 10~15 years due to huge replacement cost. Nobody expects to operate a cell phone or laptop at -30^{o}C; but automobiles need to work at this temperature. Most electronic devices are designed to operate at room temperature, but electric vehicles should be charged in winter as well as summer temperatures. In automobile application, the system requirement of fast repetition with high C-rate between discharge (acceleration) and charge (regen braking) should be met, rather than low C-rate and continuous cycle between charge and

discharge in portable electronics. These tough operating conditions can cause degradation of Li-ion batteries. The next section deals with this degradation, focusing on key barriers in automotive applications.

1.1.2. Degradation of Li-ion battery

Degradation characteristics of various active materials in the Li-ion battery have been extensively reported and the following mechanisms of capacity and/or power fading are most often introduced [7, 8]:

- Degradation of crystalline structure or phase transformation
- Graphite exfoliation due to solvent co-intercalation
- Metallic Li deposition
- Build-up of passivation film on both electrodes
- Depletion of electrolyte
- Mechanical loss of composite electrode structure due to volume change of active particles during cycling and binder decomposition

Long-term storage characteristic tests for calendar life of 15 years require literally long time. Thus, accelerated tests are usually conducted by continuous high rate cycling or by varying storage temperature, which is considered as a worst case for reversibility of Li-ion cell reaction [7]. Battery life predictions are employed by extrapolation of accelerated test results [9] as well as electrochemical models [10-14]. As is generally known, capacity fading results from active material transformation in inactive phase, which reduces capacity at any rate, increases cell impedance and lowers the operating voltage; Power fading is directly related impedance rise [7]. Nevertheless, capacity

fading and power fading do not simply result from one single cause but from various processes and their interactions, and moreover it is not easy to study most of these processes independently [8]. Therefore, this demands introduction of a reference electrode inside cell to distinguish which part in the Li-ion cell causes the capacity and power fading.

Although several papers about 3-electrode cells have been published, some of them require their own home-made cell with small electrode area [15, 16]. As electrode stack pressure and electrolyte composition and so on can generally affect the cell performance, it is hard to directly compare a cell with small electrode area and a real cell. During dismantling the cell for diagnosis, the risk of poor electrode adhesion can be exposed. The debris of active materials is occasionally observed. Also, the harvested electrode typically shows the unstable capacities according to solvent rinse and additional press [17]. Other papers announced their 3-electrode cell systems utilizing manufacturing process from initial cell fabrication [18-21]. However, this approach is also inadequate to diagnose the cell that has a certain problem under specific conditions unless all cells are 3-electrode cells.

In addition to cycle/calendar characteristics, low temperature causes deleterious degradation. Basically Li deposition in the anode tends to happen at low temperatures. High rate charge also has the risk of Li deposition [22], although this high charge capability, particularly at low temperatures, is one important requirement that determines the charge balance of the power supply in HEV [23]. As the operating potential of graphite anode (0~0.5V vs. Li/Li^+) is close to the Li metal potential, it is generally

explained that low anode potential made by large overpotential due to high rate charging, especially at subzero temperatures, leads to Li deposition. Such Li deposition causes the permanent capacity loss within a short time, unlike the above cycle life degradation [24]. To avoid Li deposition is one of critical issues in automotive application required to guarantee 15-year life.

Few studies have, however, been reported because these severe charge conditions are not allowed in present application of portable electronics. Without introducing detail threshold value of Li deposition, some papers roughly mentioned that Li deposition occurs when anode potential is below a certain anode potential like 65mV [16] or 0V [24] (vs. Li/Li^+) using home-made 3-electrode cell. However, they did not prove anything resulting from Li deposition after Li-deposition suspected charge. Smart *et al*. [25] presented one method of determining if Li deposition happens as a result of the charge employed at low temperature by analyzing the potential profile of the subsequent cell discharge. They suggested that the potential plateau preceding the usual discharge profile is evidence of Li deposition [26]. This is also qualitative analysis without threshold value. Recently, Harris *et al*. introduced in situ measurement of Li intercalation and deposition in graphite by directly watching color change of lithiated graphite (Li_xC_6) electrode according to Li concentration [27]. Although it is useful to understand intuitively Li deposition following Li intercalation, it still does not offer a threshold value of Li deposition.

The limiting factors of charge capability not inducing Li deposition at low temperature are still subject to many arguments, among these being solid electrolyte

interface (SEI) layer, charge transfer resistance, lithium diffusion, even though electrolyte conductivity is excluded [22]. Fan *et al*. [22] argued that deposited lithium does not diffuse into the graphite anode during 4 hours at -20^{o}C while it is fast at room temperature so that Li solid diffusion inside the graphite is the rate limiting factor. Zhang *et al*. [28] suggested that charge transfer resistance is the limiting factor at low temperature. Smart *et al*. [29] concluded that SEI layer is the dominant factor with various kinds of electrolytes. Each of them is to some extent helpful to understand Li deposition phenomenon. In practical application for the electric vehicle, such conceptual explanation is, however, insufficient because vehicle operation should be controlled fast and dynamically. Detail threshold parameters and their values are essential.

Not only low temperature but also elevated temperature affects battery performance. Electrochemically high temperature enhances kinetics of charge transfer but is not chemically favorable for material stability. For example, metal dissolution in the cathode is well known, especially at high temperature, for causing crucial capacity fading due to loss of active material. Moreover, these dissolved metal ions move to the anode and are incorporated in SEI layer growth, which leads to cell impedance rise [8]. As thermal stability between charged cathode material and electrolyte depends on chemical composition of cathode materials, comparative studies have been researched [6]. Abuse tolerance of automotive Li-ion batteries is more severe than acceptable abuse tolerance of the small Li-ion battery [30]. Thus thermal model development as well as experimental proof has been studied [31, 32]. The final barrier remaining is cost reduction to $20/kW, which is beyond degradation study and thus it is not dealt with here, even though cost may be most important to incorporate Li-ion batteries into electric vehicles.

1.2. Motivation

Predictable degradation could be solved by selecting alternative active materials. Promising candidates to replace $LiCoO_2$ as cathode material of Li-ion batteries are $LiNi_{1/3}Co_{1/3}Mn_{1/3}O_2$, $LiMn_2O_4$, $LiNi_{0.8}Co_{0.15}Al_{0.05}O_2$, and $LiFePO_4$. Each material has each advantages and disadvantages, which can be employed according to manufacturers' strategic decision. Graphite is now mainly used as the anode of Li-ion batteries among other candidates such as hard carbon, metallic Li alloy material and $Li_4Ti_5O_{12}$. Although hard carbon shows higher gravimetric capacity than graphite, its density is lower by 30% than graphite. Initial coulombic efficiency is a broad range of 60~80%, while commercial battery-grade graphite shows 95%. There is not much benefit in energy density compared to graphite anode. Metallic Li alloy materials including Si have been extensively studied for next generation anodes to increase energy density. The most challenging problem of volume change up to 400% during cycling has persisted for the past few decades. $Li_4Ti_5O_{12}$ is an attractive material as known zero-strain material, i.e. no volume change during cycling, and has high electrochemical potential (1.55V vs. Li/Li^+), which can avoid SEI layer formation as well as Li deposition. By contrast, this high anode potential reduces full cell potential providing only 2V-class Li-ion battery. Hysteresis problem during high rate cycling has also recently been reported, which is a barrier in fast and dynamic operation in electric vehicles [33]. To conclude, although graphite is most susceptible to Li deposition due to proximity of its reversible potential to Li metal [26], there is not much alternative, especially in automotive application, contrasted with cathode materials.

The motivation of this dissertation is to investigate anode degradation, specifically Li deposition in the carbon anode, because it may be inevitable under fast and dynamic operating conditions in automobiles. Although deposited lithium causes serious capacity loss so that it is a high priority issue, the mechanism of Li deposition is still not established qualitatively or quantitatively. In order to examine this mechanism, a reliable diagnostics tool is introduced using a 3-electrode cell system made with a commercial 18650 Li-ion cell in Chapter 2. This analysis, unlike existing methods, enables us to not only monitor individual electrode potentials but also to measure cell temperature, which can offer thermodynamic and kinetic parameters of each electrode as a function of temperature for fundamental study. In Chapter 3, the mechanism of Li deposition is proposed as the concept of anode particle surface saturation, which is validated through experiment and modeling by obtaining critical charge capacity for the onset of Li deposition at given charging circumstances. Chapter 4 describes Li deposition–free, novel pulse charge protocol employing thermal effects at low temperatures. Finally, the conclusions drawn from this study are summarized and future work is suggested in Chapter 5.

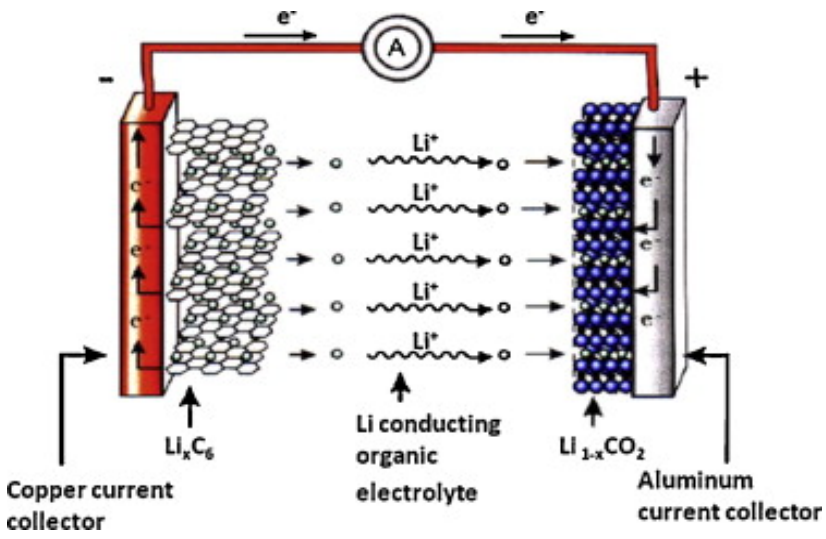

Figure 1-1: Scheme of working principle of a Li-ion battery on discharge. Taken from [34]

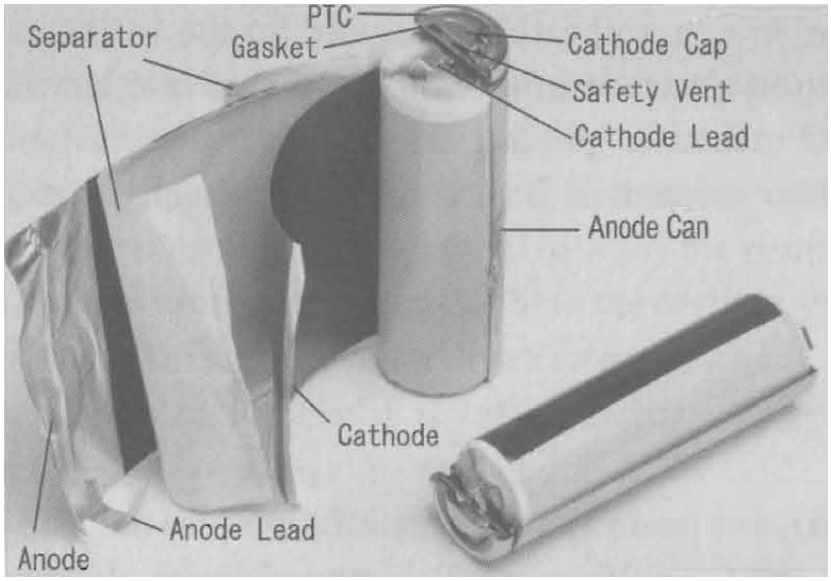

Figure 1-2: Internal structure of an 18650 cylindrical Li-ion battery. Taken from [35]

Chapter 2

Diagnostics of Automotive Li-ion Cells

Based on a newly designed 3-electrode cell system, thermodynamic and kinetic parameters of cathode and anode were studied and measured as a function of state of charge (SOC) and temperature. In this work, various tests were conducted using automotive 18650 cylindrical Li-ion cells. The experimental method and results can be utilized in diverse areas such as: (1) performance characterization; (2) studies of degradation mechanisms of each electrode; and (3) validation of electrochemical models.

2.1. Experimental

Commercial 18650 cylindrical cells were used for this study. These cells were originally designed and available for high power applications such as hybrid electric vehicles and power tools. They could be hereinafter called automotive Li-ion cells. Nominal capacity and potential of these cells show 1.2Ah and 3.7V where maximum cell potential of 4.2V and minimum cell potential of 2.5V are applied. Chemistries and electrical characteristics of these cells are summarized in Table 2-1.

A Li reference electrode was inserted into 3-electrode cell holder in order to obtain each cathode and anode potential separately [36]. This 3-electrode cell was assembled in an argon-filled glove box where both oxygen and water levels must be maintained less than 1ppm. First, a cylindrical cell was fastened in 3-electrode cell holder

and a tiny area of the bottom side of the cell was carefully cut without any damage of wound electrodes. Next, the surplus electrolyte was poured into the holder, followed by installation of a Li metal chip as the reference electrode. The Li metal was strongly adhered onto a thin Cu wire that enables us to lead a line to measure reference potential outside 3-electrode cell holder. In addition, a thermocouple was inserted into 3-electrode cell holder in order to monitor temperature behavior. The thermocouple was placed on the surface of the cylindrical cell as closely as possible. Finally, the 3-electrode cell holder was sealed tightly, and is not permitted to contact air and water after removal from the glove box.

All experiments were carried out under the isothermal condition. A Tenney Environmental Chamber (Series 942) was used to provide a constant temperature environment for all tests. Prior to each test, all cells were allowed to rest at the chamber temperature for at least 2 hours in order to reach thermal equilibrium, which can be checked by installed thermocouple connected to a digitalized thermometer outside the chamber.

An Arbin BT2000 battery testing system was employed for capacity measurement, galvanostatic intermittent titration technique (GITT) and pulse test. Two auxiliary voltage channels were used for monitoring each cathode and anode potential versus the Li reference electrode. Temperature data obtained from installed thermocouple were converted into analogue voltage data with Omega® thermocouple thermometer (Model 650) with a function that can convert from input temperature data of $\Delta 1^{o}C$ to output voltage data of $\Delta 1mV$. Another auxiliary channel was simultaneously used for

measuring these voltage data from thermometer. These three auxiliary channels were subordinately operated under one main host channel that was programmed to apply either a certain current or potential to the test cell.

Solartron SI 1287 Electrochemical Interface and SI 1255B Frequency Response Analyzer, controlled by a personal computer using Zplot® software, were employed to make electrochemical impedance spectroscopy (EIS) measurements. First using the Arbin tester, the cell was fully charged with 1C rate at 25°C and discharged at 1C rate until a specific SOC and held for 1 hour to reach a stable OCP. Then electrochemical impedance was measured by applying 5mV of AC (alternating current) oscillation over the frequency range form 50kHz to 5mHz.

2.2. Charge/discharge test

In order to measure a cell capacity, all cells were tested by a constant-current/constant-voltage (CCCV) charge and a constant-current (CC) discharge procedure, namely the Li-ion cell was charged at a constant current until the voltage reached to 4.2V, followed by holding the voltage at 4.2V until the current dropped to 0.1A. Then the cell was discharged at constant current to 2.5V. Each 10-minute rest step was employed after termination of each charge and discharge. The cells that showed an identical capacity were selected before all experiments were started.

Figure 2-1 shows the comparison of 1C charge/discharge curves at 25°C before and after making the 3-electrode cell. Both cell potential profiles as well as charge/discharge capacity are consistent to each other, meaning that there was no

disturbance of cell operation after installing the Li reference electrode and pouring extra electrolyte into 3-electrode cell holder. Figure 2-2 shows the normal 1C charge/discharge curve and temperature behavior of the 3-electrode cell at 25^{o}C, which is typical information from our 3-electrode cell system. During cycling, we can measure cell potential, cathode potential, anode potential and cell temperature respectively. Cathode potential minus anode potential (open circle in Fig. 2-2), theoretically defined as cell potential, shows good agreement with independently measured cell potential (solid line in Fig. 2-2). In addition to 1C rate test, higher C-rate test up to 10C rate also shows consistent result between measured cell potential and theoretical cell potential (each open symbol in Fig. 2-3) as shown in Fig. 2-3. Although it is sometimes a concern that placing a reference electrode inside the cell impacts the current distribution, followed by affecting potential measurement [37], our 3-electrode cell system enables us to supply reliable potential behavior of each electrode even under high C-rate cycling.

Not only individual electrode potential, but also cell temperature is important to determine the performance and safety of the automotive Li-ion battery because the automotive operation requires high current and/or high power cycling and dynamic condition. In Fig. 2-2, no temperature change is shown in 1C charge/discharge case. However, Fig. 2-3 shows temperatures rise in 2C, 5C and 10C charge/discharge. As C-rate increases, the cell temperature increases fast and reaches higher temperature. This phenomenon results mainly from electrochemical reaction heat directly related to high current [38], which should be understood as electrochemical-thermal interaction of Li-ion batteries. On the other side, after 10C discharge and rest, the cell temperature decreases during charging with 1C rate. This means heat generated in case of 1C rate is small and

can be readily dissipated to the ambient fixed at 25^{o}C. In Chapter 4, we introduce detailed thermal behavior according to C-rate and ambient temperature in order to find out how electrochemical-thermal interaction is related. Additionally an electrochemical-thermal (ECT) coupled model of Li-ion batteries has been developed in our group [39-41]. A previous work validated this temperature rise at various C-rate tests with computer simulation that matched well with these experimental results [42].

2.3. Open circuit potential (OCP) versus state of charge (SOC)

OCP is one of the important thermodynamic data, which is often considered equivalently as equilibrium potential. Basically this OCP variation according to SOC is determined by Gibbs Phase Rule as follow:

$$F = C - P + 2$$

where C is the number of component present, P is the number of phases present in material system and F is the number of degrees of freedom; i.e. the number of intensive thermodynamic parameters that must be specified to define the system and all its associated properties, one of which is electrochemical potential [43].

It is well known that graphite shows staging phenomenon during Li intercalaction/deintercalation [44, 3]. On each stage change, there is a potential plateau. By applying above phase rule, P is 2 as different stages coexist. C is also 2. Therefore F is equal to 2, which means that values of two intensive thermodynamic parameters, e.g. temperature and pressure, are specified so that no degrees of freedom are left and residual F is zero. Thus electrochemical potential should be flat. On the other hand,

layered lithium metal oxide during Li insertion/deinsertion shows that P is 1 because it is known for solid solution reaction. C is still 2 because reaction is progressed and then F becomes 3. So residual F is 1, which means potential is not fixed but varies depending on other parameter, such as Li concentration. It can be easily converted to state of charge (SOC) in the cathode material. Overall, the variation of full cell potential is dependent on that of cathode potential as a function of SOC. Hence OCP has been generally used to determine the SOC of Li-ion batteries. It is especially important for the fuel gauge of electric vehicles.

Two methods for OCP measurement were considered; one is linear interpolation method and the other is voltage relaxation [45]. First, in the case of linear interpolation method, we measured each electrode potential using low-rate scan at 25^{o}C. The average of potentials during forward and reverse scans yields not only full cell OCP but also each cathode and anode OCP. Figure 2-4(a) shows the charge/discharge curves obtained at 0.1C and their average value. The other method was followed by FreedomCAR manual [46]. This method can be broadly called Galvanostatic Intermittent Titration Technique (GITT). From SOC 100%, 1C current for 3 minutes and rest for 30 minutes were alternatively executed until cell potential reached 2.5V, as shown in Fig. 2-4(b). This 1C discharge for 3 minutes indicates SOC decrease of 5%. At the end of each rest time, full cell potentials, as well as cathode and anode potentials, were recorded. OCP versus SOC were calculated by interpolation of recorded potentials. In sum, both results of OCP measurement show practically no difference as shown in Fig. 2-4(c).

Although the two methods above yield the same result, voltage relaxation can supply other useful data about Li diffusion coefficient. Thus further tests according to temperature were conducted with GITT method, as shown in Fig 2-5. Before GITT according to temperature, test cells were charged at 25^{o}C in order to meet the same starting condition of SOC 100% and then ambient temperature was changed to various temperatures. As temperature was lowered, cell potential reached 2.5V earlier due to internal resistance elevation including charge transfer resistance and electrolyte conductivity etc. Thus OCPs of low SOC levels, below 10%, at low temperatures were not calculated because SOC level was based on 25^{o}C data. In order to get full data, lower rate discharge could be applied. But as it should take a long time and main available SOC range of electric vehicle was located above SOC 10%, another action was not taken.

As shown in Fig. 2-6, full cell OCPs show a little difference according to temperature [47]. But cathode and anode OCPs are slightly changed. This is related to the reversible heat associated with the entropy change of the each electrode reaction where the entropy change is defined as the variation of OCPs with temperature [48]. Interestingly, as the degree of change of both electrodes is similar, overall change of full cell OCP is nearly not observed [48]. Figure 2-7 summaries the tendency of OCP variation as a function of temperature, which is used in energy balance equation to study thermal behaviors of Li-ion cells in Chapter 4.

2.4. Lithium diffusion coefficient

Li diffusion inside active material particles is one of the critical transport processes in Li-ion battery performance. Huggins reported various methods to determine Li diffusion coefficient by electrochemical relaxation technique [49]. As most methods require complicated material data such as molar volume, the variation of OCP with Li concentration, surface area etc, many published papers show different values or orders of magnitude of Li diffusion coefficient [3, 50]. Moreover, it is much more difficult to measure Li diffusion coefficients of commercial Li-ion cell because the abovementioned material information must remain highly confidential. A simplified expression was, however, already reported using GITT method under a few assumptions by Huggins [49, 51, 52]. The Li diffusion coefficient inside solid (D) is defined as:

$$D = \left[\frac{4x^2}{\pi t}\right]\left[\frac{\Delta E_s}{\Delta E_t}\right]^2 \quad \text{if} \quad t << (x^2/D)$$

where x is the particle radius of active material, t is the time duration of the current step, ΔE_s is the change in OCP resulting from the current pulse, and ΔE_t is the total transient voltage change after eliminating the IR drop. The potential change during GITT test is typically shown in Fig. 2-8(a). Li diffusion coefficients of cathode and anode were calculated from this simplified equation. In order to utilize this equation, the OCPs versus $\sqrt{t}$ should, however, be theoretically a straight line during time of applying current (t) [51]. As shown in Fig. 2-8(b), this assumption was met. As we do not need material information in this equation, this method is expected to be widely used for diagnostic study of Li diffusion coefficient. Using one test cell combined with our 3-electrode cell

system, we can simultaneously obtain Li diffusion coefficients of both cathode and anode in one system even if detail material data were veiled. One more advantage of this method is that OCPs and Li diffusion coefficient were concurrently obtained by only one GITT test as a function of SOC.

Figure 2-9 shows Li diffusion coefficient of each electrode according to SOC at 25^{o}C. While Li diffusion coefficient of the cathode is independent of SOC, that of the anode strongly depends on SOC. It is believed that the ordering of the host and intercalate layers affects diffusion of Li^{+} ions in graphene layers [3]. These data were used for validating our ECT model in previous work [42]. Figure 2-10 shows the temperature dependence of Li diffusion coefficient. The diffusion coefficients of both electrodes have a decreasing tendency along with temperature. This trend explains slow kinetics of Li-ion cells at low temperatures. Based on this experimental result, we propose a mechanism of Li deposition that is one of the current issues in order to extend battery life in Chapter 3.

2.5. Internal resistance

Internal resistance is an important parameter to understand kinetics of the Li-ion cell because it is the result of overpotential arising from electrochemical reaction and usually used for evaluation of power performance [46]. In order to interpret internal resistance, two methods, AC measurement (EIS test) and DC measurement (pulse test), are complementarily used. EIS is analyzed with a certain equivalent circuit model including resistance, capacitance and inductance etc, while DC method calculates simply resistance value from potential change (ΔV) divided by applied current (ΔI) without

separating resistance component. EIS has drawbacks, however, in that the equivalent circuit model is arbitrary and high current situation cannot be represented. In this section, we compare internal resistances of full cell as well as each electrode by employing both methods. Detail analysis is introduced on studying thermal behavior in Chapter 4.

As shown in Fig. 2-11, pulse test at 25^{o}C was conducted at various SOC levels. From resistance calculation explained in Appendix A, Table 2-2 summarizes discharge and regen resistances at 1s and 10s pulse test, respectively. Both resistances show similar values regardless of SOC and C-rate, which means charge/discharge processes are highly reversible and responsive at fast and dynamic operation within a given reaction time. Most variation of cell potential arises from cathode potential change rather than anode side. The amplitude of cell potential change consists of cathode portion of 80% and anode portion of 20%, which can induce $R_{\text{fullcell}} = R_{\text{cathode}} + R_{\text{anode}}$ at a constant-current pulse. Similarly, as shown in Fig. 2-12(b), the sum of cathode and anode impedance spectra is yielded by adding the figures of their real and imaginary components at each frequency, which is closely overlapped with impedance spectra of full cell. Therefore both pulse test and EIS test using our 3-electrode cell can provide individual internal resistance components that consist of total internal resistance of full cell, which can be a useful tool to diagnose performance or degradation of Li-ion cells and to validate the electrochemical model [53]. In 25^{o}C test, the cathode side mainly determines this internal resistance of full cell, which indicates that electrochemical reaction in cathode is the limiting step.

There is no large variation according to SOC, as shown in Fig. 2-11 and Fig. 2-12. However, the temperature effect of increasing resistance was observed in Fig. 2-13. The profiles are similar but the amplitude of potential change is strongly dependent on cell temperature. Table 2-3 summarizes total resistances and each contribution of resistance rise according to the temperature. As the temperature decreases, anode portion of overall resistance is enlarged, which shows good agreement with EIS test as seen in Fig. 2-14. As the temperature is lowered, arc of anode impedance spectra, generally known as charge transfer resistance component, is much larger than that of cathode while smaller at 25^{o}C. As a result, internal resistance of the anode is much more strongly dependent on temperature than that of the cathode. This trend is also observed in Li diffusion coefficient in Fig. 2-10. Therefore sluggish kinetics at low temperature can be explained with the anode effect. For low temperature study of the Li-ion battery, kinetics of the anode side should be examined.

Finally, pulse test at only 0^{o}C shows C-rate dependence of resistance listed in Table 2-3. It is believed that resistance decreases due to thermal effect at low temperature, which is studied detail in Chapter 4. Shortly, it is proved that pulse test (DC measurement) is closely comparable to real operation including heat generation, while EIS test (AC measurement) can separate charge transfer resistance from overall impedance spectra.

2.6. Summary

Novel diagnostic method is introduced. In thermodynamic parameter study, OCPs of each electrode as well as full cell were measured as a function of temperature from GITT measurement. Thus the entropy change, defined as OCP variation according to temperature, of each electrode was readily calculated. As cathode and anode OCPs were similarly changed as a function of temperature, full cell OCP variation seems to be constant ($-0.2\ \mathrm{mVK^{-1}}$). From the same GITT measurement, Li diffusion coefficients of cathode and anode were simultaneously obtained as a function of SOC and temperature without concern about material information. Using pulse test and EIS test, internal resistances were also complementarily measured as a function of SOC and temperature. While Li diffusion coefficient of the cathode is independent of SOC, that of the anode depends strongly on SOC, however both Li diffusion coefficients are dependent on temperature. Internal resistances of both cathode and anode are independent of SOC but depend critically on temperature. The anode has particularly strong temperature-dependence on Li diffusion coefficient and internal resistance.

Table 2-1: Chemistries and characteristics of 18650 cylindrical cells

Cathode material	$LiNi_{1/3}Co_{1/3}Mn_{1/3}O_2$
Anode material	Graphite
Electrolyte	1.2M $LiPF_6$ in EC/DMC
Active area of electrode	$970cm^2$
Maximum current	20A
Energy density	$102Whkg^{-1}$ ($266\ WhL^{-1}$)
Operating temperature	$-20 \sim 60^oC$

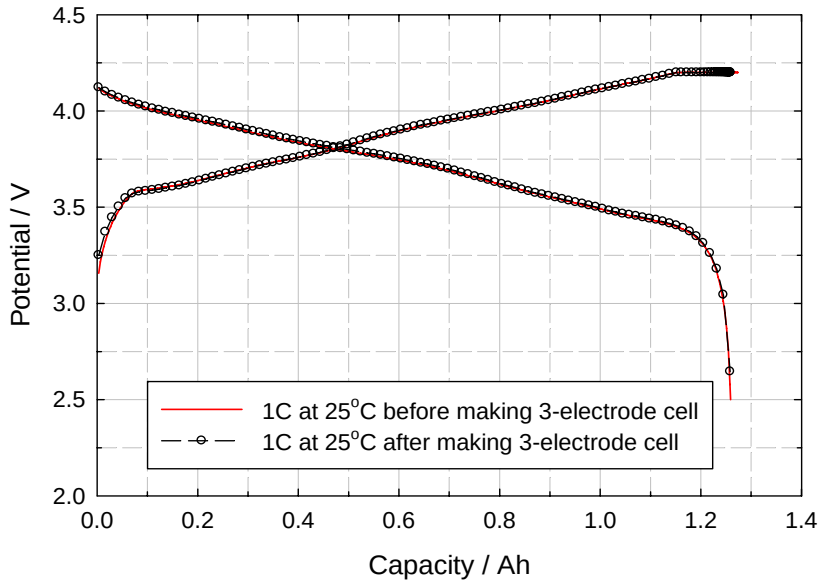

Figure 2-1: Comparison of 1C charge/discharge curves before and after making 3-electrode cell at 25°C

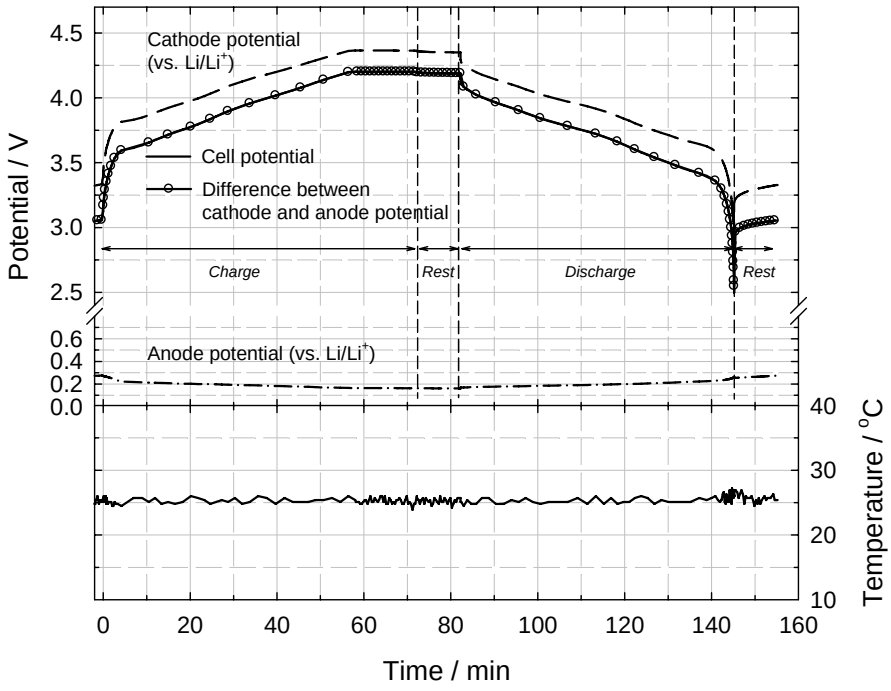

Figure 2-2: 1C charge/discharge curve and temperature behavior at 25°C

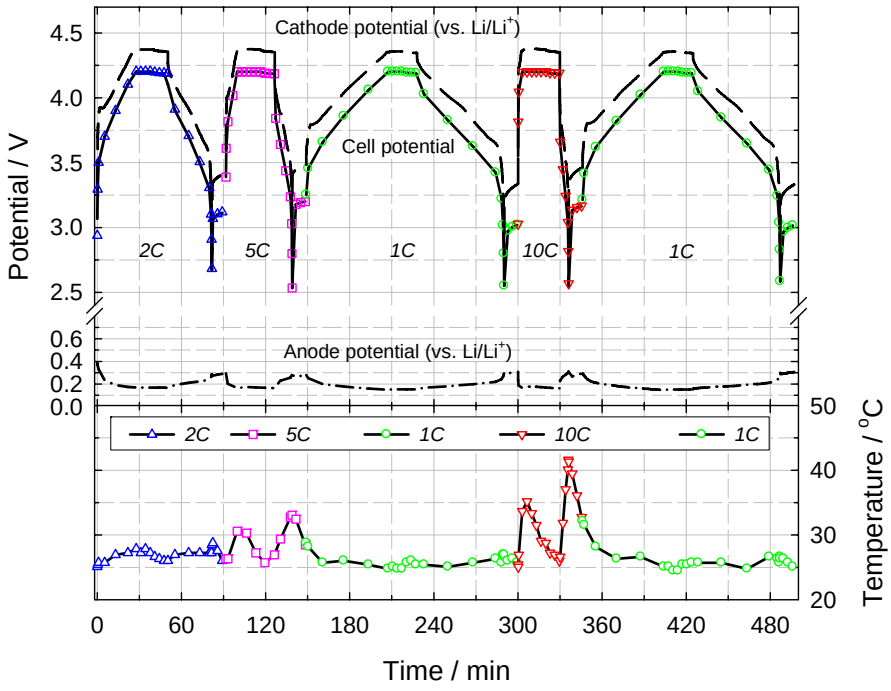

Figure 2-3: High rate charge/discharge cycling and temperature behavior at 25°C. Note that each open symbol indicates cathode potential minus anode potential in top graph.

(a)

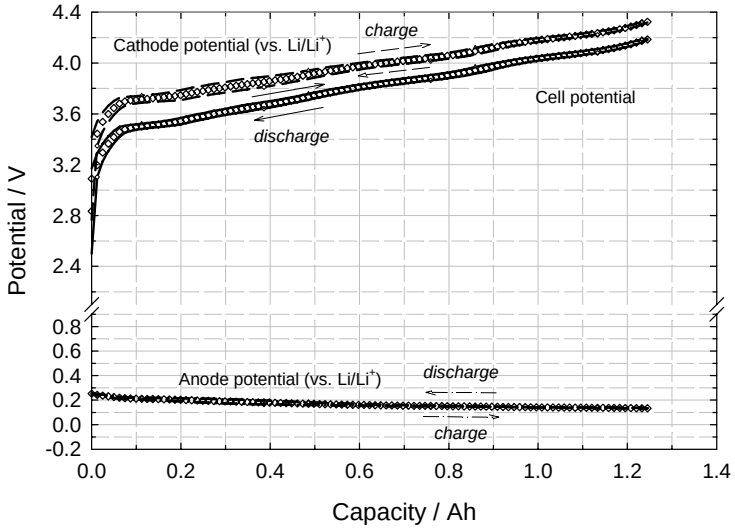
Cathode potential (vs. Li/Li+)
charge
discharge
Cell potential
Anode potential (vs. Li/Li+)
discharge
charge
Potential / V
Capacity / Ah

(b)

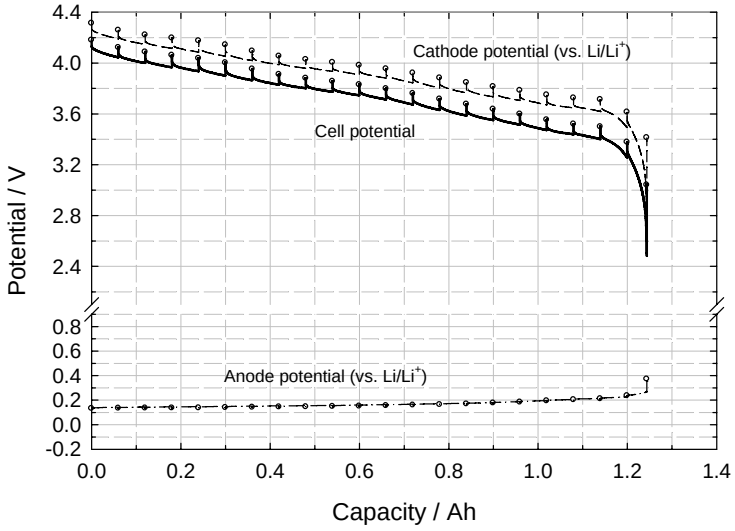
Cathode potential (vs. Li/Li+)
Cell potential
Anode potential (vs. Li/Li+)
Potential / V
Capacity / Ah

(c)

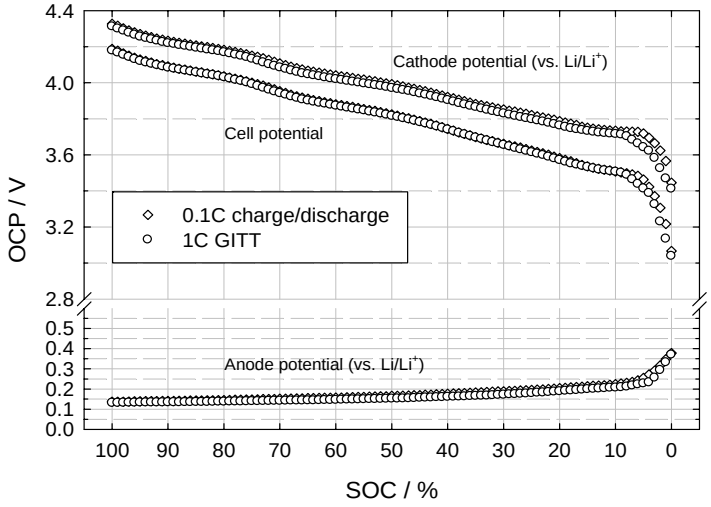

Figure 2-4: OCP measurement at 25^{o}C: (a) 0.1C charge/discharge profile, open diamonds (◊) indicate average value of charge and discharge potentials; (b) 1C GITT, open circles (o) indicate OCPs at each SOC; and (c) comparison of OCPs obtained by two methods

(a)

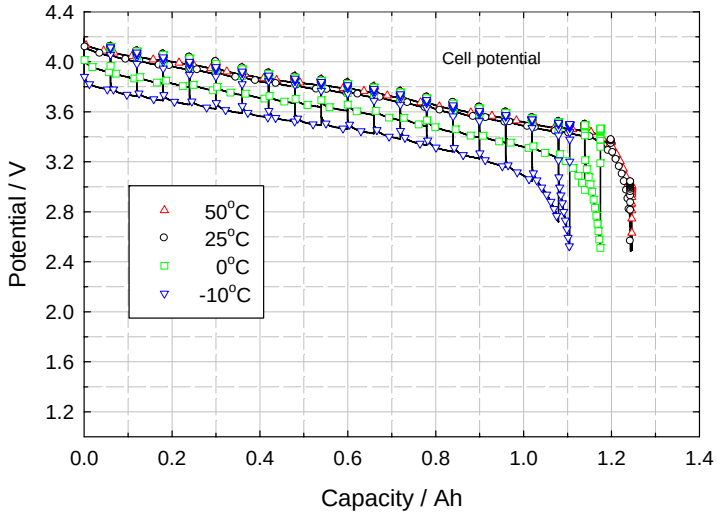

(b)

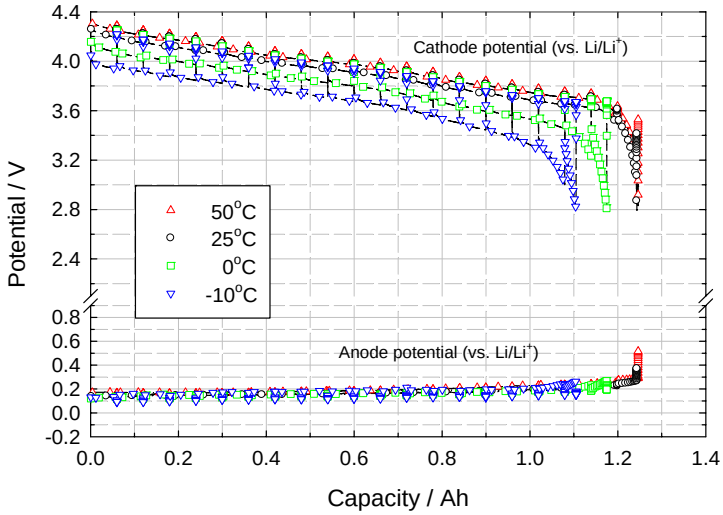

Figure 2-5: GITT tests according to temperature: (a) cell potential profile; and (b) cathode and anode potential profiles

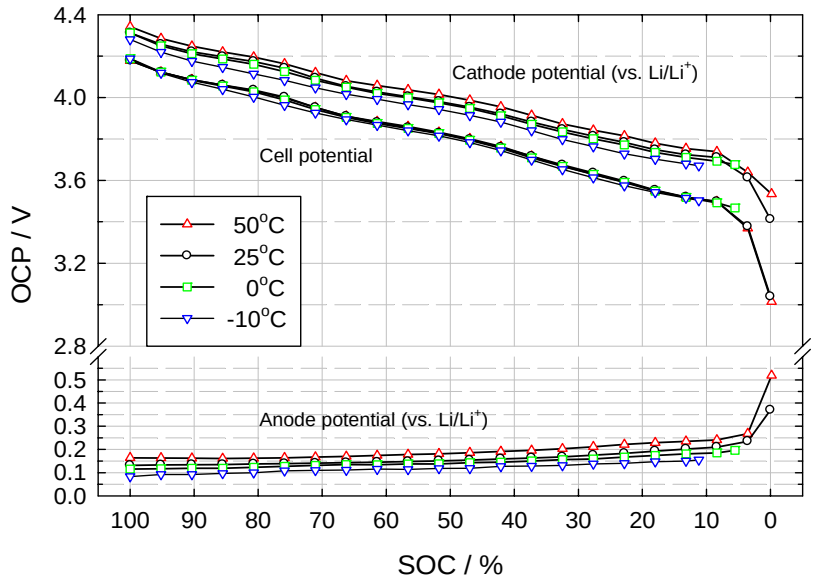

Figure 2-6: OCP versus SOC at various temperatures

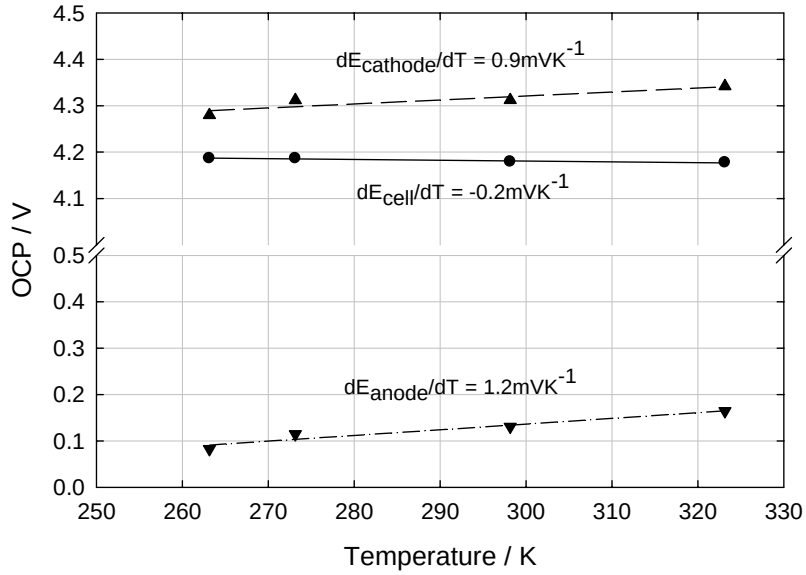

Figure 2-7: OCP variation according to temperature

(a)

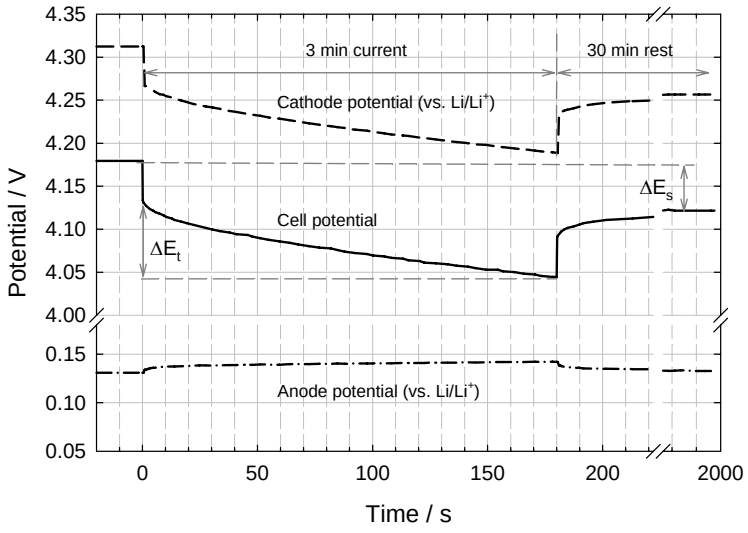

(b)

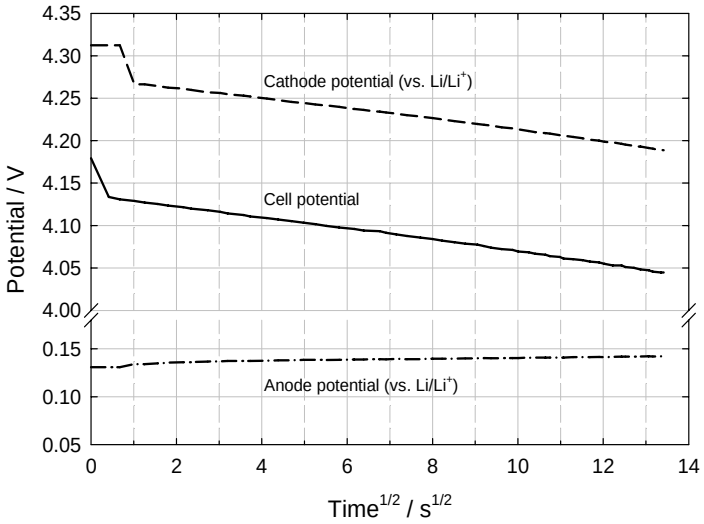

Figure 2.8: Electrode potential change during GITT test: (a) versus time; and (b) versus the square root of time

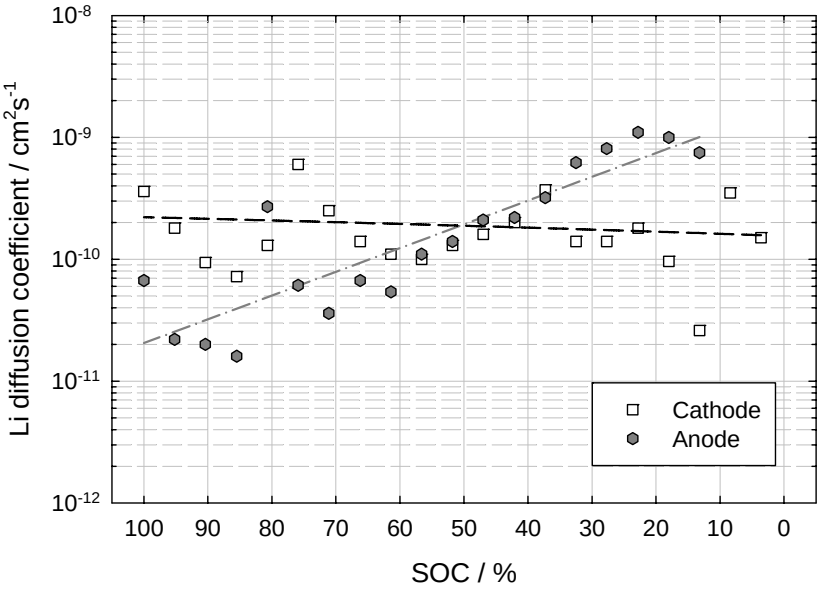

Figure 2-9: Li diffusion coefficients of both cathode and anode at 25^{o}C

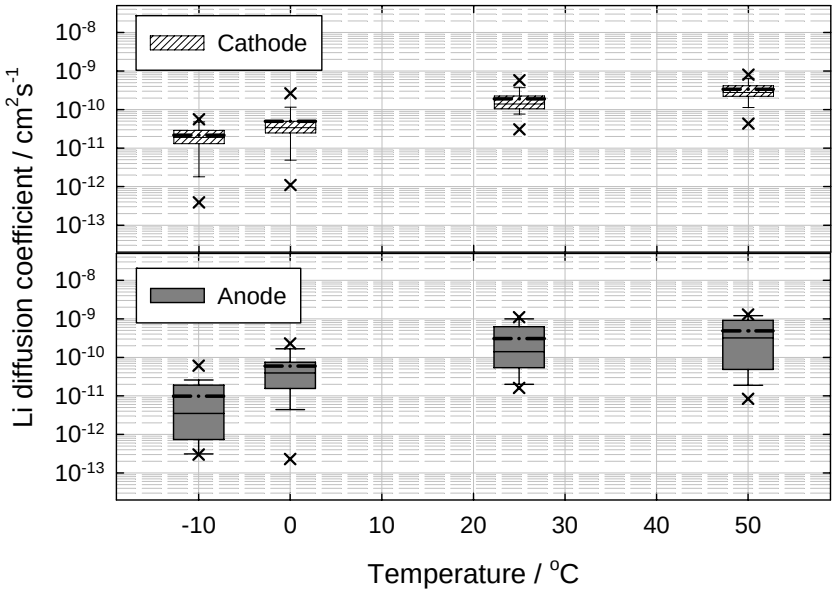

Figure 2-10: Li diffusion coefficients of both cathode and anode according to temperature; dash dot lines indicate the mean value

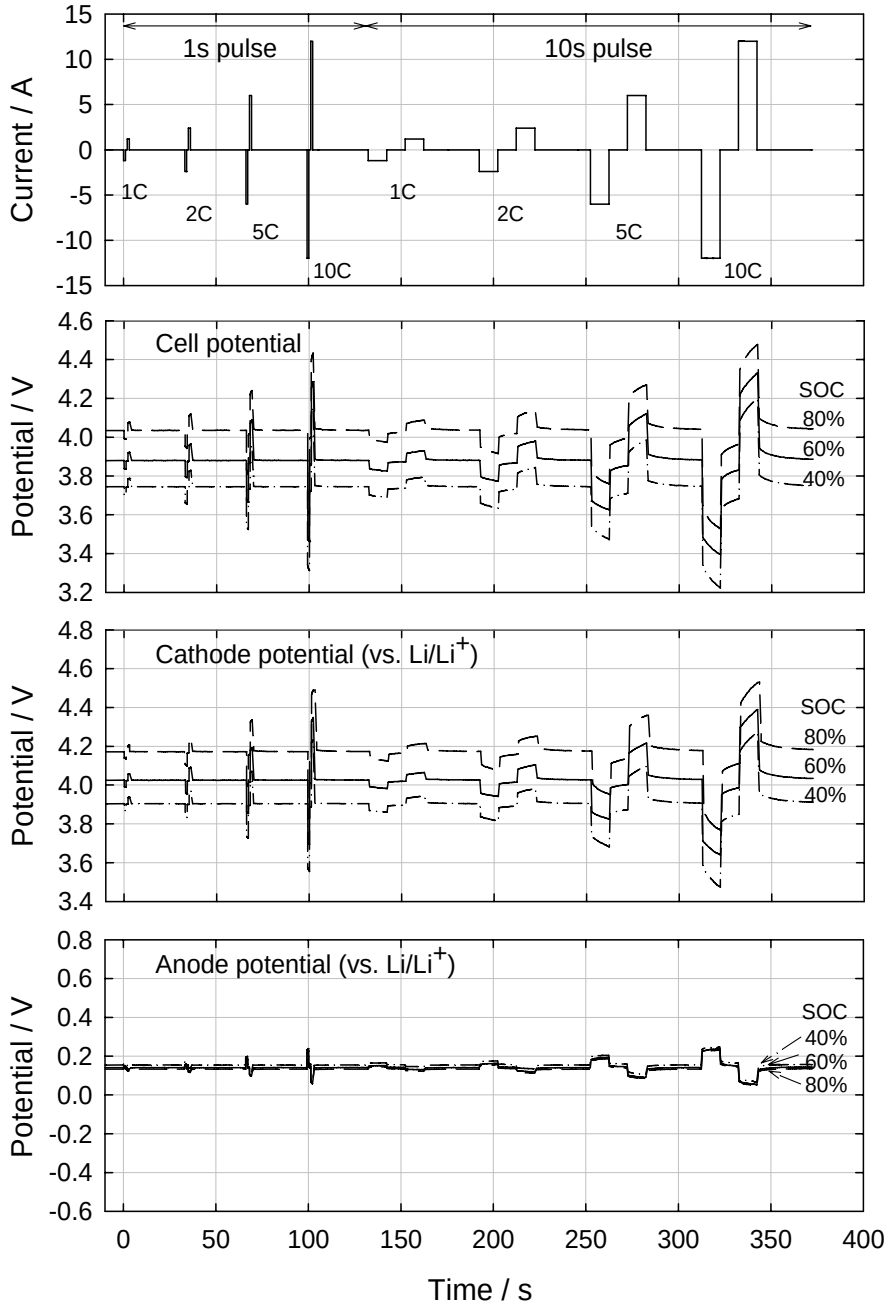

Figure 2-11: Pulse test at 25°C according to SOC

(a)

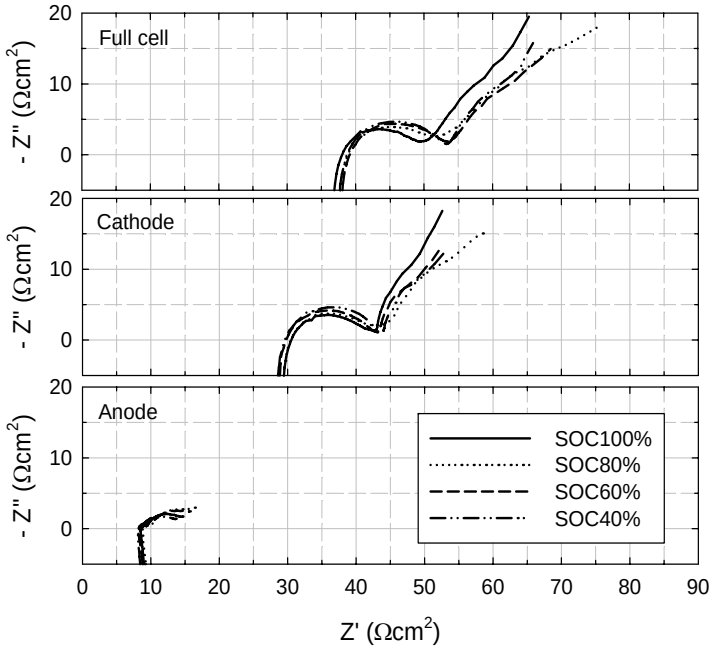

(b)

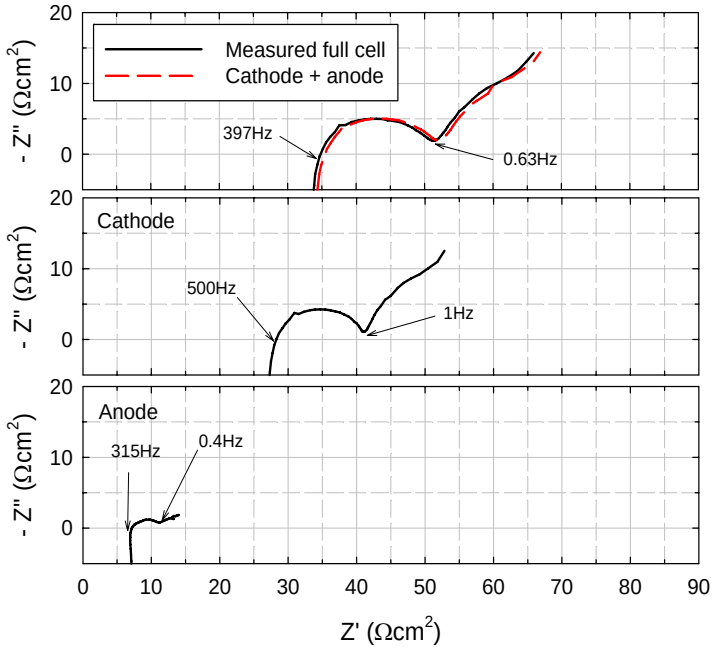

Figure 2-12: Nyquist plots at 25°C: (a) at various SOC levels; (b) sum of cathode and anode impedance in comparison with full cell impedance spectra

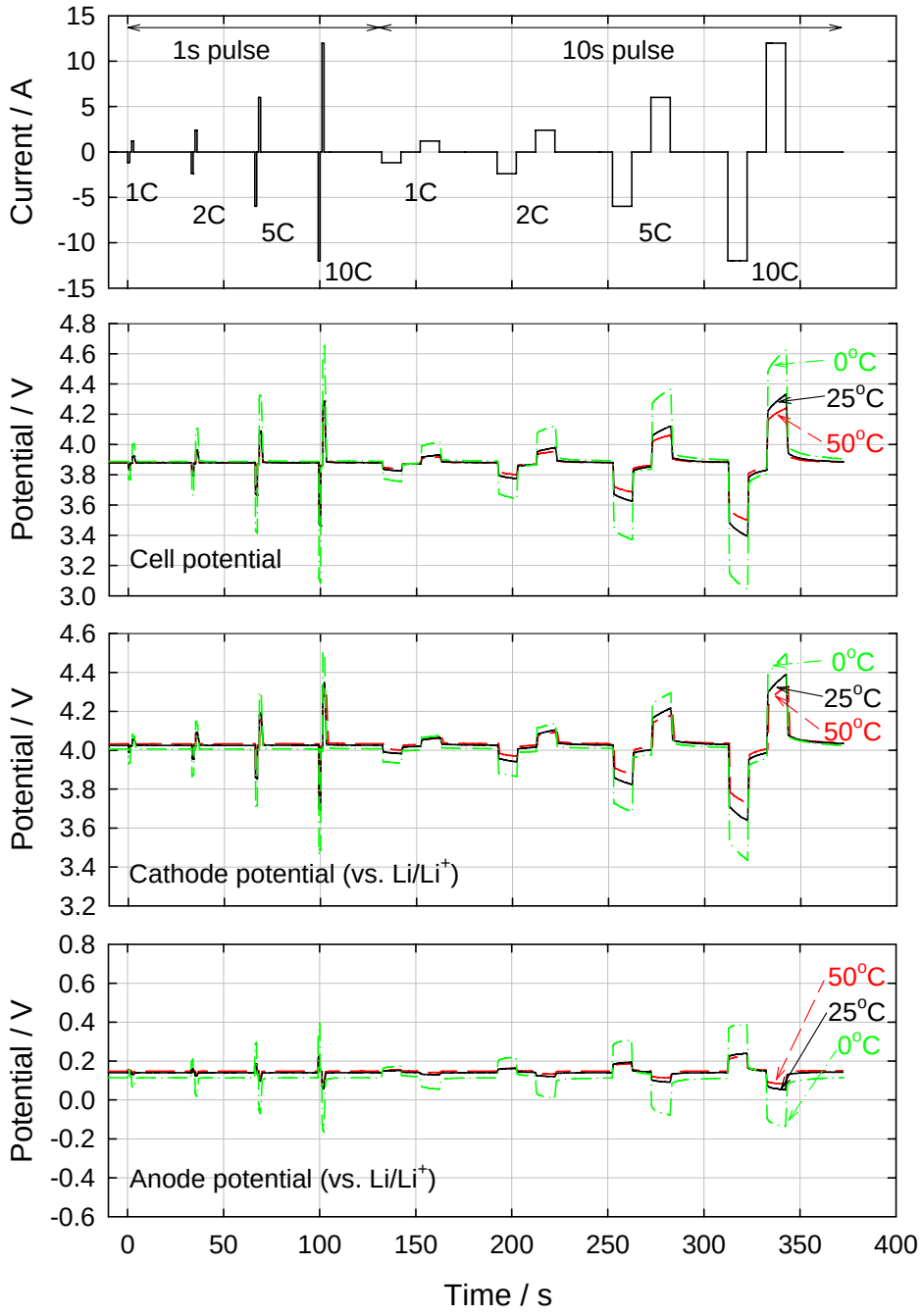

Figure 2-13: Pulse test at SOC 60% according to temperature

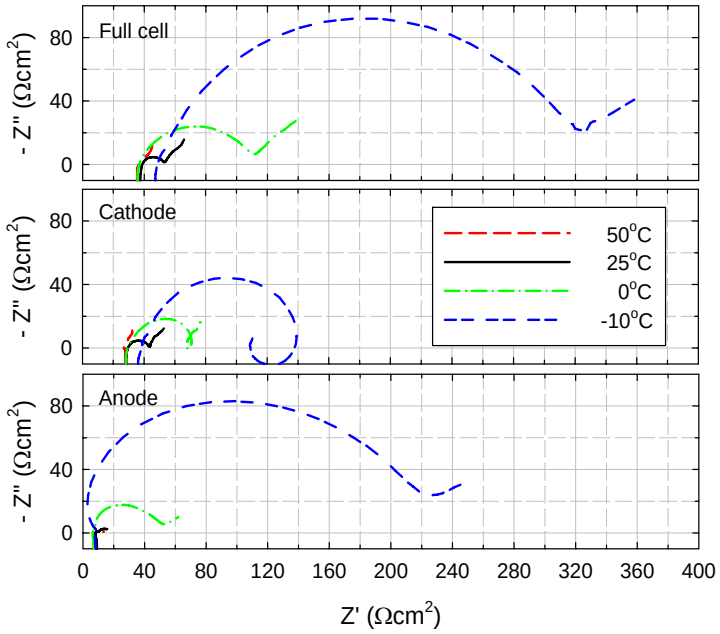

Figure 2-14: Nyquist plots at SOC 60% at various temperatures

Table 2-2: The discharge and regen resistances at 25°C for various SOC levels

25°C		1s pulse				10s pulse			
		1C	2C	5C	10C	1C	2C	5C	10C
SOC 80%	Discharge resistance (Ωcm^2)	37.8	36.9	36.9	34.9	50.4	48.5	45.6	41.7
	Regen resistance (Ωcm^2)	37.8	36.9	35.9	34.9	49.5	46.6	44.6	41.7
SOC 60%	Discharge resistance (Ωcm^2)	35.2	35.2	34.4	33.9	44.4	42.6	41.3	39.5
	Regen resistance (Ωcm^2)	35.5	35.5	35.4	34.4	46.6	45.8	43.3	40.4
SOC 40%	Discharge resistance (Ωcm^2)	35.7	35.7	35.8	34.9	45.0	44.7	44.1	42.4
	Regen resistance (Ωcm^2)	35.7	35.7	35.9	34.9	45.5	45.8	44.3	41.7

Table 2-3: The discharge and regen resistances at SOC 60% according to temperature. Note that the unit of resistance is ohmcm^2 (Ωcm^2). The numbers in parentheses stand for each electrode portion of resistance. Cathode and anode portion were calculated as each measured electrode resistance divided by discharge/regen resistance of full cell. The discharge/regen resistances were not exactly same values which are sum of cathode and anode resistances, but the values are almost similar (Δ= -0.7 ~1.5 Ωcm^2).

SOC 60%		1s pulse				10s pulse			
		1C	2C	5C	10C	1C	2C	5C	10C
50°C	Discharge resistance (Cathode % / Anode %)	25.4 (85.7 /19.5)	26.2 (80.8 /18.4)	26.0 (80.8 /19.6)	26.0 (80.6 /19.6)	32.3 (84.3 /18.4)	32.3 (81.3 /19.2)	31.3 (80.4 /19.8)	31.1 (80.7 /19.2)
	Regen resistance (Cathode % / Anode %)	25.9 (81.2 /21.0)	26.5 (79.0 /19.7)	26.7 (79.3 /19.9)	26.3 (80.0 /19.4)	33.9 (82.6 19.0)	32.8 (81.1 /19.2)	32.2 (81.7 /18.9)	31.7 (81.7 /18.2)
25°C	Discharge resistance (Cathode % / Anode %)	36.0 (79.1 /21.3)	35.2 (80.5 /21.1)	34.4 (80.0 /20.7)	33.9 (79.4 /20.6)	44.4 (79.1 /19.5)	42.6 (80.8 /20.9)	41.3 (79.5 /21.0)	39.5 (80.1 /20.1)
	Regen resistance (Cathode % / Anode %)	34.9 (82.9 /21.3)	35.5 (80.3 /20.9)	35.4 (79.7 /21.0)	34.4 (79.2 /20.7)	46.6 (79.7 /19.7)	45.8 (79.0 /20.0)	43.3 (79.7 20.1)	40.4 (80.6 /19.6)
0°C	Discharge resistance (Cathode % / Anode %)	96.8 (56.2 /43.7)	91.0 (57.2 /42.0)	76.6 (61.4 /38.2)	64.7 (65.1 /35.0)	108.5 (55.4 /44.7)	100.8 (57.3 /42.6)	84.3 (62.7 /37.5)	69.3 (67.9 /32.1)
	Regen resistance (Cathode % / Anode %)	98.4 (54.8 /45.8)	92.1 (55.8 /44.9)	76.9 (59.3 /40.9)	64.3 (62.8 /37.1)	113.8 (54.0 /46.3)	104.2 (56.0 /44.6)	85.4 (60.4 /39.9)	66.4 (65.7 /34.3)

Chapter 3

Lithium Deposition in the Carbon Anode

Lithium deposition in graphite anode is well known for causing permanent capacity loss of Li-ion battery, especially at subzero temperature and/or under high rate charge [22, 54]. In order to guarantee 15 years cycle/calendar life of Li-ion battery in electric vehicles, such Li deposition phenomenon must be avoided and controlled by a battery management system (BMS), principally through understanding mechanisms and threshold parameters. In this chapter, we aim to find threshold parameters and propose the mechanism of Li deposition.

3.1. Lithium deposition and capacity loss

Although many researchers have studied charging processes of Li-ion cells, little work elucidates the mechanism for Li deposition and introduces the threshold parameters [16, 24]. One reason is that under most portable electronic applications, severe charging scenarios such as low temperature charge and high rate charge seldom exist [22]. Therefore there have not been many studies on this Li deposition in electronic application, while these charging conditions could be critical issues in automotive application. The other reason has to do with methodology in that it is not easy to confirm whether Li deposition in the anode happens or not. The simplest way is to look directly into the anode surface of the Li deposition-suspected cell. Dismantling the suspected cell is

dangerous, however, because the anode of the Li deposition-suspected cell must be lithiated and may react fiercely with ambient atmosphere according to the degree of lithiation ($0 \le x \le 1$ in Li_xC_6) and then can catch fire, at worst. Additionally, as Jansen *et al.* already mentioned in their paper, the deposited lithium reacts quickly with the surrounding electrolyte in an attempt to form a SEI layer [24]. Lithium does not exist as a metal plating but rather, is consumed immediately in an attempt to form the passivation layer, or at the very least, does not have a firm electrical contact with the graphite matrix [24]. This lithium consumption causes the capacity loss from the next cycle [24]. Therefore even if we could get Li deposition-suspected anode without any accidents, it would be hard to see directly deposited lithium from real cell.

As we already know that capacity loss occurs when Li deposition happens, change of charge/discharge capacity before and after a certain charge process that induces Li deposition can be quantitatively observed as a diagnostic method to study Li deposition. Of course, any other factors could be thought to cause capacity fading even under mild operating conditions due to electrolyte decomposition, contact loss of active materials, current collector corrosion, and so on. Thus a normal cycle test with 1C rate was first conducted for 500 cycles in order to check original cycle performance of the test cell. As shown in Fig. 3-1, this test cell shows excellent cycle performance at 25^{o}C, maintaining the discharge capacity of 91% after 500th cycle and gradually linearly fading with -0.22mAh/cycle (equivalent to -0.02% of rated capacity per cycle) over several hundred cycles. It is noted that the state-of-the-art standard of cycle performance is more than 80% of capacity retention after 300th cycle with 0.5C rate in the Li-ion battery industry. Therefore we can assume that there is no capacity loss in this test cell under

normal charge/discharge test at 25°C within a few cycles in which all experiments about Li deposition in this dissertation will be conducted.

Figure 3-2(a) shows the comparison of 1C discharge capacities after 1C constant-current/constant-voltage (CCCV) charging until cut-off voltage of 4.2V as a function of temperature. The lower charge temperature is, the higher capacity loss was observed. But as the charge temperature is lowered even with same charge procedure, full charge capacity according to temperature also decreases slightly. Thus in order to compare the capacity loss under same condition, the charge/discharge capacity with normal 1C cycling was preliminarily measured at 25°C before all tests. In addition, each charge test was conducted at each specified temperature, followed by increasing temperature of environmental chamber up to 25°C and holding for 2 hours to reach thermal equilibrium between cell and environment. Then the cell was discharged to 2.5V at 25°C. Finally normal 1C cycle test at 25°C was repeated in order to check whether any capacity loss occurs. As shown in Fig 3-2(b), the charge/discharge curves show the same profile, which can be naturally expected because it is the same to above 25°C cycling in Fig. 3-1. But in case of 1C charge at low temperatures, each charge and discharge capacity decreases when compared to its original capacity as shown in Fig. 3-2(c) and Fig. 3-2(d). As charge temperature is lowered, the degree of capacity loss increases. After only one time charging at 0°C and -10°C respectively, each capacity loss of 4.5% and 11% was observed. Hereinafter the capacity loss is defined as:

$$\text{Capacity loss}(\%) = 1 - \frac{\text{Discharge capacity after a specific condition test}}{\text{Discharge capacity before a specific condition test}}$$

This capacity loss of 11% from -10^{o}C charge is even larger than the capacity loss of 9% after 500 cycles with 1C rate at 25^{o}C (Fig. 3-1). It is believed that this huge capacity loss results from Li deposition due to charge at low temperature. The following sections deal with this topic specifically.

3.2. Effect of anode potential

As shown in Fig. 3-3, 1C CCCV charge curves with cut-off voltage of 4.2V at 25^{o}C and -10^{o}C respectively are compared using a 3-electrode cell. During charging at -10^{o}C, every potential show larger overpotential than those of 25^{o}C charge. In particular, this large overpotential of the negative electrode leads Li deposition in the anode because anode potential reaches below 0V (vs. Li/Li^{+}) before charge is complete, as shown in Fig. 3-3(b). Thus Jansen *et al.* suggested it is necessary to lower the cell cut-off voltage on low temperature charges to a value less than 4.0V in order not to make anode potential drop below Li metal potential [24]. This could work to avoid Li deposition effectively at low temperatures, but it is not a fundamental solution. If cut-off voltage of 4.0V is applied to Li-ion cell at low temperature, charge capacity should be lowered, which indicates that available discharge capacity subsequently decreases. Another method that could be also suggested is much lower C-rate charge, for example 0.1C rate. But this method needs such extended charging time that it is inadequate for automotive application that requires fast and dynamic operation. Therefore the ultimate solution without such sacrifice as lowering cut-off voltage or C-rate should be studied. Threshold

parameters for the capacity loss due to Li deposition at low temperatures should be examined first.

Assuming Li deposition starts to happen below a certain anode potential, the threshold value was searched like existing method. Based on the charge profile of anode potential at -10^{o}C, three arbitrary points were selected. As shown in Fig. 3-3(b), 1C charge for 1000s and 2000s at -10^{o}C reaches anode potential of 50mV and 0V, respectively. Thus 1C charge for 1000s and 1C charge for 2000s were first conducted with each of two cells. As shown in Fig. 3-4(b), only 2000s charge at -10^{o}C shows the capacity loss of 3.3%, but no capacity loss was observed in 1000s charge at -10^{o}C in Fig. 3-4(a). Below anode potential of 50mV, Li deposition is suspected. To get a more narrow range of threshold value, 1C charge for 1000s and 1C charge for 1500s corresponding to anode potential of 20mV were conducted iteratively at the same temperature, as shown in Fig. 3-4(c). With one cell, one experiment set consists of 1C charge for 1000s at -10^{o}C and 1C charge/discharge cycle at 25^{o}C. After this one test set, 1500s charge test set was employed. Then 1000s charge test set was conducted again. Finally, 1500s charge set was tested. The first 1000s charge at -10^{o}C shows no capacity loss; but the next 1C 1500s charge at -10^{o}C induces the capacity loss of 2.5%. The next 1000s charge at -10^{o}C shows also no capacity loss, but the capacity loss occurs only in the case of 1500s charge. Interestingly, this tested cell was not affected by previous charge history. From the 1500s charge test, the cell showed a little capacity loss; but in the next 1000s charge test, the cell showed no capacity loss. It can be proved that deposited lithium from the 1500s charge did not exist by next 1000s charge test because it was consumed for a reaction like SEI layer formation. Only after 1500s charge test did capacity loss reoccur and the degree

of loss is also the same as shown in Fig. 3-4(c). It could be concluded that only charge for 500 seconds between 1000s (E_{anode} ~ 50mV) and 1500s (E_{anode} ~ 20mV) charge induces the capacity loss of 2.5% repeatedly.

Figure 3-5 shows result of two 3-electrode cell tests that were charged with 2C rate at -10^{o}C until anode potentials reached 50mV and 20mV, respectively. By monitoring anode potential during charging, when anode potential reached 50mV or 20mV, charge was stopped. 1C charge/discharge capacity was then checked at 25^{o}C. The anode potential cut-off of 50mV does not show capacity loss; only at anode potential cut-off of 20mV the capacity loss of 3.7% occurs.

In Fig. 3-6, 0^{o}C charge was employed with the same method. First, 1C charge at 0^{o}C was conducted until anode potential reached 50mV without capacity loss. Next test for anode potential cut-off of 20mV was planned. However, at 0^{o}C cell potential reached 4.2V first before anode potential reached 20mV, therefore 1C CCCV charge test was conducted instead. As the anode potential during 1C CCCV charging is also below 50mV, capacity loss of 6.6% was shown. As a result of the above three experiments, the anode potential of 50mV was tentatively considered as threshold value of Li deposition. This value is close to 65mV that Zhang *et al*. suggested [16].

Unfortunately however, this value is not universal at higher C-rate or different temperature. As shown in Fig. 3-7, two exceptions were observed, which is not explained by our assumption that is divided by two areas of Li deposition zone and Li deposition-free zone. In the case of 5C charge for 5min (0.5Ah) at -10^{o}C, anode potential was above 50mV, but showed capacity loss of 8.4% in Fig. 3-8(a). Interestingly, anode potential of

5C charge is higher than that of 1C charge at -10^{o}C, which indicates that anode overpotential of 5C charge is lower. This relation of overpotential and C-rate at low temperatures is discussed in detail in Chapter 4. Next, in the case of -20^{o}C charge, anode potential rapidly dropped to 0V when charge started. Surprisingly, even though it shows far below anode potential of 50mV, the capacity loss did not happen in the case of charge capacity cut-off of 0.1Ah. Only the charge capacity cut-off test of 0.2Ah shows a little capacity loss in Fig. 3-8(b). Therefore both experiments conclude that anode potential as universal threshold value is invalid to determine whether Li deposition happens or not.

Finally, Fig. 3-9(a) shows overcharge tests, typically above normal cell cut-off voltage of 4.2V, conducted at 25^{o}C. The overcharge of Li-ion battery literally means excessive reduction reaction of lithium on the anode (i.e. Li deposition) beyond Li intercalation reaction, regardless of temperature and C-rate. As a result, 4.5V CCCV overcharge shows only capacity loss, which explains that our Li-ion cells are designed in order to endure up to around 4.4~4.5V. This proves that N/P ratio, ratio of anode capacity over cathode capacity, must be designed with high value. This design factor of Li-ion cell is decided by manufacturers with their own design concept and objectives, which is not examined further in this chapter but introduced briefly, including basic design concept of Li-ion cell, in Appendix B. In summary, 4.5V overcharge induces the capacity loss of 5.4% in Fig. 3-9(c), which is believed to result from Li deposition in design of Li-ion cell [55]. At the end of 4.5V overcharge, the anode potential was above 100mV. Even if considering anode potential deviation as temperature rise in Fig. 2-7, the previous threshold value of 50mV at 0^{o}C or -10^{o}C should be placed as below 100mV. It does not

obey the initial assumption that Li deposition starts to happen below a certain anode potential.

3.3. Effect of charge capacity

Although a 3-electrode cell system is helpful to observe individual electrode potentials, anode potential cannot represent universal value for Li deposition. The reason is that measured anode potential is averaged value of whole anode area. Along electrode thickness, anode particles in separator side are under more severe charging condition compared to those in current collector side. Once Li deposition starts to occur locally in a short time, it is experimentally impossible to distinguish between Li deposition and Li intercalation reaction by measuring anode potential precisely. Moreover, two electrochemical potentials of both reactions are so close that it is difficult to know a reaction path that Li^+ ions will follow even when overpotential is large enough like 1C charge at -20^{o}C in Fig. 3-7. Thus, another measurable and controllable parameter, charge capacity, was selected. The charge capacity cut-off test was conducted instead of anode potential cut-off test.

Without considering any potential change and any upper or lower limit of voltage during charging, constant-current (CC) charge as a function of charge C-rate and temperature were conducted until the charge capacity reached a predetermined value. Then 1C discharge capacities at 25^{o}C were compared before and after this charge capacity cut-off test in order to check if the capacity loss happened. As with the anode potential cut-off test, 0.1Ah was initially selected for convenient calculation of charge

capacity. First 1C, 2C, 5C, 10C and 15C charge rate tests at 0^{o}C were employed. In order to charge 0.1Ah, each charging C-rate was conducted for 300s, 150s, 60s, 30s and 20s respectively. By varying the cut-off value of charge capacity, the values of capacity loss were summarized in Table 3-1 by comparison of 1C discharge capacities at 25^{o}C.

Charge capacity cut-off tests of 0.1Ah provided data of capacity loss from -0.6% to 0.5%. The value of 0.5% is same numerical result from 1C charge for 1000s at -10^{o}C. At that time, by comparing two discharge curves in Fig. 3-4(a), it was concluded that no capacity loss occurs. As a matter of fact, as shown in Fig. 3-1, little difference between charge capacity and discharge capacity is observed over cycles, which is equivalent to 0.3% of rated capacity. Numerically this value cannot explain the excellent cycle performance of our Li-ion cells that show 91% of capacity retention over 500 cycles. As the value of 0.3% indicates irreversible capacity resulting from a certain side reaction, only reversible capacity of 99.7% should be charged in the next cycle. After the 333rd cycle, reversible capacity, i.e. discharge capacity, should be zero, but is not in real cycle result. Thus this degree of difference was considered as experimental error in this work.

In order to analyze capacity loss quantitatively, a certain criteria value should be selected to divide into two conditions of capacity loss or no capacity loss. It should be noted that the capacity loss of 2% was determined under consideration of experimental errors and convenience of analysis, although this value of 2% is subjective and arguable. A critical value, here 2%, should be selected in this study. By comparing with a mathematical modeling result, this value can be accepted indirectly in Section 3.4.

As listed in Table 3-1, the value of capacity loss depends on charge C-rate and charge capacity. Lower charge C-rates in 1C and 2C do not show less than the capacity loss of 1% by charge capacity cut-off test of 0.5Ah. Higher charge C-rate tests of 10C and more exceed the value of 2% earlier, rather than lower charge C-rate tests. The degree of capacity loss is proportional to charge C-rate under same charge capacity cut-off test in the same column listed in Table 3-1. Also as charge is progressed further, i.e. higher charge capacity, the degree of capacity loss increases. Assuming that the degree of capacity loss is proportional to the amount of deposited lithium, the degree of Li deposition also depends strongly on charge C-rate and charge capacity.

For more quantitative analysis of capacity loss, contour graphs were plotted at various low temperatures as shown in Fig. 3-10. In the case of 15C test at 0^{o}C, the capacity loss of 0.3% and 3.6% were obtained from each 0.1Ah and 0.2Ah cut-off. Therefore a certain value between 0.1Ah and 0.2Ah may result in the capacity loss of 2%. The value of charge capacity cut-off cannot be easily obtained by above experimental method because it is a sort of trial and errors approach, which requires much time and many test cells. Therefore with existed data points, a contour plot can be used to determine the critical value of 2%. Each data point ($\times$) indicates that there are experimental results in Fig. 3-10. Red color was selected in the area where capacity loss of more than 2% happens. The borderline displayed with a dash line in Fig. 3-10 can be called critical charge capacity inducing Li deposition hereinafter. This critical charge capacity also depends highly on charge C-rate as well as temperature. Surprisingly, the critical charge capacity shows an asymptotic approach to 0.1Ah as charging C-rate increases up to above 10C, even at -20^{o}C charge test. In order to validate this value

experimentally, 20A charge tests, the maximum allowable current to apply our Li-ion cells, were conducted down to -20^{o}C. As shown in Fig. 3-11(b), the capacity losses after 0.1Ah charge at 0^{o}C, -10^{o}C and -20^{o}C are all negligible. More detailed analysis of this critical charge capacity is discussed in Section 3.4.

Another point is here called to attention in that the charge curves of 20A tests in Fig. 3-11(a) show much higher voltage than the 4.2V that is the normal upper limit on charge. Even if charge voltage shows more than 4.5V that induces overcharge in Fig. 3-9(a), there was no capacity loss after 0.1Ah charge at low temperatures as shown in Fig. 3-11(b), which proves again that lowering cell potential suggested by Jansen *et al*. [24] is not effective to avoid Li deposition. In addition, 20A test at 25^{o}C was conducted. Although cell potential during 20A charge is over 4.5V, the charge capacity cut-off of 1.0Ah at 25^{o}C induces capacity loss of 1.4%, but this capacity loss is much less than that of 4.5V overcharge test in Fig. 3-9(c). The important difference is that the charge capacity of 4.5V overcharge was 1.6Ah, that is, around 30% larger than 1C normal charge capacity in aspect of critical charge capacity. Thus it also proves that controlling the charge capacity is more effective rather than limiting full cell and/or anode potential. It is noted that above, both values of 0.1Ah at low temperatures and 1.0Ah at 25^{o}C are usefully employed in order to develop novel charge method that avoids Li deposition and simultaneously achieves fast charge at subzero temperatures in Section 4.2.

3.4. Mechanism of Li deposition

Returning to the working principle of Li-ion battery on charge, Li intercalation into graphite particles works by three steps: (1) mass transfer of Li^+ ions though electrolyte to the electrolyte-electrode interface; (2) charge transfer through SEI layer; (3) Li diffusion inside between graphene layers. To simplify our theory, staging phenomenon in graphite is neglected here. All processes depend strongly on temperature. Thus it is widely understood that as temperature is lowered, Li deposition is more prone to happen because sluggish kinetics of Li intercalation at low temperature induces Li deposition. But high C-rate dependence of Li deposition cannot be explained easily with the above temperature-dependent parameters.

Before dealing with kinetics of Li intercalation, we need to check thermodynamics. In reaction aspect of Li and C, lithiated carbon is thermodynamically stabler than deposited lithium on carbon inside Li-ion cell. Thus Li intercalation reaction into carbon happens first. But if the anode is fully charged with lithium, i.e. fully lithiated status (LiC_6), there is no empty site for lithium inside graphite and then surplus Li^+ ions from cathode side must be consequently reduced on graphite surface because two equilibrium potentials of Li intercalation and Li reduction, i.e. deposition, are very close. Actually this is an advantage of graphite as anode material compared to other candidate anode materials like lithium titanium oxide and 3d metal oxide in Li-ion cell because high cell potential, cathode potential minus anode potential, can be obtained due to lower anode potential of graphite. However, this small difference of equilibrium potentials is also a risk factor of Li reduction to metallic form. In sum, once lithium is fully

intercalated, i.e. saturated, in the anode, then Li deposition inevitably happens, which can be called overcharge case in other expression as shown in Fig. 3-9.

Here we make one scenario combined with thermodynamic and transport phenomena during charging. Fundamentally the particle surface is the focus rather than bulk because electrochemical reaction occurs on the particle surface: On charge, Li^+ ions should be moved on the particle surface and following charge transfer of Li^+ ions happens from the particle surface, then intercalated lithium diffuses inside graphite. By modifying above overcharge concept from bulk anode into the particle surface, the following scenario can be postulated: Once the anode particle surface is saturated with Li in any charging circumstances, no more Li^+ ions can be intercalated but should be reduced to metallic form on the anode particle surface. This deposition on graphite surface results in the permanent capacity loss in following cycle as mentioned in Section 3.1.

Therefore, it can be reasoned that the particle saturation depends on how fast the Li diffusion process is, which is also strongly dependent on temperature, as shown in Fig. 2-10. Therefore low temperature charge has the higher risk for Li deposition due to slow Li diffusion process that can block Li ions rushing into the anode surface. Li deposition occurs due to blocking Li occupied beneath the anode particle surface site even though lithium is not fully intercalated inside the bulk anode. In addition, high C-rate also has the risk of Li deposition for the same reason. If temperature-dependent Li diffusion process is relatively slower than the charge transfer rate of Li^+ ions determined by temperature and charge C-rate, particle surface can be also readily saturated, followed by Li deposition

before the bulk anode particles are fully lithiated. In Section 3.3, these phenomena were already demonstrated by controlling charge capacity with various C-rate tests and cell temperatures. In sum, just before the particle saturation, the charge capacity consists of only Li intercalation. After the surface is once saturated with lithium, the charge capacity consists of most Li deposition reaction. Therefore the critical charge capacity for the onset of Li deposition is defined as the charge capacity at which the anode particle surface becomes saturated with lithium so that no more lithium can be intercalated into the anode but plated on the anode surface. This critical charge capacity is consequently dependent on temperature and charge C-rate as shown in Fig. 3-10. A reasonable interpretation is as follows: First, as temperature is lowered, Li diffusion process becomes slower, followed by making the particle saturation faster at given charge C-rate, which induces the critical charge capacity to decrease. Second, the higher charge C-rate is, the less time for lithium to sufficiently diffuse inside particle is, which indicates the time of particle saturation is faster at given temperature. Therefore the critical charge capacity also decreases as a function of C-rate.

Experimentally, it is impossible to verify this saturation directly due to inability to measure Li concentration at the particle surface. Thus we utilized a mathematical model by collaboration with Fang [56]. The model used is an electrochemical-thermal (ECT) model developed and experimentally validated with the same Li-ion cell used in this study [42, 53]. This thesis does not deal with details about the model but just briefly introduces that the model consists of 1D electrochemical macroscopic transport model coupled with microscopic solid diffusion submodel in which Li concentration can be calculated by solving governing equation about species and charge conservation along

with radius direction of active material particle. For this calculation, anode particles close to the separator are specified because this is the starting line where electrochemical reaction occurs in the anode. Fig. 3-12 shows calculated distributions of Li concentration as a function of charge time inside an anode particle during charging at 0^{o}C with various C-rate tests. When the microscopic surface SOC reaches unity, it is indicative that the anode particle surface has become saturated by lithium, at which time a charge capacity ($I \times t$) is calculated and then compared to experimental data as shown in Fig. 3-13. It can be seen that experimental results are in good agreement, which validates the mechanism proposed above.

As shown in Fig. 3-12, we can predict distributions of Li concentration according to charge time not only at surface but also inside of particle. Low C-rate charge tests like 1C and 2C charge allow Li diffusion inside particle during charging even at 0^{o}C, which can alleviate the Li saturation on the surface. But as charge C-rate is elevated, the time of particle surface saturation is shortened much fast, which indicates insufficient time for Li occupied beneath particle surface to diffuse inside the particle sufficiently. Fundamentally it is concluded that the Li deposition phenomenon should be controlled by means of Li diffusion rate at given charging conditions. This is examined methodologically in Section 4.2.

3.5. Summary

In part one, the threshold value of Li deposition was studied. We suggest capacity comparison before and after a specific charging process to provide evidence of Li

deposition, instead of dismantling Li deposition-suspected cell and viewing its anode surface directly. Using 3-electrode cell system, the anode potential was preliminarily monitored. However, the value of anode potential cannot represent all cases of Li deposition under severe charging conditions. Instead, charge capacity was controlled at various charging conditions in order to get general parameters. This experimental method enables us to analyze the capacity loss due to Li deposition qualitatively and quantitatively. The critical charge capacity for the onset of Li deposition was experimentally obtained by contour plot from a number of charge test data.

In part two, we proposed the particle surface saturation as the mechanism for Li deposition. Even though the two parameters of C-rate (i.e. current) and temperature seem to have no relation each other, both can induce temporarily particle surface saturation under severe charging condition such as low temperature, high C-rate and both together. If the anode particle surface becomes saturated with lithium and the Li diffusion inside the anode particle is not fast enough, extra Li^+ ions inevitably lead to Li deposition on the anode surface. In order to validate this mechanism, the ECT model was utilized to predict the distributions of Li concentration inside the anode particle during charging due to experimental inability to measure it. The result shows good agreement between experimental and modeling data and also verifies the concept of anode particle surface saturation as the mechanism of Li deposition.

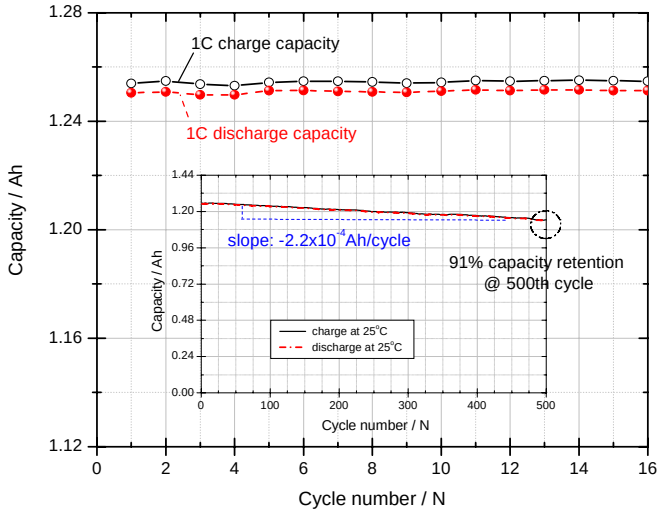

Figure 3-1: Cycle performance of 1C charge/discharge cycling at 25°C

(a)

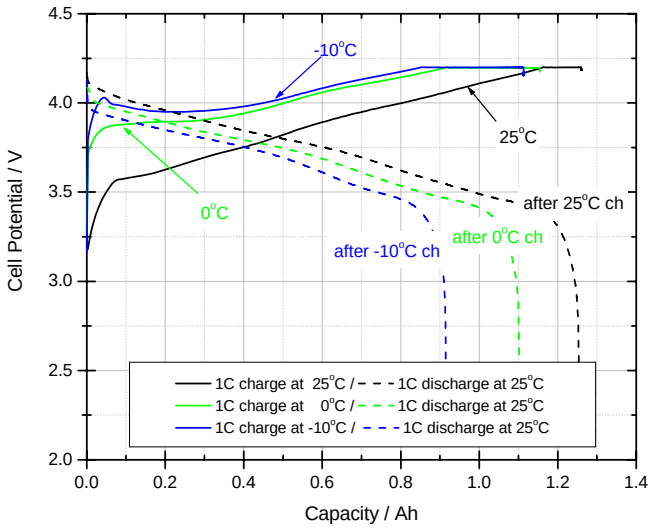
Cell Potential / V
Capacity / Ah
-10°C
25°C
0°C
after 25°C ch
after 0°C ch
after -10°C ch
1C charge at 25°C / 1C discharge at 25°C
1C charge at 0°C / 1C discharge at 25°C
1C charge at -10°C / 1C discharge at 25°C

(b)

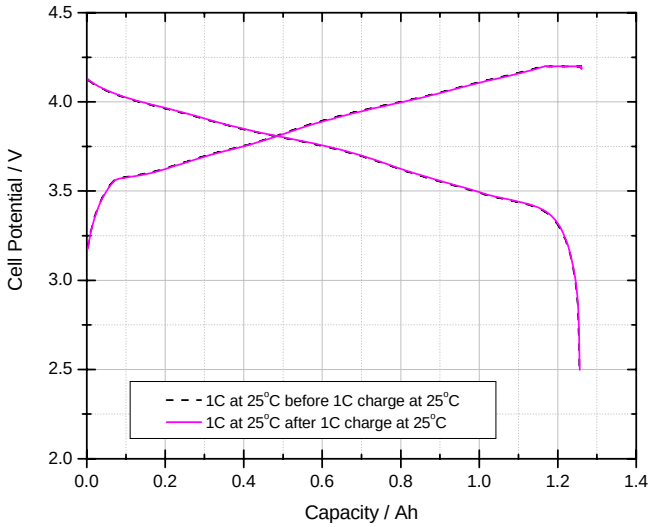
Cell Potential / V
Capacity / Ah
1C at 25°C before 1C charge at 25°C
1C at 25°C after 1C charge at 25°C

(c)

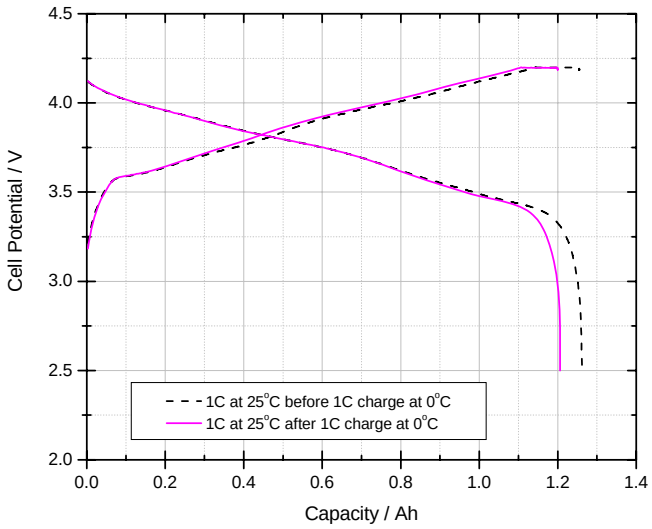

(d)

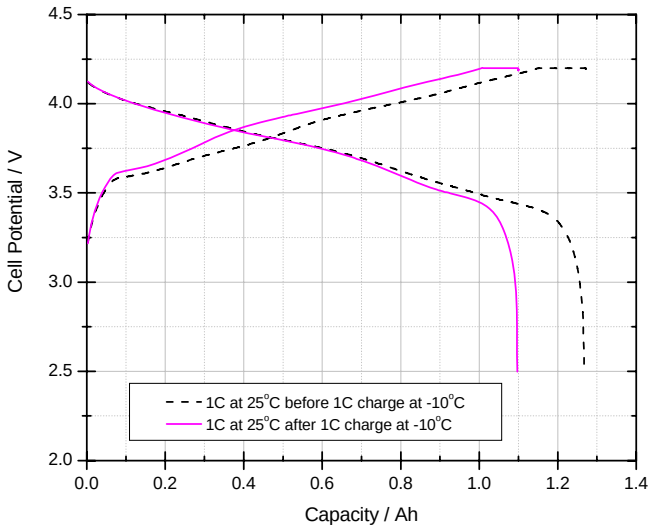

Figure 3-2: 1C CCCV charge tests at various temperatures: (a) 1C charge curves at 25°C, 0°C and -10°C and their 1C discharge curves at 25°C; and 1C capacity comparison at 25°C (b) after 25°C charge; (c) after 0°C; and (d) after -10°C

(a)

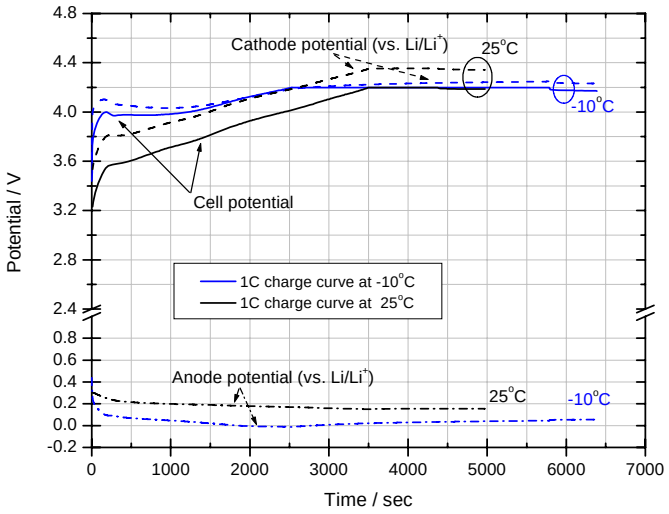

(b)

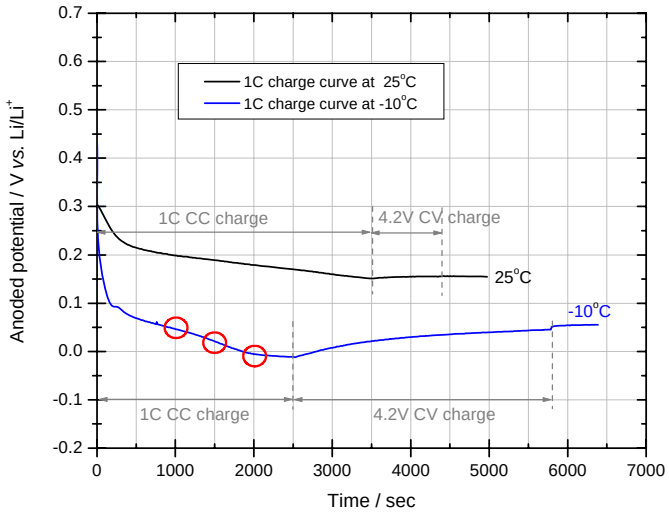

Figure 3-3: 1C charge curves with 3-electrode cell test at 25°C and -10°C: (a) full cells; and (b) anode potentials

(a)

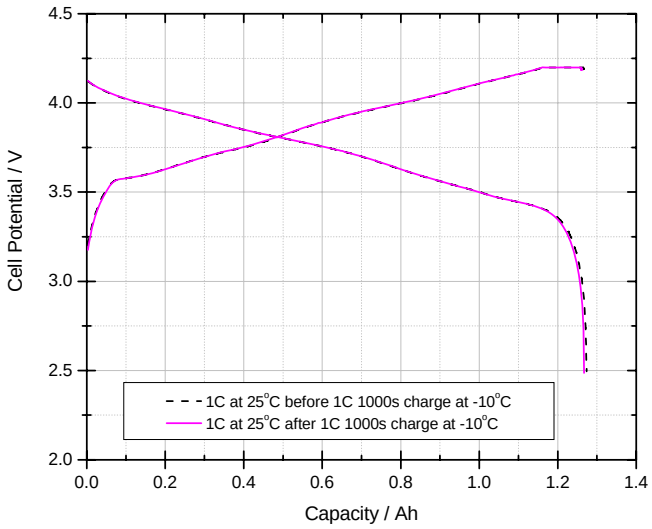
Cell Potential / V
Capacity / Ah
1C at 25°C before 1C 1000s charge at -10°C
1C at 25°C after 1C 1000s charge at -10°C

(b)

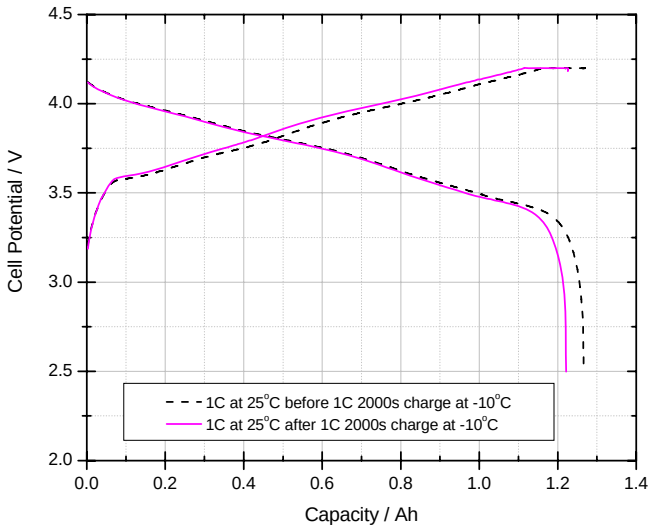
Cell Potential / V
Capacity / Ah
1C at 25°C before 1C 2000s charge at -10°C
1C at 25°C after 1C 2000s charge at -10°C

(c)

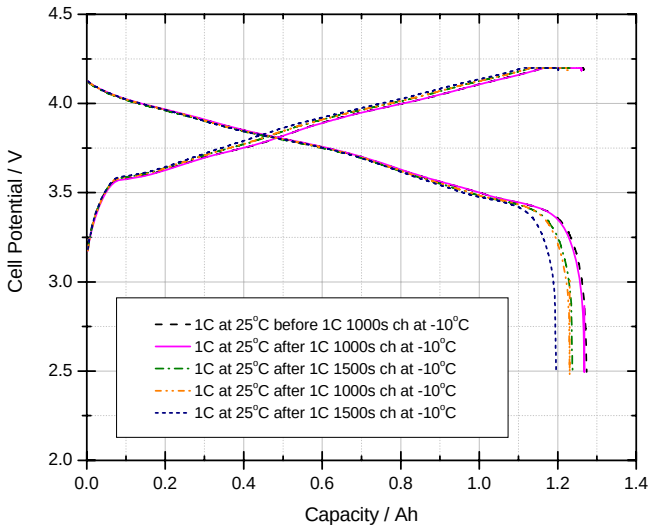

Figure 3-4: 1C capacity comparison at 25°C: (a) after 1000s charge at -10°C; (b) after 2000s charge at -10°C; and (c) after alternative 1000s and 1500s charges at -10°C

(a)

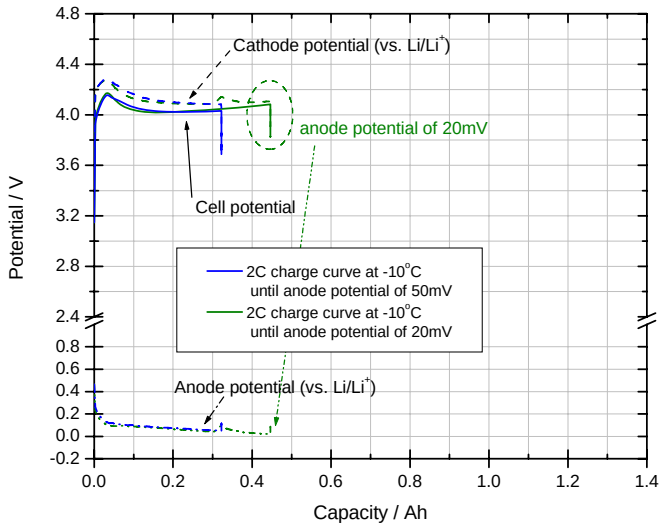

(b)

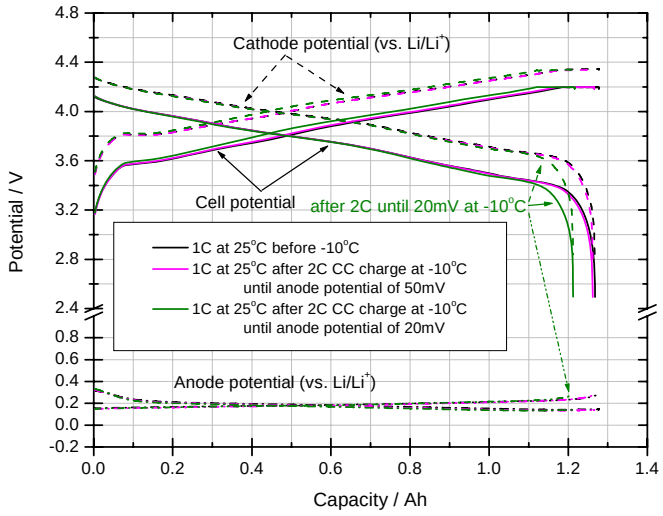

Figure 3-5: 2C charge tests at -10°C according to anode potential: (a) charge curves; and (b) 1C capacity comparison at 25°C

(a)

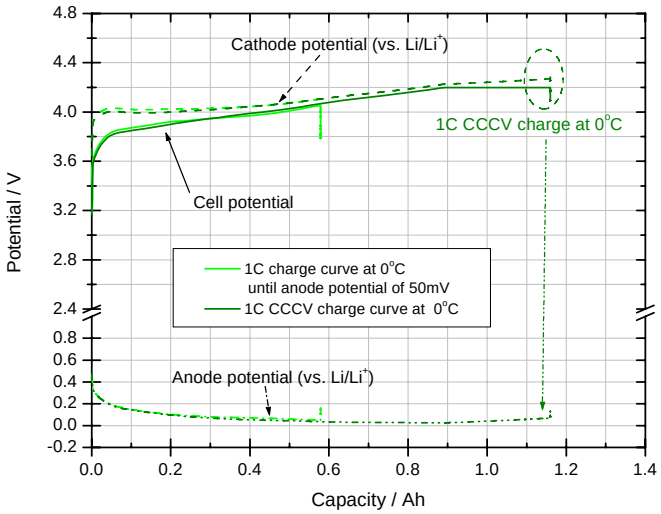

(b)

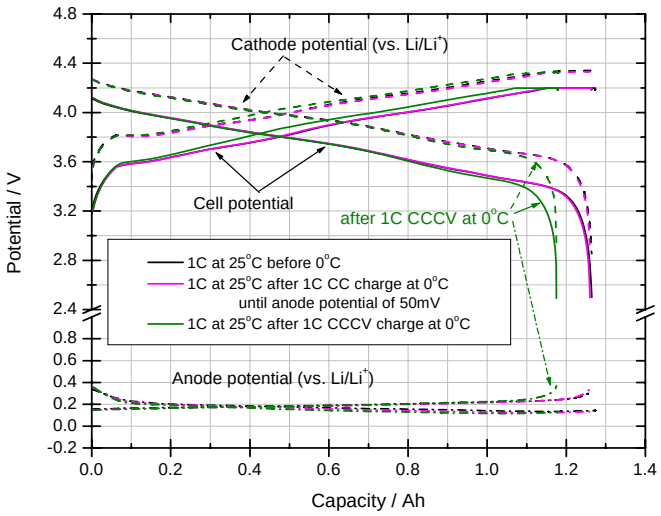

Figure 3-6: 1C charge tests at 0°C according to anode potential: (a) charge curves; and (b) 1C capacity comparison at 25°C

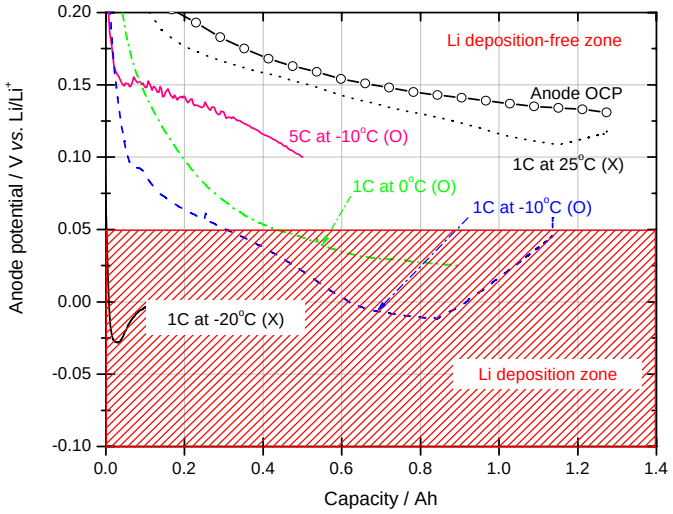

Figure 3-7: Comparison of anode potential at various charge conditions. Note that each symbol of (O) and (X) means that Li deposition happens or not respectively.

(a)

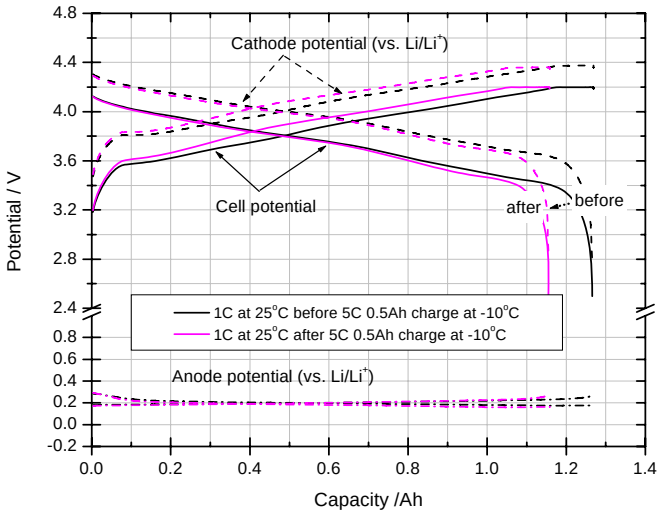

(b)

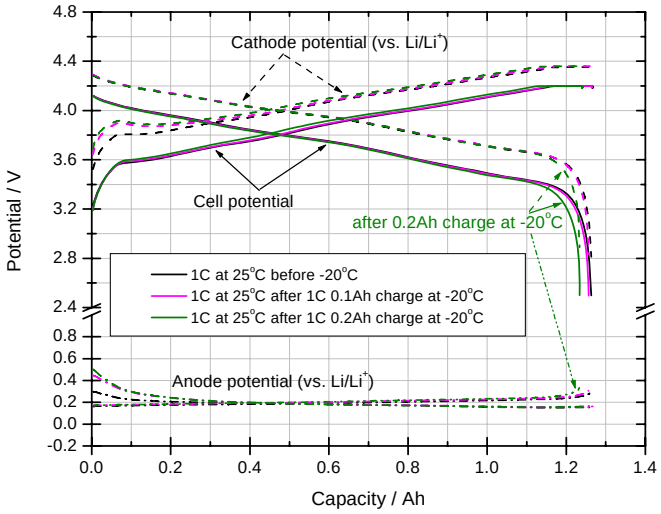

Figure 3-8: 1C capacity comparison at 20°C: (a) after 5C charge at -10°C; and (b) after 1C charge at -20°C

(a)

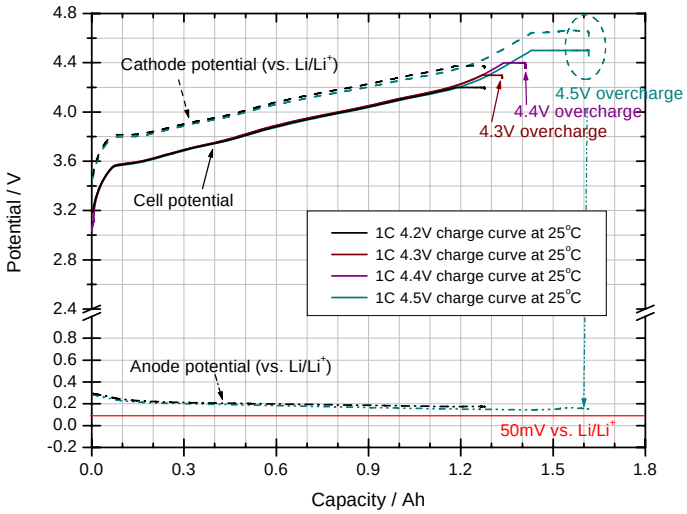
Cathode potential (vs. Li/Li+)
Cell potential
Anode potential (vs. Li/Li+)
4.5V overcharge
4.4V overcharge
4.3V overcharge
50mV vs. Li/Li+
1C 4.2V charge curve at 25°C
1C 4.3V charge curve at 25°C
1C 4.4V charge curve at 25°C
1C 4.5V charge curve at 25°C
Potential / V
Capacity / Ah

(b)

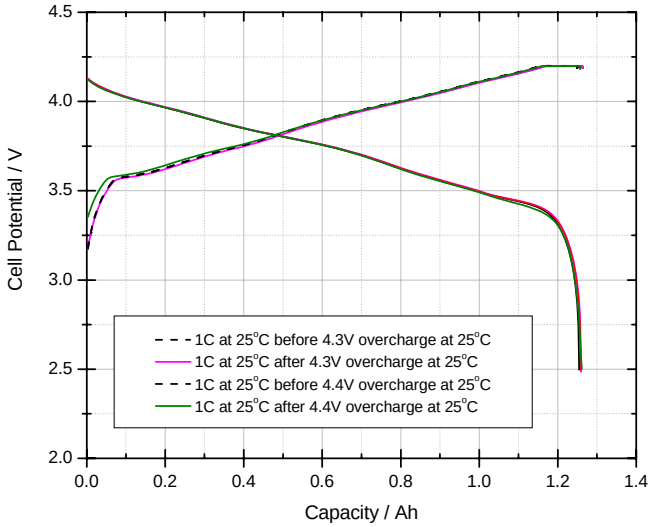
1C at 25°C before 4.3V overcharge at 25°C
1C at 25°C after 4.3V overcharge at 25°C
1C at 25°C before 4.4V overcharge at 25°C
1C at 25°C after 4.4V overcharge at 25°C
Cell Potential / V
Capacity / Ah

(c)

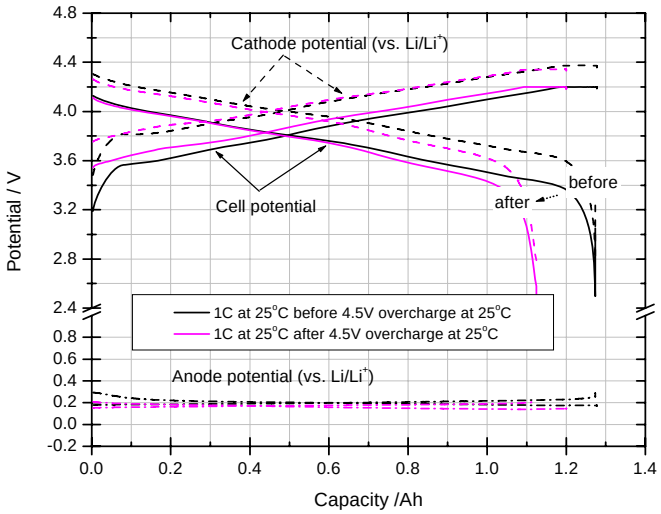

Figure 3-9: Overcharge tests at 25°C: (a) 4.3V, 4.4V and 4.5V overcharge curves at 25°C; and 1C capacity comparison at 25°C (b) after 4.3V and 4.4V; and (c) after 4.5V overcharge

Table 3-1: Capacity loss according to charge C-rate in charge capacity cut-off test at 0°C

		Charge capacity					
		0.1Ah	0.2Ah	0.3Ah	0.4Ah	0.5Ah	
Charge C-rate	1C (1.2A)	-0.6%	0.1%	0.1%	0.1%	0.1%	0.7% @ 0.58Ah
	2C (2.4A)	-0.3%	0.1%	0.2%	0.3%	0.5%	
	5C (6A)	-0.1%	0.7%	2.1%	3.7%	6.5%	
	10C (12A)	0.2%	2.2%	5.4%	7.7%	9.5%	
	15C (18A)	0.3%	3.6%	7.0%	9.0%	10.1%	
	16.7C (20A)	0.5%		5.9%	7.4%	9.6%	0% @ 0.055Ah

(a)

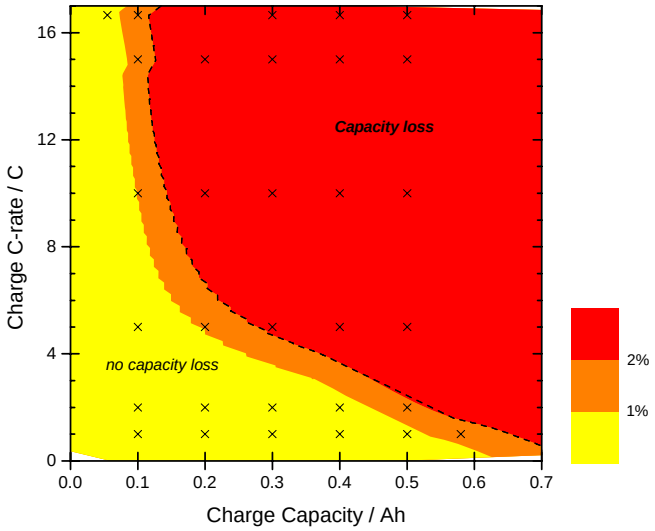
Capacity loss
no capacity loss
Charge C-rate / C
Charge Capacity / Ah
2%
1%
0
4
8
12
16
0.0
0.1
0.2
0.3
0.4
0.5
0.6
0.7

(b)

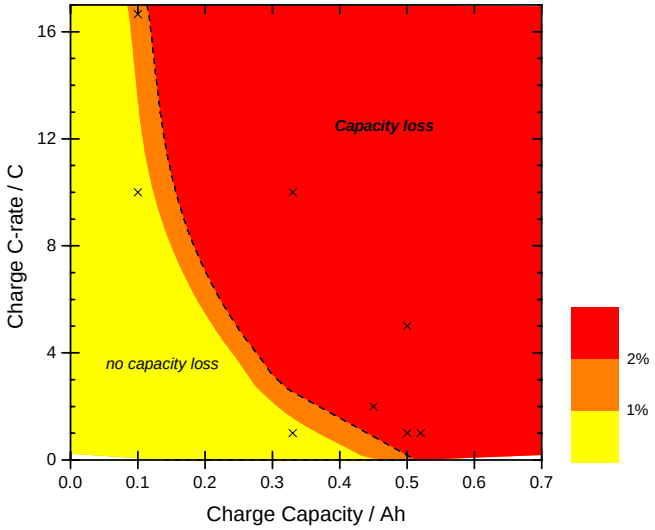
Capacity loss
no capacity loss
Charge C-rate / C
Charge Capacity / Ah
2%
1%
0
4
8
12
16
0.0
0.1
0.2
0.3
0.4
0.5
0.6
0.7

(c)

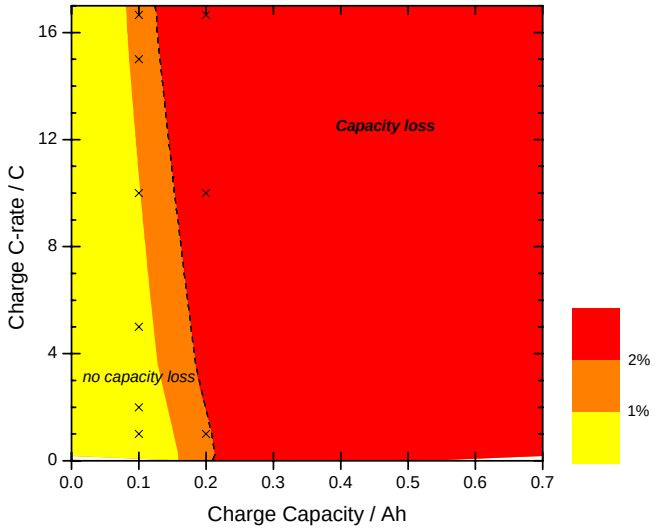

Figure 3-10: The plot of capacity loss as a function of charge C-rate and charge capacity: (a) at 0^{o}C; (b) at -10^{o}C; and (c) at -20^{o}C. Note that red area indicates that the capacity loss of more than 2 % happened.

(a)

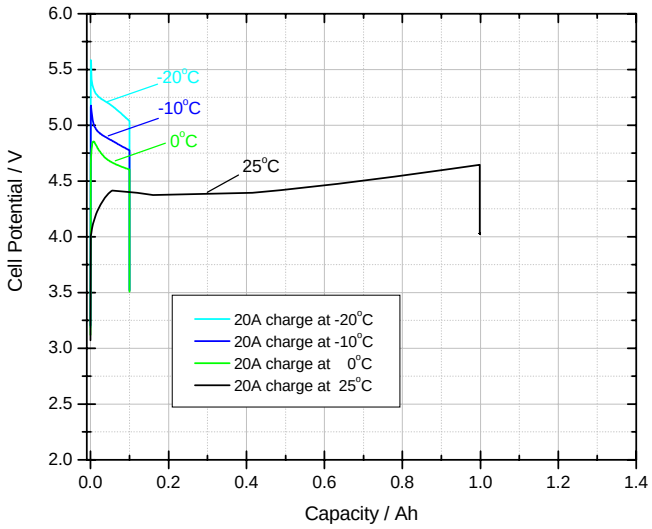
Cell Potential / V
Capacity / Ah
-20°C
-10°C
0°C
25°C
20A charge at -20°C
20A charge at -10°C
20A charge at 0°C
20A charge at 25°C

(b)

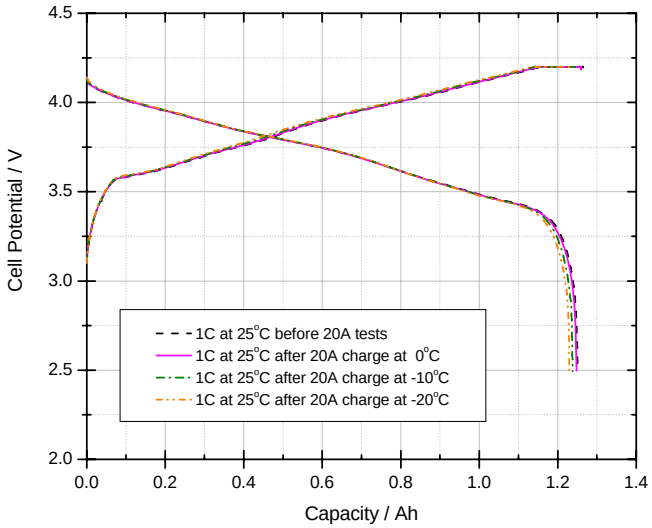
Cell Potential / V
Capacity / Ah
1C at 25°C before 20A tests
1C at 25°C after 20A charge at 0°C
1C at 25°C after 20A charge at -10°C
1C at 25°C after 20A charge at -20°C

(c)

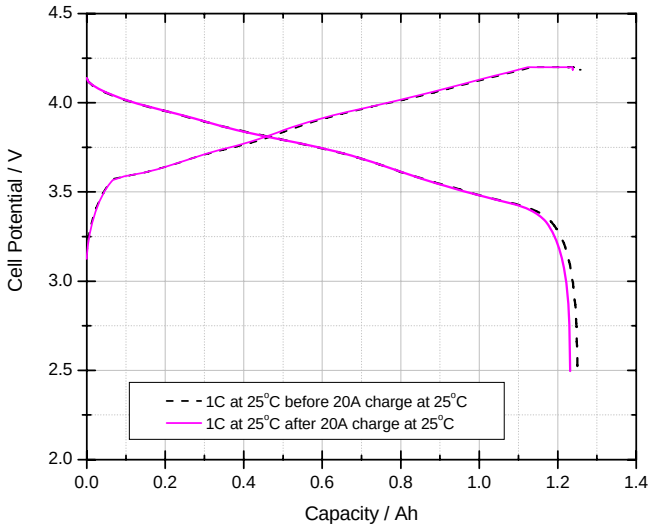

Figure 3-11: 20A charge tests at various temperatures: (a) charge curves at 25°C, 0°C, -10°C, and -20°C; and 1C capacity comparison at 25°C (b) after 20A charges at 0°C, -10°C, and -20°C; and (c) after 20A charge at 25°C

(a)

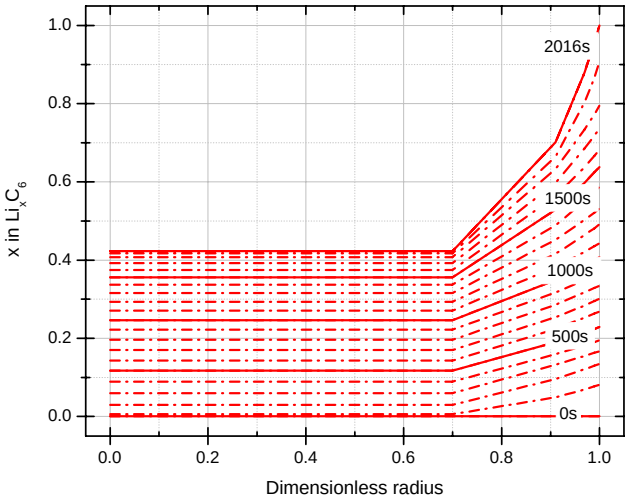
x in Li_xC_6
Dimensionless radius
2016s
1500s
1000s
500s
0s
0.0
0.2
0.4
0.6
0.8
1.0

(b)

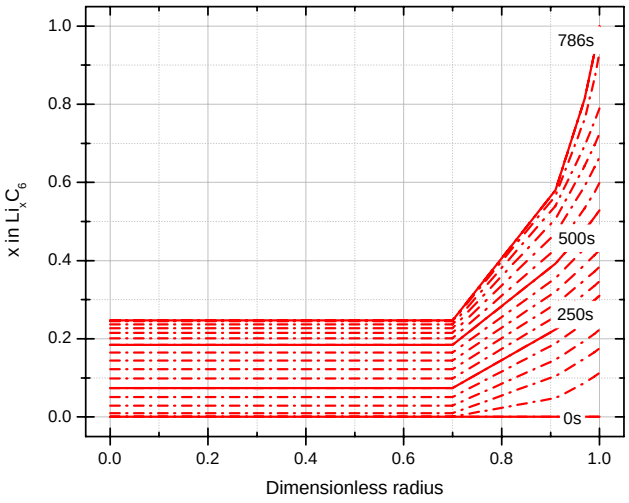
x in Li_xC_6
Dimensionless radius
786s
500s
250s
0s
0.0
0.2
0.4
0.6
0.8
1.0

(c)

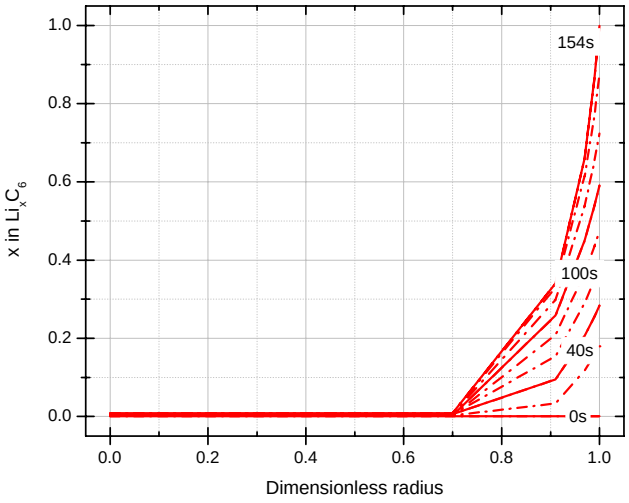

(d)

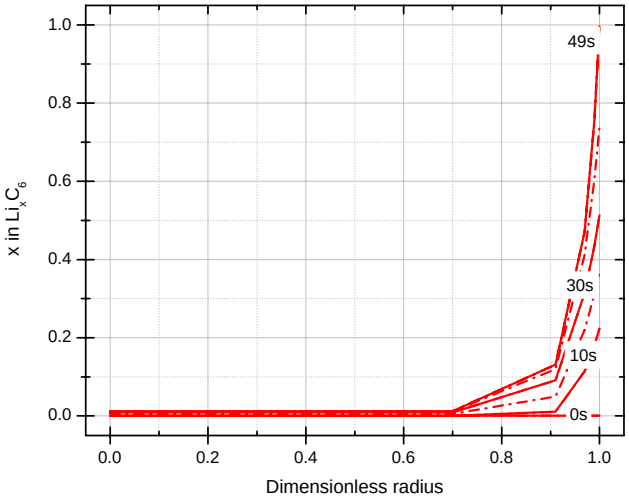

Figure 3-12: Profiles of Li concentration along the anode particle radius at 0^{o}C during charging with various C-rates: (a) 1C charge; (b) 2C charge; (c) 5C charge; and (d) 10C charge. Taken from [56]

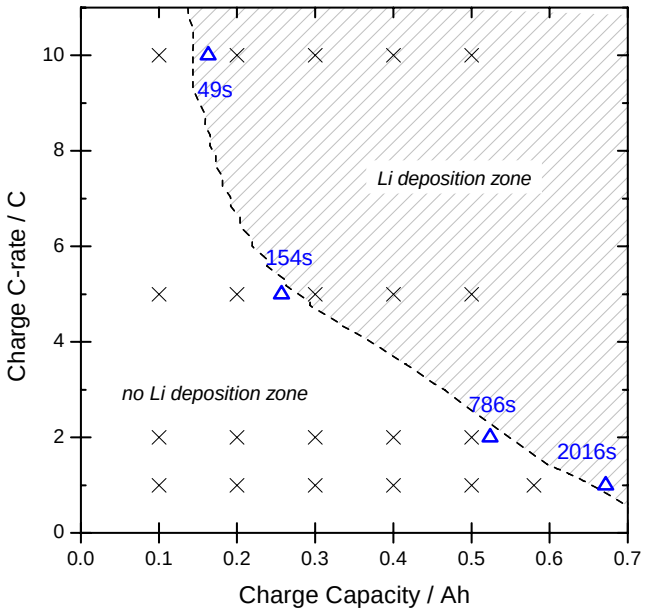

Figure 3-13**:** Comparison of critical charge capacity obtained from experiments (Fig. 3-10) and modeling (Fig. 3-12) at 0^{o}C. Note that dash line indicates the critical charge capacity obtained by experimental results. Each time when surface SOC reaches unity is marked as open triangle (Δ).

Chapter 4

Thermal Effects at Subzero Temperatures

Thermal behavior of Li-ion battery at subzero temperatures was examined in order to study how thermal effects play a role in battery performance. Based on results, a novel pulse charge protocol is proposed for the purpose of Li deposition-free, rapid charge at low temperatures.

4.1. Thermal behavior at low temperatures

As is well known, thermal management is an important engineering issue in all large-sized batteries because thermal energy is generated in batteries by electrochemical reactions of active materials, Joule heating of battery component and other irreversible processes. As performance, cycle/calendar life and abuse tolerance of Li-ion cells and packs especially depend on ambient temperature, thermal management has to play a role principally to maintain a Li-ion cell system within a specified temperature range [6]. In particular, when the rate of heat generation exceeds that of heat dissipation, the heat generated is accumulated inside the battery and then thermal runaway can occur. For automotive application, as high power operating is demanded with wide temperature range, higher risk of thermal runaway exists. This thermal runaway sometimes leads to explosion and/or fire in batteries, which must be precluded under real driving condition.

As this safety issue is a most critical factor to success Li-ion batteries in electric vehicles, most studies have been focused on thermal stability and particularly on abuse tolerance at elevated temperatures from material level to cell and pack level. The development of models for heat transfer analysis has become of increasing importance to battery design recent years [57]. Also, Li-ion battery designers incorporate one or more safety devices such as a current-interrupt, shut-down separator, vent, rupture-disk or polyswitch in Li-ion cells, which are generally designed to limit operation to temperatures below 60~65^{o}C [31, 58].

Besides upper limit of temperature, most batteries also have a minimum working temperature below which the electrolyte has low conductivity or is liable to undergo a phase change [57]. Maintenance above the minimum temperature is easy in small-sized batteries or stationary batteries from external heat source etc. Unfortunately battery-powered electric vehicles must work without any damage even at extreme low temperature. For example, in the case of the FreedomCAR goal, cold cranking tests should provide 8kW of discharge power during three 2s pulses and two 10s rests at -30^{o}C. In addition to discharge, as described in Chapter 3, the issue of Li deposition during charging at low temperature should be prevented because Li deposition causes serious permanent capacity loss. Therefore low temperature study of the Li-ion battery is required as much as high temperature study. Thermal management was studied first to determine how thermal behavior at low temperatures affects Li-ion cell performance.

4.1.1. Energy balance

Prior to investigating thermal behavior, energy balance by electrochemical reaction was studied. In general, the heating rate of entire Li-ion cell ($\dot{Q}_{\text{Total}}$) is expressed simply as follow:

$$\dot{Q}_{\text{Total}} = C_{cell}\frac{dT_{cell}}{dt} = \dot{Q}_{\text{Gen}} - \dot{Q}_{\text{Diss}}$$

where C_{cell} is heat capacity of cell, t is time and T_{cell} is temperature of cell. And $\dot{Q}_{\text{Gen}}$ is the rate of heat generation from battery inside and $\dot{Q}_{\text{Diss}}$ is the rate of heat dissipation to surrounding environment. The relation of two terms leads to temperature rise or fall.

As is well known, $\dot{Q}_{\text{Gen}}$ of electrochemical reaction consists of $\dot{Q}_{\text{S}}$ and $\dot{Q}_{\text{P}}$, that are is reversible heat due to entropy change and polarization heat due to overpotential, respectively. In general, thermodynamic Gibbs free energy equation yields the following relation:

$$\Delta G = \Delta H - T\Delta S \qquad \text{under constant pressure}$$

where the residual energy at energy conversion between the enthalpy change ΔH of the cell reaction and the electrical work ΔG can be compensated by the heat energy of $T\Delta S$ [38]. By thermodynamic definition, $dG = -SdT + Vdp$, it is seen that

$$\left(\frac{\partial \Delta G}{\partial T}\right)_p = -\Delta S \quad \text{or} \quad \left(\frac{\partial E}{\partial T}\right)_p = \frac{\Delta S}{nF}$$

because ΔG is equal to $-nFE$ where n is charge number participating reaction ($n=1$ for overall reaction of Li-ion cell), F is Faraday constant and E is cell potential. Therefore, the $\dot{Q}_S$ by entropy change is described by the following:

$$\dot{Q}_S = T\Delta S\frac{I}{nF} = I\cdot T\left(\frac{\partial E}{\partial T}\right)$$

where I is charge/discharge current. It is defined as positive during charge here. In Chapter 2, $\partial E/\partial T$ term is already measured. As this value is negative, $-0.2\,\mathrm{mVK^{-1}}$, the overall reversible heat is endothermic during charge and exothermic during discharge.

The next heat source comes from polarization heat due to overpotential. In kinetics of all electrochemical reactions, current flow indicates that electrochemical reaction progresses, which derives potential deviation from open circuit potential, i.e. polarization. It induces irreversible energy loss as heat. It yields as follow:

$$\dot{Q}_P = I\Delta E = I\cdot\eta = I\cdot IR = I^2R \qquad \text{under constant current}$$

where η is the overpotential and R is the polarization resistance, also known as total internal resistance. This value is always positive, which means this heat is exothermic regardless of charge and discharge process. This overpotential results from two main causes [57]:

(1) ‘ohmic’ loss in the bulk of the electrolyte phases, separators and sometimes in the electrode and connector.

(2) ‘electrode’ loss which include the ‘activation overpotential’, connected with the charge transfer step and/or nucleation and crystallization processes at each electrode/electrolyte interface, and the ‘concentration overpotential’ related to the depletion or accumulation of electroactive material near the electrode surface.

The internal resistances resulting from these overpotentials were measured by EIS as a function of temperature as shown in Fig 4-1(a). This Nyquist plot shows that its abscissa is a real resistance component and its ordinate is an imaginary component. In general, under alternating current with high frequency, total resistance is electronic and ionic resistances because capacitance component inside electrode is open and thus charge transfer resistance should be bypassed. At mid frequency range, charge transfer resistance is expressed with semicircle form. Here R_1 is the value of intercept at abscissa and R_2 is the value of semicircle diameter. As temperature is lowered, R_2 value increases extremely while R_1 remains almost unchanged. As shown in Fig. 4-1(b), the relation shows exponential rise of charge transfer resistance along with inverse temperature ($1/T$) as follows [59]:

$$R_2 = 1.93 \times 10^{-14} e^{8214/T} \Omega \text{ , while } R_1 \approx 0.03\Omega$$

Therefore we get the mathematical equation of heat generation as a function of temperature as below:

$$\dot{Q}_{\text{Gen}} = C\frac{dT}{dt} = I^2 R + IT\left(\frac{\partial E}{\partial T}\right) = \left(1.93 \times 10^{-14} e^{8214/T} + 0.03\right) \cdot I^2 - 0.2 \times 10^{-3} T \cdot I$$

As shown in Fig. 4-2, the irreversible heat (overpotential heat) portion of total heat generation was calculated by the above equation. In the case of low rate and room temperature operation (circle in Fig. 4-2), the entropy heat term cannot be neglected. However, in high rate and low temperature (box in Fig 4-2), the main heat source can be regarded as the overpotential heat. Therefore in automotive application, it can be concluded that this overpotential heat term is of more importance. Figure 4.2 also shows

the comparison of measured and calculated values of 1C case along with temperature. From GITT test in Fig. 2-5(a), overpotentials were measured during 1C discharge process at each test temperature, followed by calculating the value of $I \cdot \eta$. The irreversible heat portion obtained by GITT data (DC measurement) shows good agreement with that calculated with internal resistance equation ($1.93 \times 10^{-14} e^{8214/T} + 0.03$) from EIS test (AC measurement). Although DC measurement is closer to real circumstance, the result represents just total sum of polarization. But as shown in Fig. 4-1, the EIS data can separate each resistance component to obtain total internal resistance in detail.

Finally, the rate of heat dissipation is expressed below:

$$\dot{Q}_{\text{Diss}} = Ah(T - T_{amb})$$

where A is the surface area of cell and h is the heat transfer coefficient. T_{amb} indicates surrounding temperature. As all terms in the energy balance equation were obtained, thermal behavior can be estimated. But according to battery size, the temperature gradient inside the battery exists. Forgez *et al*. [60] measured a temperature difference between surface and internal temperature of 26650 cylindrical cell by drilling a hole in the center of the bottom and inserting an insulated thermocouple. There was a difference up to 10°C observed depending on C-rate. Thus in this study, two steps of heat transfer were assumed; The heat generated inside cell is propagated to the surface of 18650 cylindrical can that is exposed to ambient temperature; the temperature of can is changed to dissipate the heat propagated to surrounding, which yields the following two equations:

$$C_{\text{cell}} \frac{dT_{\text{cell}}}{dt} = I^2 R + I \cdot T\left(\frac{\partial E}{\partial T}\right) - Ah_{\text{cell}}\left(T_{\text{cell}} - T_{\text{can}}\right)$$

$$C_{\text{can}}\frac{dT_{\text{can}}}{dt} = Ah_{\text{cell}}\left(T_{\text{cell}} - T_{\text{can}}\right) - Ah_{\text{can}}\left(T_{\text{can}} - T_{\text{amb}}\right)$$

where T_{cell} is internal temperature of cell assuming there is no more temperature gradient along with position inside cell, T_{can} is the surface temperature of cell and T_{amb} is the temperature of environmental chamber.

To validate these equations, 10C charge for 30s at 0^{o}C was conducted, which is equivalent to 0.1Ah. Note that this is a safe value against Li deposition at given low temperatures in Chapter 3. As shown in Fig. 4-3, the temperature rise of 5^{o}C within 1min was observed during charge and rest. Maximum temperature was observed at 30s later after stopping current. It can be explained that the heat accumulated inside Li-ion cell for 30s charge is still released after stopping current. When releasing heat from inside cell is equal to dissipation outside cell, temperature rise is ended and temperature decrease starts. After plugging in physical parameter, both internal and surface temperatures were calculated under the same charge condition. This calculated surface temperatures result shows a good match with experimental result. Internal and surface temperatures calculated here show the difference of 9^{o}C at maximum value, which means that the calculated cell temperature shows much faster increase than surface temperature due to high rate of heat generation compared to heat dissipation. In sum, it is concluded that energy balance proposed here can reliably estimate and simulate thermal behavior of Li-ion cells.

4.1.2. Measurement of thermal behavior

The charge curve in Fig. 4-3 shows a hump at the initial charge point, which consists of rapid potential increase and next, continuous decrease. Although it is generally shown that cell potential profile rises as a function of SOC because full cell OCP also increases, as shown in Fig. 2-6, these phenomena are observed in various cases for low temperature and/or high rate operation. In Fig. 4-4(a), cell potential curves show this overshooting behavior at 1C charge as temperature is lowered. Charge and discharge curves also show this behavior at high C-rates, as shown in Fig. 4-4(b) and Fig. 4-4(c). This overshooting/undershooting indicates that overpotential decrease unusually along with SOC in aspect of electrochemical reaction. The above test conditions belong to overpotential heat dominant area, i.e. only the exothermic reaction region in Fig. 4-2, which means that initial overpotential is large. Thus cell temperature due to overpotential heat increases rapidly, followed by quickly decreasing internal resistance ($R \propto e^{1/T}$). As a result, overpotential is lowered, which induces cell potential decrease as charge process continues and the hump of potential profile is shown. This is an example of electrochemical-thermal interactions at low temperatures. This strong interaction can be utilized for novel pulse charge in Section 4.2.

Figure 4-5 shows this phenomenon in detail. 20A constant-current charge for 18 seconds (0.1Ah) was conducted. As temperature is lowered, the increasing rate of temperature becomes steep. Because Li-ion cell at lower temperature has higher internal resistance, the rate of irreversible heat generation (I^2R) subsequently rises at the same current. The difference between maximum temperature and initial temperature is also

dependent on heat generated. As temperature is lowered, the amount of temperature rise also increases. As a result, the degree of overpotential decrease at each temperature increases, which is shown as potential difference (ΔV) between maximum cell potential and charge-end potential: 0.25V at 0°C; 0.40V at -10°C and 0.54V at -20°C. This is indicative that overshooting phenomena are more distinct as temperature is lowered.

Different C-rates were applied at 0°C with same amount of charge capacity (0.1Ah) as shown in Fig. 4-6. In both cases, the main heat generated comes from I^2R as shown in Fig. 4-2. 10C charge for 0.5min shows temperature rise of 5°C; but 1C charge for 5min does not because the heat generated in 1C charge is much less by 100 times than 10C charge. In similar, Fig. 4-7 shows the result of alternative C-rate charge test at 0°C without rest. At 16.7C (20A) charge for 18s, cell temperature increases rapidly; but at 1C (1.2A) charge for 5min, temperature decreases in contrast. It is believed that heat dissipation is larger than heat generation in case of 1C charge at 0°C compared to high rate charge. In order to increase cell temperature from subzero temperature, high current should be applied.

4.2. Novel pulse charge

As electrochemical reactions closely relate to thermal behavior, a novel charge protocol at low temperature is introduced using self-heating of Li-ion cell. In order to increase cell temperature, high current is required, which however has high risk of Li deposition at low temperatures. For instance, it is impossible to increase temperature up to room temperature from subzero temperatures when considering critical charge capacity

(~0.1Ah at 20C charge) as shown in Fig. 4-5. Thus consecutive discharge pulse was employed in order to release Li concentration from saturated anode surface. As shown in Fig. 4-8, 20A charge/discharge pulses were applied for each 9s, which is equivalent to 0.05Ah of charge/discharge capacity. There was consecutive interval of 1s rest between pulses for total 5min of test time. It should be noted that 20A is the maximum allowable current from the battery manufacturer and 0.05Ah is Li deposition-free charge capacity as shown in Fig. 3-10. This test was conducted from SOC 0% level. As net charge capacity is zero, OCPs between initial and end point are same.

In Fig 4-8, room temperature was reached within a few minutes. As initial high current charge/discharge pulse makes cell temperature increase rapidly, internal resistance subsequently decreases, which feeds back the heat generated (I^2R). Therefore while the test time elapses, the increasing rate of temperature is lowered continuously. The potential deviation between charge and discharge curves also decreases. Thus overall thermal behavior shows parabolic curve shape. After 3min, potential change resulting from overpotential shows the same profile, which indicates that at that time internal resistance is too small that no more rapid temperature rise occurs.

Figure 4-9 shows the same pulse tests at different temperatures. All thermal behaviors show similar profiles. After just 1.5min, every temperature exceeds 30^{o}C, where charge profiles cannot be distinguished, as shown in a small box of Fig. 4-9(a). Every test shows no capacity loss, as shown in Fig. 4-9(b), because charge pulse duration was controlled under less than critical charge capacity and discharge pulse is also effective for eliminating Li saturation on surface. Therefore this high current

charge/discharge pulse test can increases temperature within a short time without concern of Li deposition at subzero temperatures. As already explained in Chapter 2, charge transfer resistance and Li diffusion coefficient depend strongly on temperature. Once cell temperature rises up to room temperature, no concern is necessary for sluggish kinetics. Thus it is important to maintain temperature above room temperature in order to enhance kinetics of electrochemical reaction. Additionally, as this method offers self-heating of automotive Li-ion cell, no external heat source is demanded.

Figure 4-10 and 4-11 summarize a novel pulse charge protocol in detail. First, total charge time and ambient temperature were fixed to 6min and 0^{o}C. Test (i) consists of high current pulses (the same as the pulse test of Fig. 4-8) for 3min and then high current charge (20A) for the last 3min. Test (ii) is 10A CC charge for a total of 6min. Each net charge capacity is 1.0Ah, that is, 80% of rated capacity. As shown in Fig 4-11(a), there was no capacity loss after Test (i), but huge capacity loss was observed after Test (ii) as shown in Fig. 4-11(b). Even though Test (ii) employs lower charge current than Test (i), the degree of capacity loss increases, unlike the general trend listed in Table 3-1, which can be explained because cell temperature difference of two tests is a key factor. When the 20A charge of Test (i) starts after pulses for 3min, the temperature is around 30^{o}C while overall temperature of Test (ii) does not exceed 20^{o}C. In addition, from Fig. 3-10, it can be estimated that Li deposition of Test (ii) already starts around 1min later, at which time temperature is around 5^{o}C. On the other hand, the 20A charge at 25^{o}C is allowed to charge up to 1.0Ah of charge capacity without capacity loss, as shown in Fig. 3-11(c). Test (iii) is followed by a process similar to Test (i). The only difference is that pulse duration of charge/discharge is 27s, which corresponds to 0.15Ah.

Thus although Test (i) and (iii) show the same temperature profile, a small capacity loss was observed in Fig. 4-11(c). This result points out the importance of critical charge capacity. In sum, high current charge/discharge pulse can increase cell temperature up to predetermined temperature rapidly within a few minutes, and the following high current charge above room temperature can be conducted without Li deposition. During high current charge/discharge pulses, pulse duration must have limitation of less than critical charge capacity inducing Li deposition, as obtained by Fig. 3-10. This protocol is called the novel pulse charge.

Figure 4-12 compares this novel pulse charge and 1C charge with the same amount of charge capacity (1.0Ah) at 0^{o}C. After both charges and rest for 10minutes at 0^{o}C, the chamber temperature was elevated to 25^{o}C for 2 hours in order to reach thermal equilibrium and then 1C discharge capacities were compared. As shown in Fig. 4-12, the novel pulse charge takes a total of 5min and no capacity loss was observed. But 1C charge takes longer (50min) and 10% of capacity loss happens as expected. In Fig. 4-13, cycle tests were conducted by these two charge methods. 1C charge for 50min induces serious capacity fade while novel pulse charge method shortens charge time and maintains good cycle performance. It is concluded that this novel pulse charge protocol can offer the solution for two problems of Li deposition at low temperatures and rapid charge simultaneously.

4.3. Summary

In order to find Li deposition-free charge method, thermal behavior was studied because electrochemical-thermal interaction plays a role in battery kinetics. First the energy balance of our 18650 Li-ion cell as a function of current and temperature was yielded by EIS and GITT test. From EIS test, internal resistance as a function of temperature was measured, which shows exponential increase with inverse temperature and determines irreversible heat (I^2R) at given current. Another heat source, reversible heat, comes from entropy change ($\sim \partial E/\partial T$) that was measured through GITT test in Chapter 2. At low temperature and/or high rate condition, irreversible heat is dominant, which can explain the phenomenon having a potential hump on initial charge/discharge and rapid temperature rise from subzero temperatures.

The novel pulse charge protocol was proposed here for the first time. This method consists of two-step charge. The first step is to increase temperature up to predetermined value within a short time by applying high current charge/discharge pulses, and the pulse duration must be limited to less than critical charge capacity. The second step is to apply high constant current with no adverse impacting on Li-ion cell such as Li deposition. This charge protocol allows automotive Li-ion batteries not only to reduce charging time but also to extend cycle life, even at subzero temperatures.

(a)

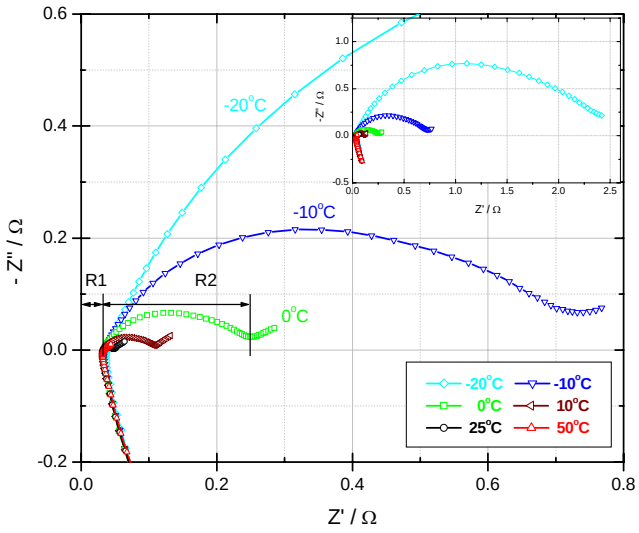

(b)

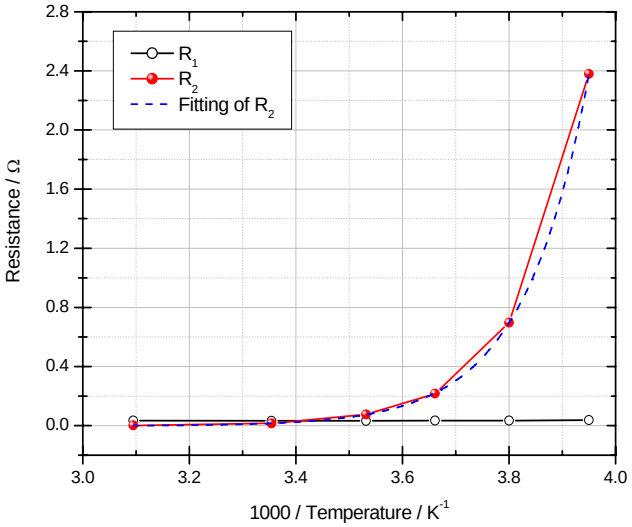

Figure 4-1: Resistance versus temperature: (a) EIS according to temperature; and (b) resistance fitting. Note that R1 is the resistance that is intercept of abscissa. R2 is the diameter of semicircle.

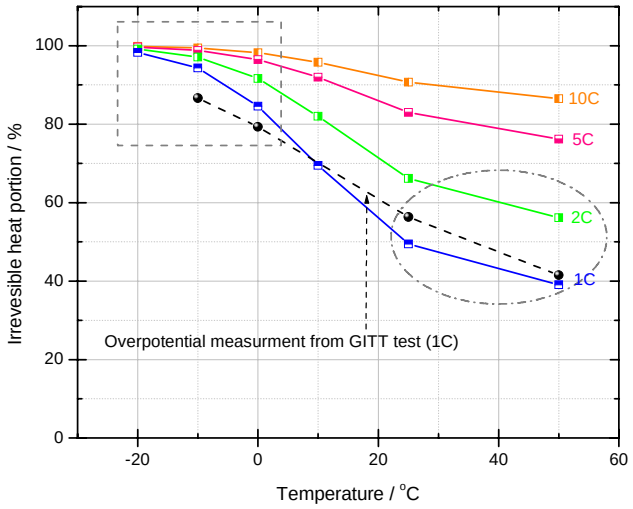

Figure 4-2: Irreversible heat portion over total heat generation as a function of temperature and C-rate. Total rate of heat generation is sum of irreversible heat rate ($\dot{Q}_P$) and reversible heat rate ($\dot{Q}_S$).

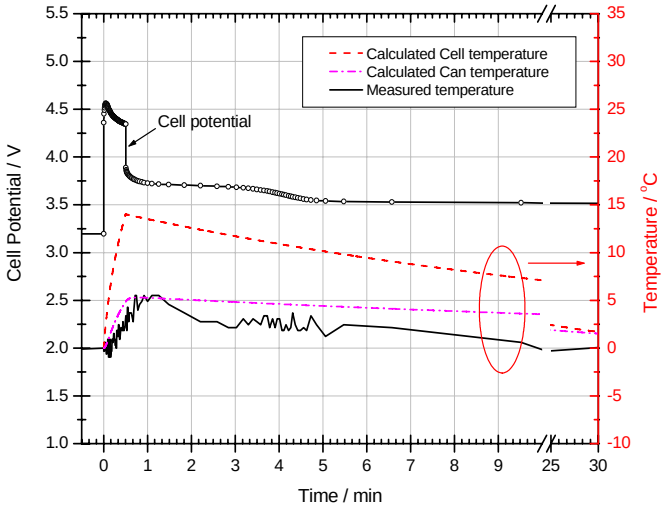

Figure 4-3: Cell potential and temperature change during 10C charge for 30s (0.1Ah) at $0^{o}C$

(a)

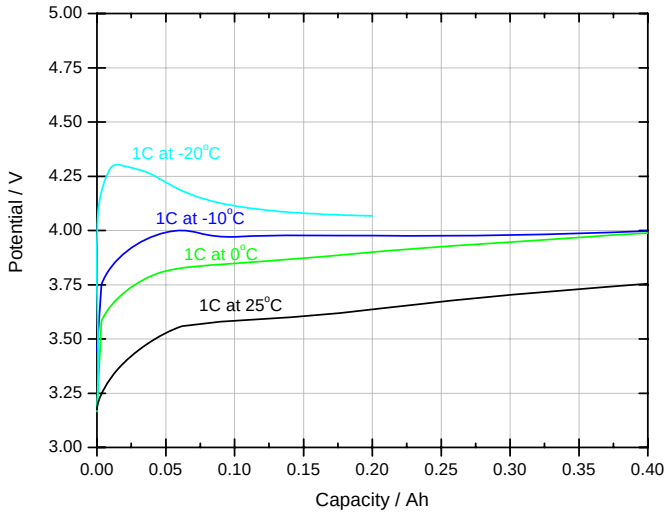
5.00
4.75
4.50
4.25
4.00
3.75
3.50
3.25
3.00
Potential / V
0.00
0.05
0.10
0.15
0.20
0.25
0.30
0.35
0.40
Capacity / Ah
1C at -20°C
1C at -10°C
1C at 0°C
1C at 25°C

(b)

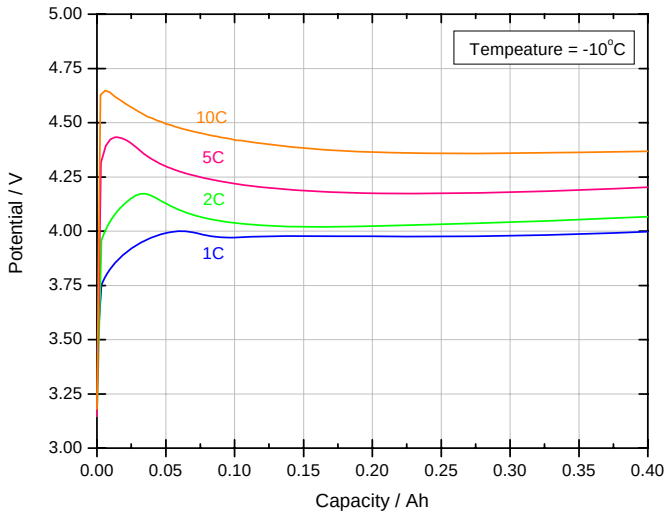
5.00
4.75
4.50
4.25
4.00
3.75
3.50
3.25
3.00
Potential / V
0.00
0.05
0.10
0.15
0.20
0.25
0.30
0.35
0.40
Capacity / Ah
Tempeature = -10°C
10C
5C
2C
1C

(c)

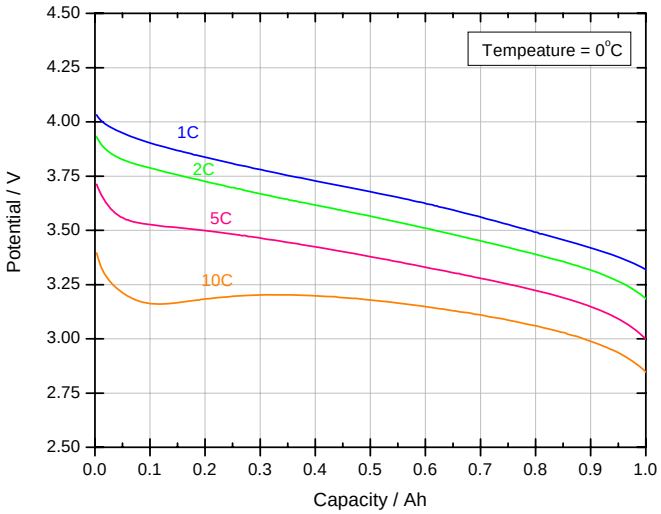

Figure 4-4: Potential profiles showing a hump according to temperature and C-rate: (a) 1C charge curves according to temperature; (b) charge curves according to C-rate at -10°C; and (c) discharge curves according to C-rate at 0°C

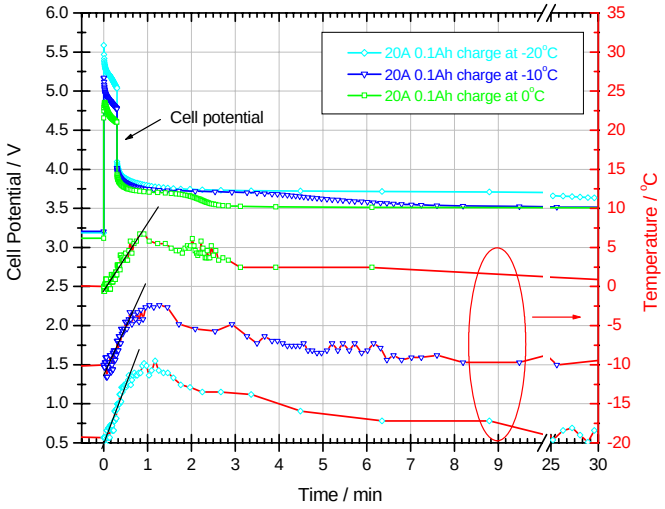

Figure 4-5: Cell potential and temperature changes during 20A charge for 18s (0.1Ah) according to temperature

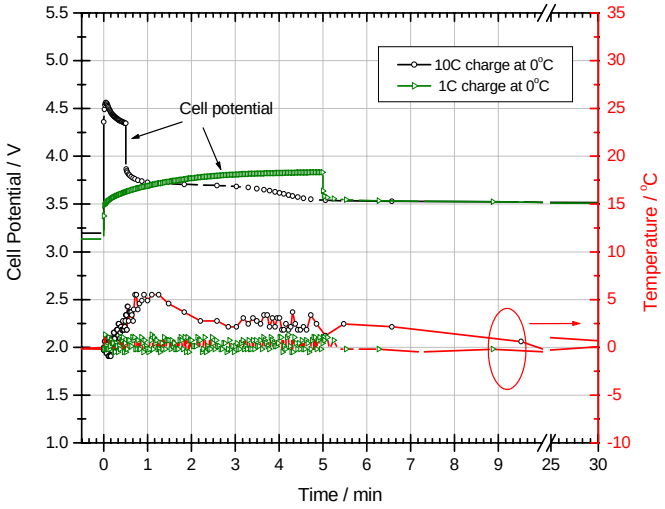

Figure 4-6: Cell potential and temperature changes according to charge C-rate with same 0.1Ah charge capacity at 0°C: 10C for 30s and 1C for 300s

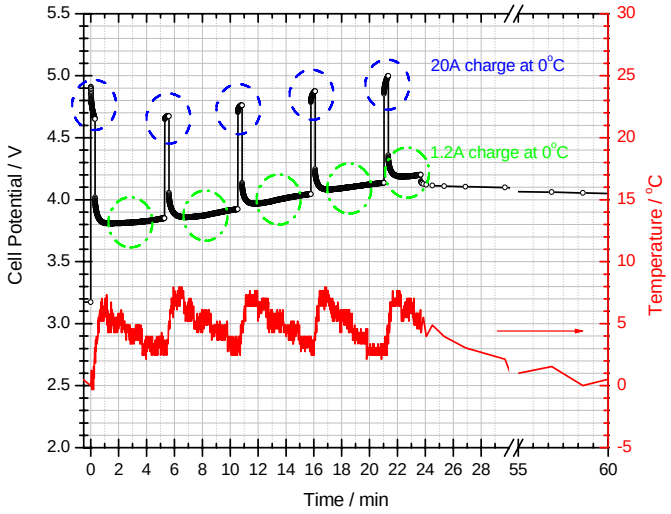

Figure 4-7: Alternative high current of 20A and low current of 1.2A charge test at 0°C

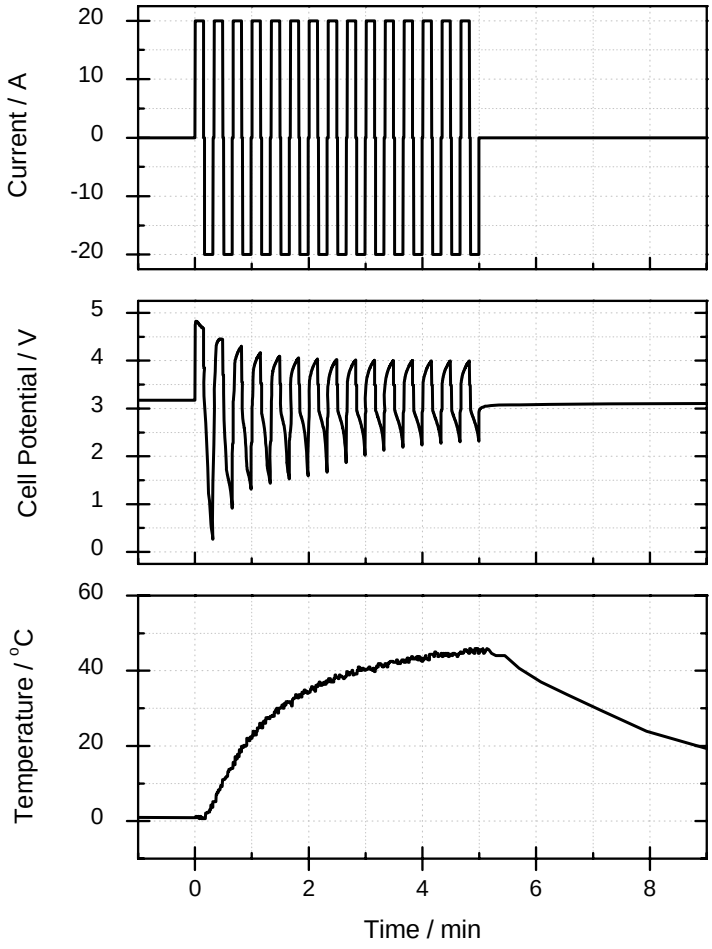

Figure 4-8: High current charge/discharge pulse test at 0°C

(a)

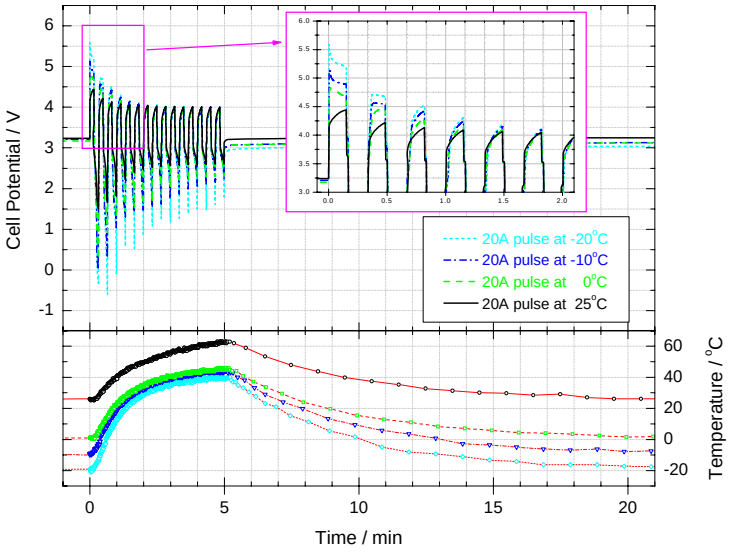

(b)

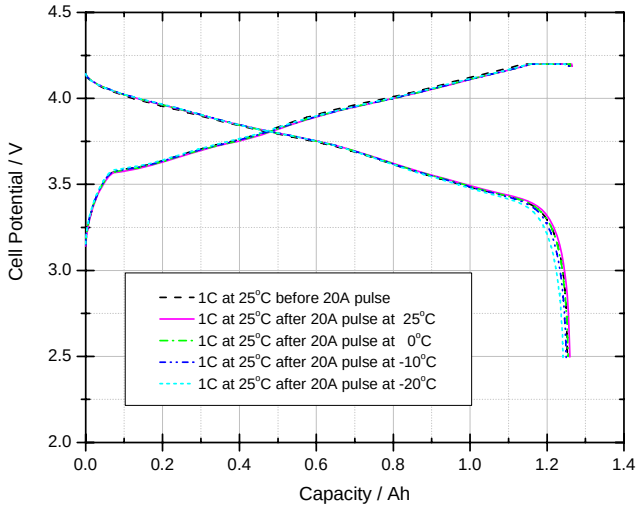

Figure 4-9: High current charge/discharge pulse test at various temperatures: (a) Cell potential and temperature changes; and (b) 1C capacity comparison at 25°C after pulse test

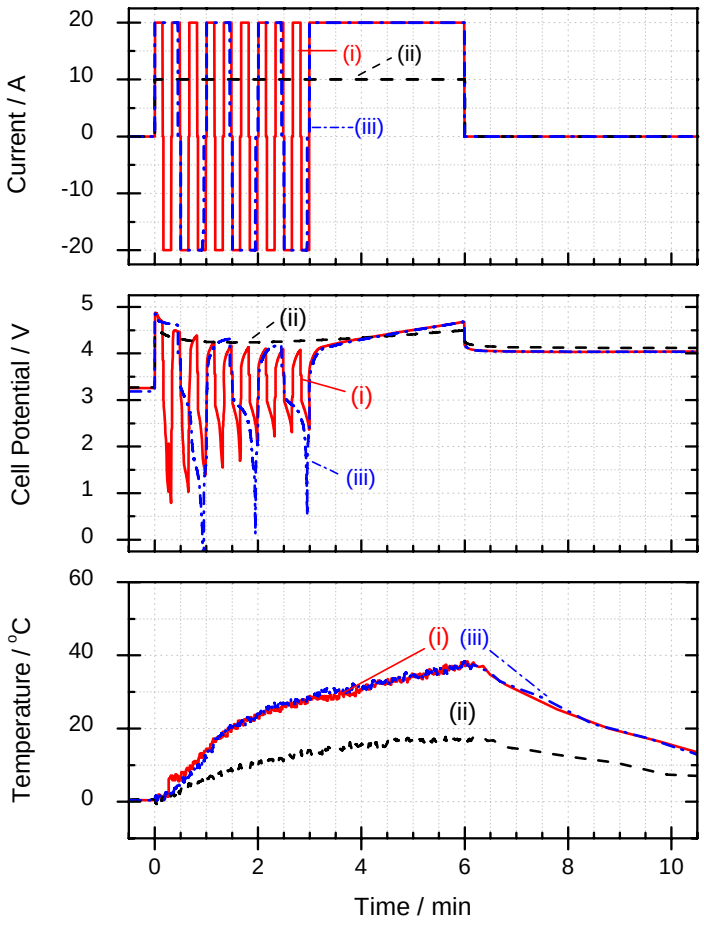

Figure 4-10: Cell potential and temperature behavior with various charging protocols at 0^{o}C. Note that Test (ii) is 1C CC charge for 6min; Test (i) and Test (iii) are two-step charge; 1^{st} step is high current pulse for 3min and 2^{nd} step is 20A charge for 3min. Test (i) has 9s of pulse duration but Test (iii) has 27s of pulse duration.

(a)

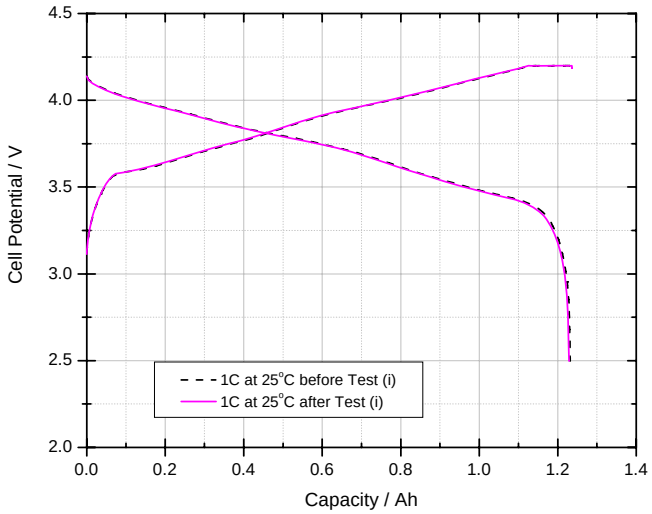
Cell Potential / V
Capacity / Ah
1C at 25°C before Test (i)
1C at 25°C after Test (i)

(b)

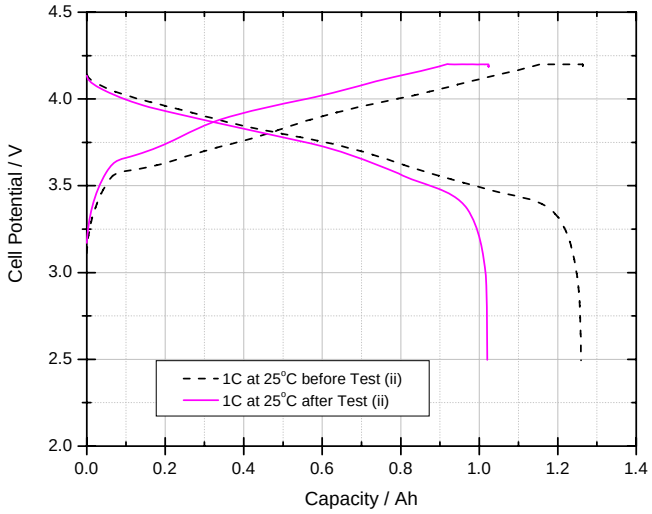
Cell Potential / V
Capacity / Ah
1C at 25°C before Test (ii)
1C at 25°C after Test (ii)

(c)

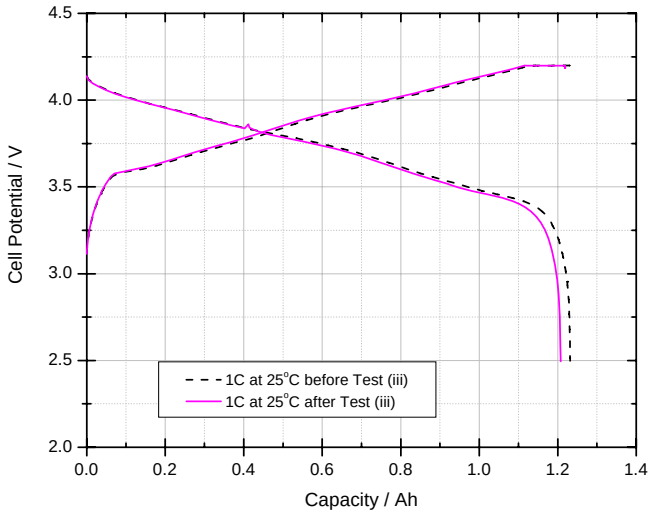

Figure 4-11: 1C capacity comparison at 25°C after various charge tests as shown in Fig. 4.10

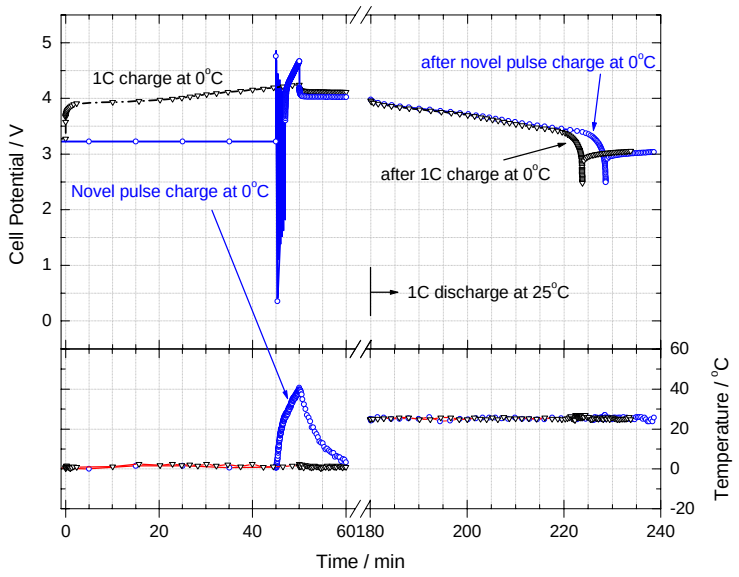

Figure 4-12: Comparison of novel pulse charge with 1C constant current charge at 0°C under equal amount of charge capacity (1.0Ah, 80% of rated capacity). After charging at 0°C and 2hr rest, both cells were discharged at 25°C.

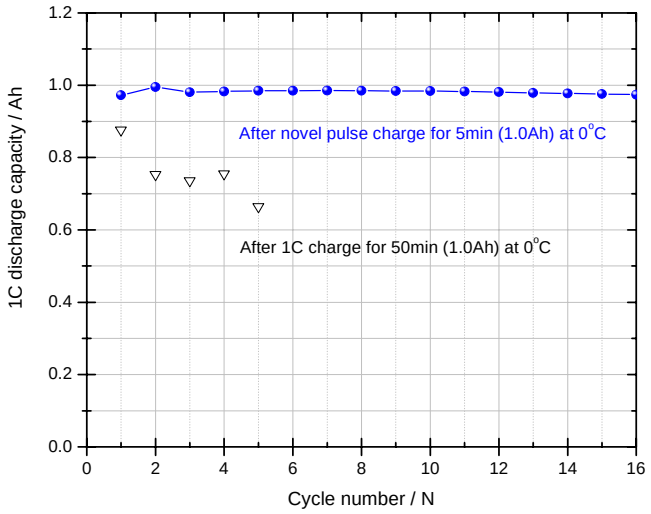

Figure 4-13: 1C discharge capacity at 25°C after two different charge protocols at 0°C

Chapter 5

Conclusions and Future Work

5.1. Conclusions

This dissertation introduces Li deposition-related (1) cause and effect; (2) diagnostic method; and (3) preventive charging protocol. Using automotive 18650 cylindrical Li-ion cells (1.2Ah) throughout the present work, we:

1. measured thermodynamic and kinetic parameters of each cathode and anode as a function of SOC and temperature, which is provided to understand electrochemical reaction and relevant thermal behavior of the Li-ion cell.
2. experimentally found the threshold parameter of Li deposition, namely the critical charge capacity, that not only depends on temperature and C-rate but also shows asymptotic behaviors at high C-rate.
3. propose the concept of anode particle surface saturation as being the mechanism of Li deposition, which is validated through electrochemical calculations.
4. suggest a novel pulse charge protocol that enables Li deposition-free, rapid charge at subzero temperatures by taking advantage of electrochemical reaction heat.

Owing to our 3-electrode cell described in Chapter 2, each data of cathode and anode was measured individually as a function of SOC and temperature, which is used to diagnose how each electrode affects overall full cell behavior. Novel GITT test consisting

of consecutive discharge current and relaxation was introduced, which offers concurrently not only open circuit potentials but also Li diffusion coefficients. Also, as this method does not need specified material information for Li diffusion coefficient measurement, it is convenient for analysis of commercial Li-ion cells, typically having confidential material information. Li diffusivity of the anode is more strongly responsive to temperature compared to that of the cathode, which explains that low temperature study of Li-ion cell requires intensive study of the anode side. This trend is also found in internal resistance from both of DC pulse measurement and EIS test.

In Chapter 3, it was initially assumed that anode potential could be a threshold parameter of Li deposition, which is proved not to be acceptable in universal cases. It is believed that electrochemical potential is varied by electrochemical-thermal interaction at Li deposition-causing charging conditions, e.g. low temperature and/or high current, and measured anode potential is averaged value of numerous particles having different SOC level along the electrode thickness of the whole anode. This distortion of potential measurement cannot represent the phenomenon of Li deposition starting to happen locally at severe charging conditions. Thus instead of monitoring anode potential, charge capacity at a certain charging circumstance was selected to be criteria for determining Li deposition. Experimentally, the critical charge capacity for the onset of Li deposition was obtained, which is critically dependent on temperature and charge C-rate. As temperature is lowered and/or charge C-rate is higher, this critical charge capacity decreases, namely Li deposition starts earlier and becomes more serious. This experimental result induces the concept of anode particle surface saturation. On the particle surface, the mass balance between input of Li^+ ions by charge transfer and output of Li diffusion inside anode

particle determines the surface saturation, which results in Li deposition on the anode particle surface in the mechanism proposed in this study. At given charge current, the rate of charge transfer is fixed so that the rate of Li diffusion should be controlled in order to impede anode particle surface saturation. Actually it can be enhanced by elevated cell temperature through high current charge/discharge pulse announced in Chapter 4.

In a range of maximum allowable operating condition, the critical charge capacity shows asymptotic behavior as charge C-rate increases, which indicates that the minimum value of critical charge capacity as a safety margin of Li deposition exists before the surface is saturated, regardless of charging conditions. Combined with heat generation by high current charge/discharge pulse, the control of pulse duration, i.e. less than the minimum value of critical charge capacity, enables Li-deposition free, rapid charge at subzero temperatures.

In conclusion, the comprehensive study of this dissertation provides the mechanism of Li deposition and its solution. A novel diagnostic tool is additionally introduced.

5.2. Future work

- Different initial SOC:

The present study about Li deposition investigates the critical charge capacity for onset of Li deposition from SOC 0%. In practice, various SOC levels exist in automotive applications. As shown in Fig. 2-9, Li diffusion coefficient in the carbon anode is lowered as SOC increases. Anode potential is also closer to that of Li/Li^+ than SOC 0%.

Therefore, the SOC-dependence of the critical charge capacity is suggested for future investigation.

- *New anode material:*

$Li_4Ti_5O_{12}$ is generally known for Li deposition-free anode material because its equilibrium potential of 1.5V is far away from that of Li/Li^+ [61, 62]. In the thermodynamic sense, it is not prone to Li deposition. Appendix C introduces, however, preliminary tests at 0^oC and -30^oC using CR2016 coin cell (~1.5cm^2 area), which shows serious capacity loss at extreme charging case such as -30^oC and above 5C. Unlike commercial battery-grade graphite, it is easy to control the particle size of $Li_4Ti_5O_{12}$ from nano-size to micron-size [63]. As particle size is inversely proportional to surface area exposed to Li^+ ions, it can be expected under the mechanism of Li deposition proposed here that anode particle surface saturation will be alleviated as particle size is reduced. Therefore it remains to be seen how $Li_4Ti_5O_{12}$ anode behaves with same method introduced here in order to obtain thermodynamic and kinetic parameters and calculate the distribution of Li concentration along with particle size.

- *Over-discharge:*

Similar to the overcharge issue discussed herein, overdischarge adversely affects cycle performance and thermal stability of the Li-ion cell, which is usually controlled by low limit of cell voltage. It is known that overdischarge below 1.5V leads to Cu dissolution and these dissolved Cu^{2+} ions migrate through the separator and cause internal short [64]. As shown in Fig. 4-9, high current charge/discharge pulse at low temperatures shows initially low cell potential around 0V. It is believed that this pulse time is so short

that there would be no capacity loss. But the threshold parameter inducing Cu dissolution should be understood in automotive applications.

- *Thermal analysis:*

Generally, the focus of thermal analysis has been to prevent thermal runaway and to suppress temperature rise at high temperature. But on the other hand, heat generated by high current at low temperature is beneficial to enhance sluggish kinetics of Li-ion cell reaction. Therefore it is necessary to meet both the requirements of thermal safety at high temperature and prevention of Li deposition at low temperature. The main adjustable and measureable parameter is internal resistance because most heat generated is I^2R in high current operation. This should be studied in future work. Additionally, Li-ion battery pack is so large that it could be unfavorable for uniform heat distribution and fast cooling, which is also of much importance compared to small Li-ion cell. Therefore it is essential to study the accumulation of useful heat and the dissipation of harmful heat from cell to pack under the fast and dynamic operating conditions of the electric vehicle.

REFERENCES

1. S. G. Chalk and J. E. Miller, Key challenges and recent progress in batteries, fuel cells, and hydrogen storage for clean energy systems, *J. Power Sources*, **159**, 73 (2006).

2. T. Miller, Advances in NiMH and Li-ion batteries for full hybrids, in *Advanced Automotive Batteries Conference*, Baltimore, MD (2006).

3. Z. Ogumi and M. Inaba, Carbon Anodes, in *Advances in Lithium-Ion Batteries*, W. A. v. Schalkwijk and B. Scrosati Eds., Kluwer, New York (2002).

4. M. B. Armand, Intercalation Electrodes, in *Materials for Advanced Batteries*, D. W. Murphy, J. Broadhead and B. C. H. Steele Eds., Plenum Press, New York (1980).

5. M. Yoshio, A. Kozawa and R. J. Brodd, Introduction: Development of Lithium-Ion Batteries, in *Lithium-Ion Batteries*, M. Yoshio, A. Kozawa and R. J. Brodd Eds., Springer, New York (2009).

6. M. Alamgir and A. M. Sastry, Efficient batteries for tranportation applications, in *Convergence 2008*, 08CNVG-0036, Detroit, MI (2008).

7. M. Broussely, Aging Mechanism and Calendar-Lifer Predictions in Li-Ion Batteries, in *Advances in Lithium-Ion Batteries*, W. A. v. Schalkwijk and B. Scrosati Eds., Kluwer, New York (2002).

8. J. Vetter, P. Novak, M. R. Wagner, C. Veit, K. C. Moller, J. O. Besenhard, M. Winter, M. Wohlfahrt-Mehrens, C. Vogler and A. Hammouche, Ageing mechanisms in lithium-ion batteries, *J. Power Sources*, **147**, 269 (2005).

9. E. V. Thomas, I. Bloom, J. P. Christophersen and V. S. Battaglia, Statistical methodology for predicting the life of lithium-ion cells via accelerated degradation testing, *J. Power Sources*, **184**, 312 (2008).

10. R. Spotnitz, Simulation of capacity fade in lithium-ion batteries, *J. Power Sources*, **113**, 72 (2003).

11. B. Y. Liaw, R. G. Jungst, G. Nagasubramanian, H. L. Case and D. H. Doughty, Modeling capacity fade in lithium-ion cells, *J. Power Sources*, **140**, 157 (2005).

12. R. P. Ramasamy, J. W. Lee and B. N. Popov, Simulation of capacity loss in carbon electrode for lithium-ion cells during storage, *J. Power Sources*, **166**, 266 (2007).

13. Q. Zhang and R. E. White, Calendar life study of Li-ion pouch cells - Part 2: Simulation, *J. Power Sources*, **179**, 785 (2008).

14. Q. Zhang and R. E. White, Capacity fade analysis of a lithium ion cell, *J. Power Sources*, **179**, 793 (2008).

15. D. P. Abraham, S. D. Poppen, A. N. Jansen, J. Liu and D. W. Dees, Application of a lithium-tin reference electrode to determine electrode contributions to impedance rise in high-power lithium-ion cells, *Electrochim. Acta*, **49**, 4763 (2004).

16. S. S. Zhang, K. Xu and T. R. Jow, Study of the charging process of a $LiCoO_2$-based Li-ion battery, *J. Power Sources*, **160**, 1349 (2006).

17. Diagnostic Examination of Generation 2 Lithium-Ion Cells and Assessment of Performance Degradation Mechanisms, ANL-05/21 (2005).

18. M. S. Wu, P. C. J. Chiang and J. C. Lin, Electrochemical investigations on advanced lithium-ion batteries by three-electrode measurements, *J. Electrochem. Soc.*, **152**, A47 (2005).

19. G. Nagasubramanian and D. H. Doughty, 18650 Li-ion cells with reference electrode and in situ characterization of electrodes, *J. Power Sources*, **150**, 182 (2005).

20. J. Zhou and P. H. L. Notten, Development of reliable lithium microreference electrodes for long-term in situ studies of lithium-based battery systems, *J. Electrochem. Soc.*, **151**, A2173 (2004).

21. Q. W. Wu, W. Q. Lu and J. Prakash, Characterization of a commercial size cylindrical Li-ion cell with a reference electrode, *J. Power Sources*, **88**, 237 (2000).

22. J. Fan and S. Tan, Studies on charging lithium-ion cells at low temperatures, *J. Electrochem. Soc.*, **153**, A1081 (2006).

23. E. Karden, S. Ploumen, B. Fricke, T. Miller and K. Snyder, Energy storage devices for future hybrid electric vehicles, *J. Power Sources*, **168**, 2 (2007).

24. A. N. Jansen, D. W. Dees, D. P. Abraham, K. Amine and G. L. Henriksen, Low-temperature study of lithium-ion cells using a Li_ySn micro-reference electrode, *J. Power Sources*, **174**, 373 (2007).

25. M. C. Smart, B. V. Ratnakumar, L. Whitcanack, K. Chin, M. Rodriguez and S. Surampudi, Performance characteristics of lithium ion cells at low temperatures, *IEEE Aerospace and Electronic Systems Magazine*, **17**, 16 (2002).

26. B. V. Ratnakumar and M. C. Smart, Lithium plating and lithium intercalation kinetics as a function of electrolyte composition, in *216th Electrochemical Society Meeting*, Abs. # 650, Vienna (2009).

27. S. J. Harris, A. Timmons, D. R. Baker and C. Monroe, Direct in situ measurements of Li transport in Li-ion battery negative electrodes, *Chem. Phy. Lett.*, **485**, 265 (2010).

28. S. S. Zhang, K. Xu and T. R. Jow, A new approach toward improved low temperature performance of Li-ion battery, *Electrochem. Commun.*, **4**, 928 (2002).

29. M. C. Smart, B. V. Ratnakumar, L. D. Whitcanack, K. B. Chin, S. Surampudi, H. Croft, D. Tice and R. Staniewicz, Improved low-temperature performance of lithium-ion cells with quaternary carbonate-based electrolytes, *J. Power Sources*, **119**, 349 (2003).

30. G. H. Kim, A. Pesaran and R. Spotnitz, A three-dimensional thermal abuse model for lithium-ion cells, *J. Power Sources*, **170**, 476 (2007).

31. S. Al-Hallaj and J. R. Selman, Thermal modeling of secondary lithium batteries for electric vehicle/hybrid electric vehicle applications, *J. Power Sources*, **110**, 341 (2002).

32. D. H. Doughty, P. C. Butler, R. G. Jungst and E. P. Roth, Lithium battery thermal models, *J. Power Sources*, **110**, 357 (2002).

33. K. Hoshina, Y. Tatebayashi, H. Inagaki and N. Takami, Dependence of electrochemical kinetics of lithium titanium oxide electrode on hysteresis during a high-rate charge-discharge reaction, in *216th Electrochemical Society Meeting*, Abs. # 435, Vienna (2009).

34. B. Scrosati and J. Garche, Lithium batteries: Status, prospects and future, *J. Power Sources*, **195**, 2419 (2010).

35. K. Matsuki and K. Ozawa, General Concept, in *Lithium Ion Rechargeable Batteries*, K. Ozawa Ed., Wiley-VCH, Weinheim (2009).

36. Y. C. Zhang and C. Y. Wang, Cycle-life characterization of automotive lithium-ion batteries with $LiNiO_2$ cathode, *J. Electrochem. Soc.*, **156**, A527 (2009).

37. D. W. Dees, A. N. Jansen and D. P. Abraham, Theoretical examination of reference electrodes for lithium-ion cells, *J. Power Sources*, **174**, 1001 (2007).

38. K. Onda, T. Ohshima, M. Nakayama, K. Fukuda and T. Araki, Thermal behavior of small lithium-ion battery during rapid charge and discharge cycles, *J. Power Sources*, **158**, 535 (2006).

39. W. B. Gu and C. Y. Wang, Thermal and electrochemical coupled modeling of a lithium-ion cell, in Lithium Batteries, ECS Proceedings, 99-25, 748 (2000).

40. V. Srinivasan and C. Y. Wang, Analysis of electrochemical and thermal behavior of Li-ion cells, *J. Electrochem. Soc.*, **150**, A98 (2003).

41. K. Smith and C. Y. Wang, Power and thermal characterization of a lithium-ion battery pack for hybrid-electric vehicles, *J. Power Sources*, **160**, 662 (2006).

42. W. Fang, O. J. Kwon and C. Y. Wang, Electrochemical-thermal modeling of automotive Li-ion batteries and experimental validation using a three-electrode cell, *Int. J. Energy Res.*, **34**, 107 (2010).

43. R. A. Huggins, *Advanced Batteries: Materials Science Aspects*, Springer, New York (2009).

44. M. Winter and J. O. Besenhard, Lithiated Carbons, in *Handbook of Battery Materials*, J. O. Besenhard Ed., Wiley-VCH, Weinheim (1999).

45. V. Pop, H. J. Bergveld, D. Danilov, P. P. L. Regtien and P. H. L. Notten, *Battery Management Systems: Accurate State-of-Charge Indication for Battery-Powered Applications*, Springer, Netherlands (2008).

46. Battery Technology Life Verification Test Manual, INEEL/EXT-04-01986 (2005).

47. H. J. Bergveld, W. S. Kruijt and P. H. L. Notten, *Battery Management Systems: Design by Modelling*, Springer, Netherlands (2002).

48. Q. Huang, M. M. Yan and Z. Y. Jiang, Thermal study on single electrodes in lithium-ion battery, *J. Power Sources*, **156**, 541 (2006).

49. R. A. Huggins, Transient behavior of insertion reaction electrodes, *Solid State Ionics*, **86-8**, 41 (1996).

50. A. V. Churikov and A. V. Ivanischev, Application of pulse methods to the determination of electrochemical characteristics of lithium intercalates, *Electrochim. Acta*, **48**, 3677 (2003).

51. C. J. Wen, B. A. Boukamp, R. A. Huggins and W. Weppner, Thermodynamic and mass-transport properties of LiAl, *J. Electrochem. Soc.*, **126**, 2258 (1979).

52. R. A. Huggins, Supercapacitors and electrochemical pulse sources, *Solid State Ionics*, **134**, 179 (2000).

53. W. Fang, O. J. Kwon, C. Y. Wang and Y. Ishikawa, Modeling of Li-ion battery performance in hybrid electric vehicles, in *SAE World Congress*, 09PFL-0573, Detroit, MI (2009).

54. H. P. Lin, D. Chua, M. Salomon, H. C. Shiao, M. Hendrickson, E. Plichta and S. Slane, Low-temperature behavior of Li-ion cells, *Electrochem. Solid State Lett.*, **4**, A71 (2001).

55. P. Arora, M. Doyle and R. E. White, Mathematical modeling of the lithium deposition overcharge reaction in lithium-ion batteries using carbon-based negative electrodes, *J. Electrochem. Soc.*, **146**, 3543 (1999).

56. O. J. Kwon, W. Fang and C. Y. Wang, Lithium deposition in the anode of an automotive Li-ion battery: experiments and modeling, in *15th International Meeting on Lithium Batteries*, Abs. # 279, Montreal (2010).

57. C. A. Vincent and B. Scrosati, *Modern Batteries*, Arnold, London (1997).

58. H. Maleki, J. R. Selman, R. B. Dinwiddie and H. Wang, High thermal conductivity negative electrode material for lithium-ion batteries, *J. Power Sources*, **94**, 26 (2001).

59. S. S. Zhang, K. Xu and T. R. Jow, Charge and discharge characteristics of a commercial $LiCoO_2$-based 18650 Li-ion battery, *J. Power Sources*, **160**, 1403 (2006).

60. C. Forgez, D. V. Do, G. Friedrich, M. Morcrette and C. Delacourt, Thermal modeling of a cylindrical $LiFePO_4$/graphite lithium-ion battery, *J. Power Sources*, **195**, 2961 (2010).

61. J. L. Allen, T. R. Jow and J. Wolfenstine, Low temperature performance of nanophase $Li_4Ti_5O_{12}$, *J. Power Sources*, **159**, 1340 (2006).

62. N. Takami, H. Inagaki, T. Kishi, Y. Harada, Y. Fujita and K. Hoshina, Electrochemical kinetics and safety of 2-Volt class Li-ion battery system using lithium titanium oxide Anode, *J. Electrochem. Soc.*, **156**, A128 (2009).

63. L. Kavan, J. Prochazka, T. M. Spitler, M. Kalbac, M. T. Zukalova, T. Drezen and M. Gratzel, Li insertion into $Li_4Ti_5O_{12}$ (Spinel) - Charge capability vs. particle size in thin-film electrodes, *J. Electrochem. Soc.*, **150**, A1000 (2003).

64. H. Maleki and J. N. Howard, Effects of overdischarge on performance and thermal stability of a Li-ion cell, *J. Power Sources*, **160**, 1395 (2006).

65. FreedomCAR Battery Test Manual for Power-Assist Hybrid Electric Vehicles, DOE/ID-11069 (2003).

66. R. J. Rrodd and K. Tagawa, Li-Ion Cell Production Processes, in *Advances in Lithium-Ion Batteries*, W. A. v. Schalkwijk and B. Scrosati Eds., Kluwer, New York (2002).

Appendix A

Discharge and regen resistance

On pulse test, discharge and regen (charge) resistances are determined using a $\Delta V / \Delta I$ calculation for each iteration of the test profile below [65].

$$R_{\text{discharge}} = \frac{\Delta V_{\text{discharge}}}{\Delta I_{\text{discharge}}} = \frac{V_{t_1} - V_{t_0}}{I_{t_1} - I_{t_0}}, \quad R_{\text{regen}} = \frac{\Delta V_{\text{charge}}}{\Delta I_{\text{charge}}} = \frac{V_{t_3} - V_{t_2}}{I_{t_3} - I_{t_2}}$$

A test cell is fully charged with 1C rate at 25^{o}C and discharged at 1C rate until a specific SOC and held for 1 hour to reach a stable OCP at 25^{o}C. Then the pulse test is conducted in the following sequence: 1C discharge for 1 second, rest for 10 seconds, 1C charge for 1 second and rest for 30 seconds. Next further 2C, 5C and 10C pulse cycles are repeated with these same protocols. After finishing the 1s pulse cycles, 10s pulse tests are conducted.

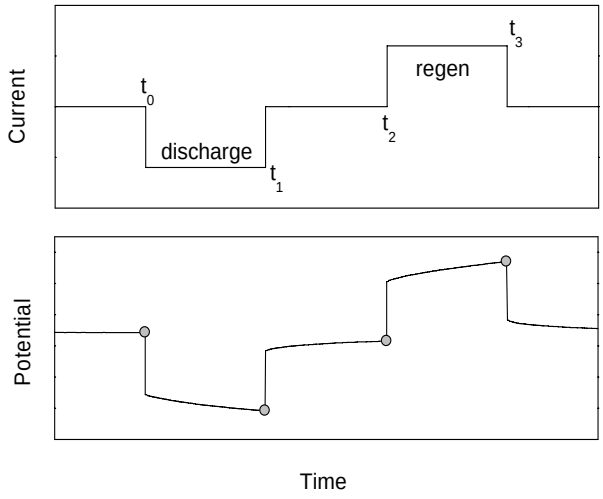

Figure A-1: Pulse test profile

Appendix B

Basic design concept of Li-ion cell

This section introduces how to calculate reversible capacity of the Li-ion cell with given cathode and anode materials. The capacity of the Li-ion ion cell is proportional to how many Li^+ ions can be stored in the cathode and the anode host materials. Thus, some researchers depicted the capacity by area diagram conceptually [66]. Figure B-1 shows this capacity relation with area diagram. In Fig. B-1(a), filled squares mean the irreversible reaction site and empty squares mean the reversible reaction site. Generally, $LiCoO_2$ has irreversible capacity of 2~3% and carbon has 5~7% which is defined as difference between charge capacity and discharge capacity divided by charge capacity. Anode irreversible reaction is mostly related to SEI layer formation, which occurs first of all, followed by intercalation reaction into reversible site upon first charging process in Fig. B-1(b). On next discharging process in Fig. B-1(c), only Li^+ ions of reversible site can move back to cathode reversible site. Therefore the actual capacity of a Li-ion cell depends on how many Li^+ ions are returned in the reversible site of the cathode. In other words, it is derived by the equations below:

Reversible capacity = cathode charge capacity – anode irreversible capacity (B.1)

Anode irreversible capacity = anode charge capacity – anode discharge capacity (B.2)

In the Li-ion battery industry, loading value in unit of mAh/cm^2 is widely used to express capacity value. Cathode loading is the basis because the initial Li source is from

the cathode. Cathode discharge capacity is usually selected as starting loading value: 3.5~4mAh/cm^2 for small Li-ion cell and 1~2mAh/cm^2 for high-power Li-ion cell. Another important parameter is N/P ratio, defined as ratio of anode loading over cathode loading. Anode loading is always higher than cathode by considering process variables in real manufacturing; e.g. uniformity of coated weight and geometric factor of wounded electrodes etc. Following is one example using typical values.

- Cathode loading: 1.3 and N/P ratio: 105
- Irreversible capacity of cathode and anode: 3% and 5%

As N/P ratio is 105, anode loading is 1.37. Considering irreversible capacity, charge loading of each electrode is 1.34 and 1.44, respectively. By combining Eq. (B-1) and Eq. (B-2) with the above figures, reversible capacity of the full cell is 1.27mAh/cm^2: 1.34 – (1.44 – 1.37). Cell designers choose each material and decide loading and N/P ratio in the first step. As mentioned shortly in Section 3.3, N/P ratio can be controlled to obtain safety margin over overcharge and Li deposition in general. But as N/P ratio is higher at given cathode loading, reversible capacity of the full cell decreases slightly. Assuming high N/P ratio is 120, anode loading is 1.56 and then reversible capacity of 1.26 is obtained. But in aspect of capacity density, there is a huge loss of total available anode: 1.26/1.56 vs.1.27/1.37. Therefore optimum N/P ratio should be selected.

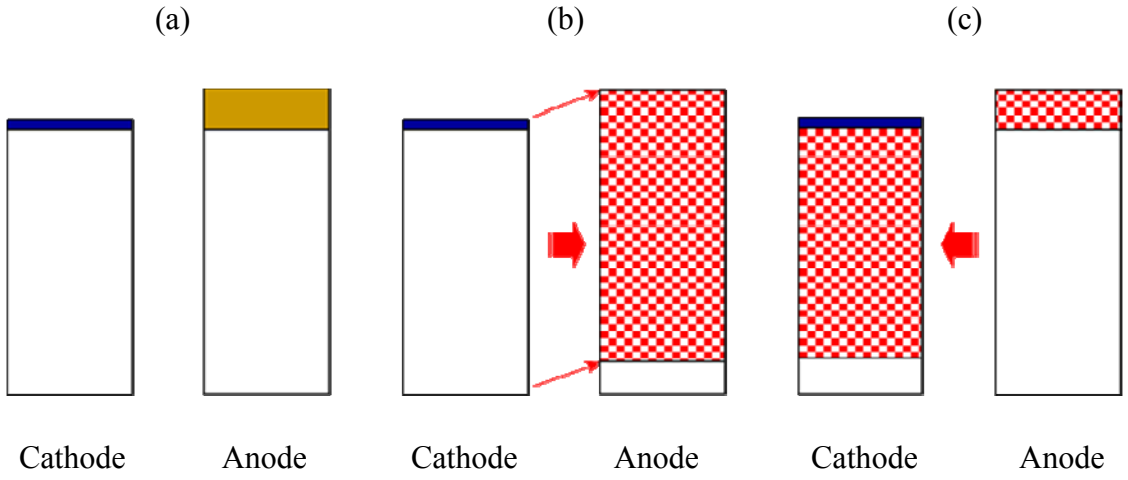

Figure B-1: Depiction of capacity calculation: (a) initial state; (b) first charge; and (c) first discharge. Filled squares mean irreversible reaction site and empty squares mean reversible reaction site. Patterned square indicates Li occupied at each reaction site.

Appendix C

Low temperature test of $Li_4Ti_5O_{12}$

$Li_4Ti_5O_{12}$ (LTO) is known for Li-deposition free anode materials due to its high electrochemical potential. In order to adopt the mechanism of Li deposition proposed in Chapter 3, similar tests were conducted using CR2016 coin cell (20mm diameter and 1.6mm thickness). LTO used is procured from Ishihara Sangyo, which measured BET surface area of 2.5m^2/g and average particle diameters of 6.6μm. LTO slurry paste that consists of 85 wt.% of LTO, 5 wt.% of carbon black and 10 wt.% of PVdF binder was coated onto Al foil and dried overnight at 120^{o}C before assembling coin cells in an Ar-filled glove box. Cathode was obtained from 18650 cylindrical cell used in this dissertation. Coin full cell shows 1C discharge capacity of 1.9mAh at 25^{o}C within 1~2.8V. Similar test to find critical charge capacity was employed at 0^{o}C and -30^{o}C.

As shown in Fig. C-1, there is no serious capacity loss at 0^{o}C but at -30^{o}C. It is believed that nobody tried these severe charging conditions to LTO material. Even though electrochemical potential of LTO is far higher than that of Li/Li^+, Li deposition in LTO anode at -30^{o}C is suspected in similar to graphite-based 18650 Li-ion cell, which could be explained with the concept of anode particle surface saturation. Interestingly, as shown in Fig. C-2, the minimum critical charge capacity of 0.1mAh is also shown but 0.2mAh 10C charge at -30^{o}C leads to huge capacity loss of 50%.

In sum, the LTO-based cell has feature that Li deposition does generally not happen at low temperature compared to a graphite-based cell. But in extreme charge case,

it also shows serious capacity loss, which can result because all anode materials are generally governed by the mechanism of anode particle surface saturation.

(a)

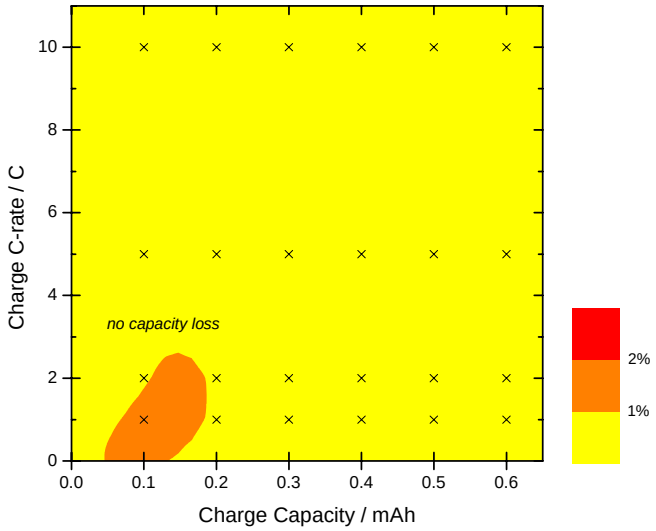

(b)

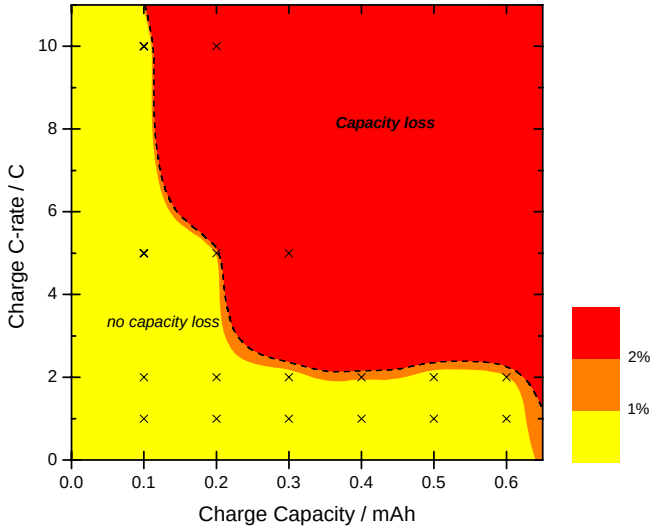

Figure C-1: The plot of capacity loss as a function of charge C-rate and charge capacity in LTO-based coin full cell: (a) at 0^{o}C and (b) at -30^{o}C

(a)

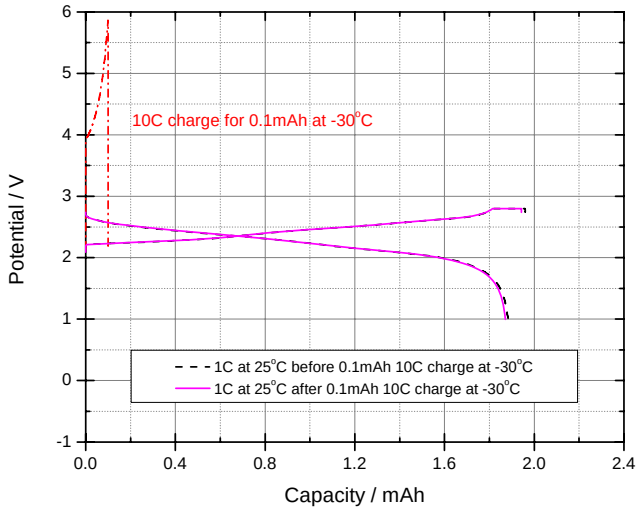

(b)

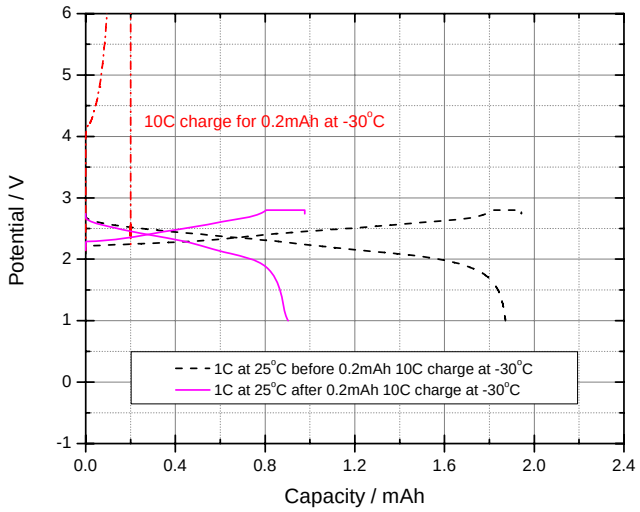

Figure C-2: 1C capacity comparison of LTO-based coin full cell at 25°C: (a) after 0.1mAh 10C charge at -30°C and (b) after 0.2mAh 10C charge at -30°C

VITA

Ou Jung Kwon

EDUCATION

The Pennsylvania State University, University Park, PA, USA 2007 ~ 2010

Ph.D. in Materials Science and Engineering

Advisor: Dr. Chao-Yang Wang

Seoul National University, Seoul, South Korea 1999 ~ 2001

M.S. in Chemical Engineering

Advisor: Dr. Seung Mo Oh

Seoul National University, Seoul, South Korea 1995 ~ 1999

B.S. with honors in Chemical Engineering

WORK EXPERIENCE

The Pennsylvania State University, University Park, PA Sep. 2007 ~ Aug. 2010

Research Assistant, Electrochemical Engine Center

- Degradation of Automotive Li-ion Batteries: Li deposition; Accelerated test
- A fabrication line of Li-ion batteries

LG Chem Research Park, Daejeon, South Korea Jan. 2001 ~ Aug. 2007

Senior Researcher, Battery Research and Development Mar. 2006 ~ Aug. 2007

- Si-based composite anode materials and their electrodes
- A pilot line to produce Si-based composite anode materials

Research Engineer, Battery Research and Development Jan. 2001 ~ Feb. 2006

- Carbonaceous anode materials for high-capacity 18650 cells
- A new process to make spherical carbonaceous materials

Seoul National University, Seoul, South Korea Oct. 1999 ~ Dec. 2000

Research Assistant, Electrochemical Energy Conversion & Storage Laboratory

- High-capacity carbonaceous anode materials in Li-ion batteries